Geophysical Methods and Strategies to investigate Rock-physical Properties at the Field-scale: Methane, Hydrogen and Heat Injection under Experimental Conditions.

Dissertation

der Mathematisch-Naturwissenschaftlichen Fakultät

der Eberhard Karls Universität Tübingen

zur Erlangung des Grades eines

Doktors der Naturwissenschaften

(Dr. rer. nat.)

vorgelegt von

Susann Birnstengel

aus Berlin

Tübingen

2023

Gedruckt mit Genehmigung der Mathematisch-Naturwissenschaftlichen Fakultät der Eberhard Karls Universität Tübingen.

Tag der mündlichen Qualifikation:	27.11.2023
Dekan:	Prof. Dr. Thilo Stehle
1. Berichterstatter/-in:	Prof. Dr. Peter Dietrich
2. Berichterstatter/-in:	Prof. Dr. Reinhard Drews

Geophysical methods and strategies to investigate rock-physical properties in the field-scale: methane, hydrogen and heat injection under experimental conditions

Thesis submitted to

Faculty of Science
Eberhard Karls University of Tübingen

in partial fulfilment for the award of the doctoral degree by

Susann Birnstengel

Immerhin kommen mir die meisten Wege schon irgendwie bekannt vor. Aber eigentlich ist es ja gar nicht unsere Bestimmung, die Wege zu kennen. Es ist gerade unsere Bestimmung sie *nicht* zu kennen. Wir kommen nicht auf die Welt, um Antworten zu finden, sondern um Fragen zu stellen. Man tapst sozusagen in einer immerwährenden Dunkelheit herum, und nur mit viel Glück sieht man manchmal ein Lichtlein aufflammen. Und nur mit viel Mut und Beharrlichkeit oder Dummheit oder am besten mit allen zusammen kann man hie und da selber ein Zeichen setzen!

Zitat Prof. Freud aus "Der Trafikant"
ROBERT SEETHALER

Abstract

Seismic borehole techniques offer the opportunity to characterize the near-surface aquifer properties sensitively. Knowledge of rock-physical relations at the field scale is essential for interpreting geophysical measurements. However, transferring the results of existing lab-scale studies directly to the field scale remains challenging due to the use of different frequency ranges. To address this issue, we developed an experimental monitoring setup for gas and heat injection experiments to study rock-physics relations at the field scale. We successfully studied the dependence of temperature and gas saturation on seismic properties, respectively. The integration of geophysical measurements into a hydrogeological problem allows us to demonstrate the applicability of theoretical rock-physical concepts at the field scale, providing an essential link to the discipline of hydrogeophysics. After a thorough preliminary survey, which revealed a detailed picture of the subsurface conditions, we were able to define suitable test site areas for our injection experiments. With controlled injections of heat, CH_4, and H_2 at depth ranges between 7-$18\,\mathrm{m}$, we obtained controlled changes in sediment parameters such as temperature and water saturation. We monitored the temperature and saturation changes in a time-lapse experiment for at least twelve months at observation depths between 8-$18\,\mathrm{m}$. In each case, we analyzed P-wave velocity and amplitude change, including energy level and quality factor. A subsequent comparison of our seismic data with in situ water content measurements obtained from the gas injection experiments using different computational approaches resulted in a fit. It confirmed the method of seismic cross-hole measurement for gas leakage detection. With a comprehensive monitoring layout we furthermore detected parameter changes inferred from temperature variations in the subsurface and compared the results to in situ temperature measurements. We demonstrate in our experiments that we verify rock physics relationships at the field scale with our experimental setup and quantify relative water content changes in the subsurface.

Zusammenfassung

Die Verwendung von seismischen Bohrlochmessungen eröffnet uns die Möglichkeit, physikalische Eigenschaften oberflächennaher Grundwasserleiter aussagekräftig zu charakterisieren. Dabei sind Kenntnisse bezüglich gesteinsphysikalischer Zusammenhänge im Feldmaßstab für die Interpretation der geophysikalischen Messungen unerlässlich. Eine Herausforderung bildet dabei die direkte Übertragung von Erkenntnissen aus Laborstudien auf den Feldmaßstab. Grund dafür ist, dass die Messdurchführung in verschiedenen Frequenzbereichen stattfindet. Um dieses Problem anzugehen, haben wir unter zu Hilfenahme von Wellenfeldsimulationen eine Monitoring-Konzept für Gas- und Wärmeeinleitungsexperimente entwickelt, um die gesteinsphysikalischen Zusammenhänge im Feldmaßstab zu untersuchen. Die Auswirkungen variierender Temperaturen bzw. Gassättigungen auf seismische Eigenschaften konnte dabei erfolgreich beobachtet werden. Daraus zeigt sich, dass die Integration geophysikalischer Messungen in eine hydrogeologische Fragestellung es ermöglicht, die Anwendbarkeit theoretischer gesteinsphysikalischer Konzepte im Feldmaßstab nachzuweisen. Sie stellt damit eine wichtige Verbindung zur Disziplin der Hydrogeophysik her. Um ein, für unsere Arbeiten notwendiges und detailliertes Bild der Untergrundverhältnisse zu erhalten, erfolgte eine umfangreiche, adaptive Vorerkundung des Testgeländes. Damit konnten wir geeignete Versuchsflächen für unsere Eintragsversuche festlegen. An ausgewählten Standorten führten wir kontrollierte Injektionen von CH_4, H_2 und Wärme, in Tiefenbereichen zwischen 7 m - 18 m Tiefe durch und erzielten eine Veränderung der Sediment-Parameter (Temperatur, Wassersättigung). Den Prozess der Temperatur- und Sättigungsänderung verfolgten wir jeweils in einem Zeitraffer-Experiment über einen Zeitraum von mindestens zwölf Monaten in Beobachtungstiefen zwischen 8 - 18 m. Die Untersuchungen umfassten dabei jeweils eine Analyse der P-Wellen-Geschwindigkeit und Amplitudenveränderung einschließlich des Energielevels und Qualitätsfaktors. Innerhalb des Gaseintragexperiments verglichen wir die seismischen Daten mit in-situ Wassergehaltsmessungen unter Verwendung verschiedener Berechnungs-Ansätze.

Die Bewertung der Ergebnisse bestätigte den Ansatz, Bohrlochseismik zur Erkennung von Gasleckagen in Betracht zu ziehen. Unsere Experimente zeigen, dass wir mit unserem Versuchsaufbau gesteinsphysikalische Beziehungen auf der Feldskala verifizieren und relative Wassergehaltsänderungen im Untergrund quantifizieren können. Die Verifizierung unserer Methode zum Erkennen von Parameterveränderungen durch Temperaturvariationen im Untergrund konnte mit unserem ersten Experiment aufgrund technischer Schwierigkeiten nicht zufriedenstellend erfolgen. Die Ergebnisse eines Anschlussprojektes mit ähnlicher Fragestellung und einer erweiterten Messanordnung lieferten jedoch sehr aussichtsreiche Ergebnisse. Dabei konnte eine Anomalie im P-Wellenverhalten beobachtet, welche bei anschließender Recherche hinreichend erklärt und bestätigt wurde. Wir folgern daraus, dass seismische Bohrlochmessungen Potenzial bieten, als Erkundungs- und Überwachungsmethode für Wärme-induzierte Prozesse im Untergrund eingesetzt zu werden.

Eidesstattliche Erklärung

Ich erkläre durch meine Unterschrift an Eides statt, dass ich diese Arbeit, abgesehen von der Beratung durch die Betreuenden, selbständig verfasst habe. Darüber hinaus erkläre ich, dass diese Dissertationsschrift nicht, auch nicht auszugsweise, im Rahmen eines Prüfungsverfahrens vorgelegen hat. Teile der Dissertationsschrift sind zur Veröffentlichung eingereicht worden. Betreffendes Text- und Bildmaterial wurde kenntlich gemacht. Die Arbeit ist unter Einhaltung der Regeln guter wissenschaftlicher Praxis der Deutschen Forschungsgemeinschaft entstanden.

Declaration of academic honesty

I declare that this dissertation has been composed by myself, apart from the advice of my supervisors. Furthermore, I declare that this dissertation has not been presented, not even in part, in the context of an examination procedure. Parts of the thesis are submitted for publication. Relevant text and image material have been identified. The thesis has been written in compliance with the rules of good scientific practice of the German Research Foundation.

Data Availability

The original data used for this publication is provided in the Data Management
Portal of the Helmholtz Center for Environmental Research - UFZ. Additional
data publications are available in Pangaea
(Pohle et al.; 2022, https://doi.pangaea.de/10.1594/PANGAEA.940676;
https://doi.pangaea.de/10.1594/PANGAEA.940914).

Acknowledgement

The work presented here was developed as part of the collaborative projects TestUM I and II funded by the BMBF.

First, I sincerely thank my supervisors Prof. Peter Dietrich and Dr. Ulrike Werban, for their tireless support, learning and development opportunities, and constructive feedback and patience. You strongly encouraged me to shape my own path rather than confining it and gave me the possibility to build valuable connections to the scientific community across countries.

I thank Prof. Reinhard Drews for taking an interest in my work and making time to evaluate my thesis.

Thanks to the TestUM team for making the project and all the experiments possible. Thank you for teaming up in the field, Götz and Klas, and for providing the results on which I could verify the findings of my experiments, Linwei. A special and big thanks goes to the people who supported and facilitated the necessary fieldwork, the preliminary investigation and the incessant monitoring trips. Helko, I am still happy we were able to save your thumb. Schossi, I am glad we made it through the (first) heat wave over Brandenburg. Marco, only grumpy phone calls will ever save ERT data, thanks for all the technical and not so technical support that was also given by Simon, Krecki, Thomas, Matteo, Paul and Peter. I thank Hendrik, Kilian, and Uta for your tremendous support during the data uncluttering and processing phase. I thank Olaf for enabling simulations and Thomas for helping my head to disentangle models and math.

Nina, thanks for lending me your ears, couch supply and to not mince matters.

I especially thank Vera for making time to go through this work and provide extremely helpful feedback and for your infectious passion for being a scientist.

To the people that I declare the most important rest in my life: Thank you friends and family. For grounding me, being thick-skinned, for having my back, and being at my side.

So much for Lisbeth!

.

Contents

List of Figures

List of Tables

List of Symbols

Symbol	Description	Unit
B	Pore space modulus	$\mathrm{N\,m^{-2}}$
K_i	Compressional modulus of single elements	$\mathrm{N\,m^{-2}}$
k_f	Hydraulic conductivity	$\mathrm{ml/\,min\,/kPa}$
K	Compressional modulus	$\mathrm{N\,m^{-2}}$
K_{dry}	Effective bulk moduli of the dry rock	$\mathrm{N\,m^{-2}}$
K_f	Compressional bulk modulus of the fluid	$\mathrm{N\,m^{-2}}$
K_g	Compressional bulk modulus of the gas	$\mathrm{N\,m^{-2}}$
K_m	Compressional bulk modulus of the drained matrix, solid grains	$\mathrm{N\,m^{-2}}$
K_R	Reuss average	$\mathrm{N\,m^{-2}}$
K_{sat}	Effective bulk moduli of the saturated rock	$\mathrm{N\,m^{-2}}$
K_V	Voigt average	$\mathrm{N\,m^{-2}}$
K_w	Compressional bulk modulus of the gas	$\mathrm{N\,m^{-2}}$
M	P-wave modulus	$\mathrm{N\,m^{-2}}$
M_{dry}	Elastic P-wave modulus of the skeleton	$\mathrm{N\,m^{-2}}$
M_f	Fluid modulus	$\mathrm{N\,m^{-2}}$
M_g	Gas modulus	$\mathrm{N\,m^{-2}}$
M_m	Elastic P-wave mineral modulus	$\mathrm{N\,m^{-2}}$
M_{ps}	P-wave modulus of partially saturated media	$\mathrm{N\,m^{-2}}$
M_R	Reuss average of the P-wave modulus	$\mathrm{N\,m^{-2}}$
M_{sat}	Elastic P-wave modulus of the partially saturated rock	$\mathrm{N\,m^{-2}}$
M_w	Water modulus	$\mathrm{N\,m^{-2}}$
P	Pressure	Pa
Q	Flow rate	$\mathrm{ml/\,min}$
Q_f	Quality factor	$-$
s	Distance	m
S_g	Gas saturation	$-$
S_w	Water saturation	
t	Traveltime	s
t_{fs}	Traveltime in full saturated rock	s

Symbol	Description	Unit
t_{ps}	Traveltime in partly saturated rock	s
T	Temperature	°C
v	Seismic wave velocity	$\mathrm{m\,s^{-1}}$
v_f	Interval velocity of the pore fluid	$\mathrm{m\,s^{-1}}$
v_g	Interval velocity of the injected gas	$\mathrm{m\,s^{-1}}$
v_m	Interval velocity of the matrix material	$\mathrm{m\,s^{-1}}$
v_P	Seismic P-wave velocity	$\mathrm{m\,s^{-1}}$
v_S	Seismic S-wave velocity	$\mathrm{m\,s^{-1}}$
v_w	Interval velocity of the water	$\mathrm{m\,s^{-1}}$
V_i	Volume friction	m
α	Biot-Willis coefficient	-
Θ_g	Gas content	Vol.%
Θ_w	Water content	Vol.%
μ	Shear modulus	$\mathrm{N\,m^{-2}}$
μ_i	Shear modulus of the elements	$\mathrm{N\,m^{-2}}$
μ_{dry}	Shear modulus of the rock skeleton	$\mathrm{N\,m^{-2}}$
μ_m	Shear modulus of the mineral phase	$\mathrm{N\,m^{-2}}$
μ_R	Shear modulus of the Reuss bound	$\mathrm{N\,m^{-2}}$
μ_{sat}	Shear modulus of the saturated rock	$\mathrm{N\,m^{-2}}$
μ_V	Shear modulus of the Voigt bound	$\mathrm{N\,m^{-2}}$
ρ	Density of the rock, material	$\mathrm{kg\,m^{-1}}$
ρ_f	Density of the pore filling	$\mathrm{kg\,m^{-1}}$
ρ_g	Density of the gaseous phase	$\mathrm{kg\,m^{-1}}$
ρ_m	Density of the mineral phase	$\mathrm{kg\,m^{-1}}$
ρ_w	Density of water	$\mathrm{kg\,m^{-1}}$
Φ	Porosity	—

List of Abbreviations

ASTM American society for testing and materials

BERT Boundless electrical resistivity tomography software

CMD Electromagnetic conductivity meters

CPT Cone penetrometer test

DGPS Differential global positioning system

DP Direct-push

EC Electrical counductivity

EMI Electromagnetic induction

ERT Electrical resistivity tomography

FBP First break picking

GPR Ground penetrating radar

HDPE High-density polyethylene

HPT Hydraulic penetration tool

HT-ATES High tempererature - Aquifer thermal energy storage system

P-wave Pressure wave

RB1 First receiver borehole

RB2 Second receiver borehole

S-wave Shear wave

SB Source borehole

SMT Soil moisture probes

SNR Signal-to-noise ratio

TestUM Testfeld zur Untersuchung und zum Monitoring durch die Nutzung des Untergrundes induzierter reaktiver Mehrphasentransportprozesse in oberflächennahen Aquiferen

VSP Vertical seismic profiling

1

Introduction

Frag nicht was die Geophysik für
dich tun kann, sondern was du für
die Geophysik tun kannst

P. DIETRICH

With the energy transition being one of the biggest challenges for today's society, every avenue should be explored for sustainable energy generation and storage. The near-surface subjected to extensive interventions plays an important role when approaching the field of energy transition and its related research. Hence supply and distribution infrastructures are expanding and face environmental protection challenges at the same time. Leakages in gas pipelines or geothermal heating systems are not uncommon, as the gas leaks of Nord Stream 1 and 2 natural gas pipelines in the Baltic Sea showed recently [Deutsches Zentrum für Luft und-Raumfahrt, 2022]. Leakages that result in above-ground outlets are hardly detectable in the subsurface. Therefore the assessment and monitoring of gas and heat storage together with their distribution facilities remain essential. Their corresponding induced processes in the near-surface are crucial and open to a reliable risk assessment and impact analysis on our groundwater resource. Observing the dynamics of subsurface parameters such as porosity, saturation and permeability will conduce to the understanding of hydrogeological processes in the subsurface [Jorgensen, 1989, Diallo, 2000, Lamert et al., 2012]. Those rock properties are imaged by geophysical proxies that are individually subjected to natural environmental and anthropogeneous influences. Near-surface geophysics, in particular, uses geophysical methods to investigate small-scale features in the shallow subsurface. Finding and evaluating relationships at the scale of interest is an important but complex task. The recognition of integrating geophysical measurements into hydrogeological studies grows and could significantly advance our understanding of dynamic hydrogeological processes, especially at intermediate scale [Robinson et al., 2008]. Since those observations do not generally provide direct

1
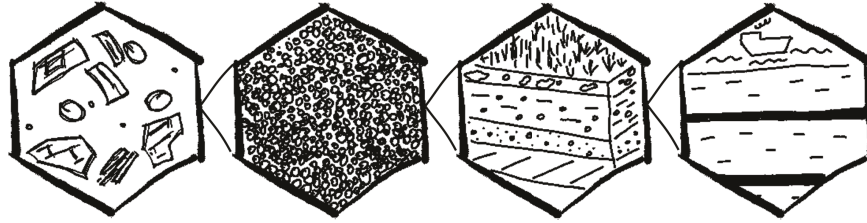
Figure 1.1: Research at different scales. From laboratory (μ - dm) over field (m - dm) to seismic scale (km)

information about hydrogeological properties, their effective use is governed by the strength of the relationship between estimated geophysical properties and the properties of interest [Binley et al., 2015, Blazevic et al., 2020].

1.1 Research at different scales

An intensive amount of research tackles energy-related questions. Depending on the issue, researchers explored different dimensions, scales, and carriers of energy with different geophysical methods. I will mention a few of them in the following to gain an insight into the extent of the topic:

1.1.1 Seismic scale

Especially in the exploration of carbon capture and storage sites e.g., to detect the change in seismic velocity and to image the gas distribution in the reservoir (or even model CO_2 saturation [Hu et al., 2017]), various examples exist for the application of seismic methods [Zhang et al., 2012, Götz, 2014, Onishi et al., 2009]. [Lumley, 2010] provides an overview on 4D seismic monitoring. They look very closely at seismic properties of pure and mixed CO_2 and provide improvement suggestions on SNR, processing flows, and algorithms for 4D purposes. [Lumley, 2001] states that in reservoir monitoring, the 4D-seismic technology is advancing exponentially in reservoir modeling and management. 4D survey describes time-lapse data of 3D seismic surveys. The fourth dimension is time. Other time-lapse monitoring techniques are repeated 2-D seismic surveys, surface seismic, vertical seismic profiling (VSP), borehole- borehole, cross well measurements, and non-seismic techniques including time-lapse electromagnetic survey, gravity data as well as ground penetrating radar (GPR). [Harris et al., 1995] performed a time-lapse and high-resolution cross well- measurement, imaging a CO_2 injection at a depth of approximately $1\,\text{km}$ and a cross-well distance of $56\,\text{m}$ and $183\,\text{m}$ respectively. [Cahill et al., 2017] investigate the persistence of methane in groundwater. They evaluate the response of GPR and estimate the dimension of the gas plume from amplitude vari-

ations. [Hermans et al., 2013] successfully used time-lapse cross-hole ERT to monitor thermal transport processes during a thermal injection and pumping experiment. [Hideki et al., 2008] uses time lapse cross-well seismic tomography for monitoring injected CO_2 in an onshore aquifer where they injected 10400 t of CO_2 at a depth of 1100 m. Geophysical site monitoring, modeling, and seismic surveys for gas and heat detecting technologies [Lumley et al., 2008, Pevzner et al., 2020, Trautz et al., 2020, Milsch et al., 2008, Jaya et al., 2010] as well as geotechnical site investigation [Ng et al., 2019] or time-lapse studies with multi-method approaches [Dangeard et al., 2021] have been applied, discussed and improved over time.

1.1.2 Research at laboratory scale

Although there is no approximate amount of time-lapse surveys in the near-surface investigating the field scale, laboratory studies are available. [Gist, 1994] highlighted the gas saturation dependency (using a gas - brine mixture) on seismic velocity for unconsolidated sand and glass beads. He introduced the gas pocket model and the local fluid flow to account for saturation dependence at ultrasonic velocity. The author concludes that those models revert to the effective fluid model for seismic velocities. [Gregory, 1976] investigated the influence of water, oil, gas, and their mixture saturation on rock properties of consolidated rocks at room temperature. The author found P-wave velocity changes between fully gas-saturated and fully water-saturated to be a function of porosity and pressure. In the experiments, gas caused a substantial reduction of the elastic moduli, and he concludes that this effect should be most noticeable at shallow depths and in high-porosity rocks. [Zhang et al., 2021] studied the correlation between temperature variation and its effect on P-wave velocity and uni-axial compressive strength for temperature changes between room temperature and 800°C in the laboratory. The experiments show that the sandstone's P-wave velocity decreases with temperature increase. [Grosso and Mader, 1972], on the other hand, obtained the P-wave velocity in pure water from 0 °C - 100 °C, where the P-wave velocity increases with increasing temperature between 0 °C - 73 °C and decreases from 73 °C - 100 °C. [Jaya et al., 2010] performed lab measurements to predict the thermo-physical effect of the saturating pore fluid on the seismic properties by applying a rock physics model. They used Gassmann's relations as a basic principle for the model and modified them to account for temperature dependence. The influence of temperature on seismic velocity is strongly related to thermo-physical characteristics of the corresponding pore fluid [Wang and Nur, 1990]. The measurements show decreasing P-wave velocities with increasing temperature, whereas bubbles and micro - fracturing reduce the seismic velocity. They observe hysteresis effects in the P-wave velocities. The observed quality factor is increasing over the 50 °C - 125 °C range, and it concludes that temperature-dependent seismic attenuation is a complex issue and needs more research.

1.1.3 The gap

It becomes increasingly important to reveal and evaluate relations between different subsurface parameters in the field scale. Each one is exposed to various anthropogeneous and environmental influences. Especially our groundwater is strongly exposed to negative influence, so multidisciplinary and monitoring networks across all scales are needed to capture the impact on the groundwater resource as a whole [Cahill et al., 2017]. Rock physical relations are very well investigated for homogeneous sediments in the laboratory scale, but there is a lack of research covering the field scale (m - dm). New concepts and measurement methods are important to reveal rock physical relations, coherency, and dependencies on that scale. One could argue that scaling processes could be usefully applied here. However, standard up-scaling procedures from the core scale to the field scale or downsizing from the reservoir scale are challenging, for example, in terms of frequencies or large variations in the measurement scale [Partyka et al., 2000]. Theoretical considerations, on the other hand, struggle with the reproduction of heterogeneity [Li et al., 2019]. In addition, investigations of rock physical dependencies in unconsolidated materials, while only one parameter is changing at the field scale are unfortunately lacking. Furthermore, long-term investigations must be added to the picture by applying time-lapse surveys in the near-surface when investigating the field scale. Consequently, there is a need for controlled experiments that sustain real conditions in the scale of measurement to attain valid rock physical relations such as saturation changes, temperature, or even changes in grain-to-grain contact due to geochemical processes [Birnstengel et al., 2024].

1.1.4 Gas and heat injection - The approach

For that purpose, controlled gas and heat injections have been planned on preliminarily selected sites. For the gas injection, two different types of gas will be used, methane and hydrogen. This results in material compressibility change through the alteration of the bulk modulus [Nanda, 2016], affecting the seismic signal velocity and amplitude. For the heat injection [Jaya et al., 2010] figured out that reservoir temperature changes will have a thermo-physical effect on the saturating pore fluid. However, the temperature dependence of the rock is guided by the pore fluid. Additionally, due to heating, the potential formation of bubbles affects the rock's saturation condition. These effects allow the application of seismic signal analysis.

Thus, seismic velocity and amplitude are excellent proxies to image gas and temperature-induced parameter changes. The seismic method is well applicable to derive rock physical parameters since the seismic P-wave velocity is strongly affected by the water content in unconsolidated materials [Allen et al., 1980]. That implies that the signal is susceptible to changes in the fluid component. In the saturated zone, the pressure-wave propagation velocity is governed by the pore fluid, not the formation density [Wightman et al., 2004]. The effective

properties of unconsolidated sediments depend upon rock composition and the properties of their components (minerals, pore content). Porosity as a rock physical parameter often shows a distinct correlation with the dominating difference between the properties of the solid and the fluid constituent [Schön, 2004]. One has to take in mind that the position of the groundwater table strongly influences the P-wave and that its application for deriving geotechnical parameters is limited [Paasche et al., 2009]. Whereas capillary pressure strongly affects both P- and S- waves [Solazzi et al., 2021, Romero-Ruiz et al., 2021], shear waves react sensitively to changes in dynamic soil parameters, such as shear strength or modulus of elasticity [Dietrich and Tronicke, 2009]. In Chapter 2 I will further discuss the rock-physical concepts. Due to the presence of glacial till deposit at the test site's subsurface and due to the already mentioned influence of the position of the groundwater table, the idea of using conventional reflection and refraction seismic has been replaced by the application of cross-hole seismic. We set the focus on horizontal cross-hole measurements since [Becht et al., 2004] shows that by using the conventional inversion approach for tomography data, including a full traveltime data set and a homogeneous starting model, anomalies need to be resolved. Cross-hole experiments provide a depth profile of P-waves and, depending on the equipment, sometimes also S-waves. The procedures are outlined in the American Society for Testing and Materials (ASTM) test designation D4428 M-84 (1984). A modified cross-hole seismic layout with two instead of one receiver borehole, already applied by [Diallo, 2000], enables interpretation independent from the source signal while decoupled from surface noise. Due to the size of the local borehole installations, the investigation will be focused on seismic P-waves [Birnstengel et al., 2024]. One key challenge of the experiments is the limitation of the measurement scale and its resolution. The characterized target may be much smaller than the footprint of the geophysical measurement [Binley et al., 2015]. Financial limitations of invasive in situ sampling of the subsurface enforce interpretation based on a few observations at shallow depths. Knowing that the subsurface process or property under investigation can be scale-dependent (e.g., [Schulze-Makuch et al., 1999]), those measurements are limited by the scale they offer [Binley et al., 2015]. Furthermore, it was not possible to perform beneficial density measurements with a cone penetrometer test (CPT) on the test site due to the presence of glacial till in the top layer.

1.2 Objectives

The goal of this work is to determine and, in a first attempt, quantify rock physical dependencies by affecting the subsurface with a (1) methane- (2) hydrogen and (3) heat injection in a controlled manner in the field scale. A near-surface seismic cross-hole setup was able to resolve petrophysical parameter changes. At the same time, repeatability and reproducibility of the experimental design have been evaluated for time-lapse interpretation [Birnstengel et al., 2024].

Data analysis focuses on seismic velocity and amplitude, including quality factors. They are discussed in the matter of indicating and quantifying changes in the pore fluid. We perform a time-lapse borehole experiment to gain insight into the degassing, dissolving, and cooling process in the subsurface. The experiments and their monitoring have been conducted at the test site "TestUM" in Wittstock (Germany). Hereinafter, we compared the results of each gas and temperature injection relative to each other to analyze and interpret the changes of geophysical proxies in regard to their rock physical relations. By reviewing Gassmann's equation, using the approach of [Mavko et al., 1995] to solve them without knowing S-wave velocity and the time-average relation when considering a "patchy saturation", different rock model approaches are discussed to calculate the gas content in the subsurface inferred from geophysical proxies. Finally, we compared the calculated results to measured water content. To debate the applicability for gas leakage detection, we analyzed the data with regard to rock physical interpretation [Birnstengel et al., 2024]. Heat injection results are evaluated long-term to account for sustainable changes in the subsurface condition, such as bulk density, pore fluid distribution, grain to grain contact. A modified Gassmann equation that accounts for temperature dependence, provided by [Jaya et al., 2010], will be used to characterize the influence of temperature on seismic properties. The overall aim of this work is the analysis and interpretation of a hydrogeophysical field study using rock physical relations [Birnstengel et al., 2024].

1.3 Overview of chapters

A brief orientation to the central aspect of the work and its contextual classification, an overview of previous related studies, and research gaps have already been given. Hereinafter follows an introduction to relevant petrophysical and rock physical relations in **Chapter 2**. Understanding how property changes in the near-surface relate to changes in geophysical proxies is essential to interpret results obtained during the experiments. This Chapter gives a detailed look at gas-induced changes in the subsurface and changes that are caused by temperature variations. Aiming for an experiment that performs in the field scale, **Chapter 3** gives an overview of the preliminary investigation and conception of the test site. Relevant operations that are important for an extensive characterization are amply described. This includes electromagnetic, electrical, and hydrogeological surveys, as well as the technical description of the gas and heat injection process. The experiments will be described are part of a collaborative project "TestUM-Aquifer – Testfeld zur Untersuchung und zum Monitoring durch die Nutzung des Untergrundes induzierter reaktiver Mehrphasentransportprozesse in oberflächennahen Aquiferen", and "Geophysikalisches und hydrogeologisches Testfeld zur Untersuchung und zum Monitoring durch die Nutzung des Untergrundes induzierter reaktiver Mehrphasentransportprozesse in oberflächennahen Aquiferen – Zyklischer HT-ATES- Versuch". The work of different project partners builds on each other and is interlinked; their re-

lated contributions are briefly described. The conducted time-lapse study is monitored using seismic cross-hole measurements. This monitoring concept, the monitoring timeline and all necessary processing steps are explained and illustrated in **Chapter 4**. The following **Chapter 5** bundles the geophysical response of the methane, hydrogen, and heat injection in graphs, plots, and tables. A discussion **Chapter 6** follows on from this, and the work is completed with a thorough conclusion in **Chapter 7**.

2

Rock Physics Relation

> It doesn't matter how beautiful
> your theory is, it doesn't matter
> how smart you are. If it doesn't
> agree with experiment, it's wrong.
>
> RICHARD P. FEYNMAN

Hydro-geophysical investigations improve the understanding of hydro- geological processes through geophysical observations. Those observations do not provide direct information about hydro-geological properties. In order to interpret hydro-geophysical field studies, the application of rock physical relations becomes necessary.

2.1 Concepts at the near surface

Natural rocks are heterogeneous materials consisting of various fluid and solid constituents with different properties. Their effective properties depend on rock composition and the properties of their components. It is important to note that scale matters. For example, permeability data measured from core plugs do not represent reservoir properties at larger support volume, such as a rock volume corresponding to a sample in well logs or a seismic trace [Wen, 2018]. This also applies to geophysical attributes. [Müller et al., 2010] reviews laboratory- and field experiments as well as theoretical models that analyze seismic wave attenuation and dispersion in porous rocks. They point out that heterogeneity on various length scales does not permit a simple cor-respondence between the wavelength and heterogeneity scale. Thus, up-scaling procedures from core scale (micron to centimeter) to the seismic scale (me-ter to decimetre) or down-scaling from reservoir scale (km) remain difficult, as mentioned in 1.1.3. [Tiwary et al., 2009] has investigated different up-scaling procedures. They conclude that a considerable deviation in the result depends

on the up-scaling method. Therefore it is challenging to decide in the beginning which method is useful for the particular study. The authors state that the results should be compared to field data performed with the appropriate frequency. [Li et al., 2019,] analyze the accuracy of inferring subsurface rock physical properties based on theoretically modeled or core-scaled measured rock-physic relationships that are themselves derived from elastic constants measured at seismic scale. The authors find that the heterogeneity of the physical properties of rocks at the local scale has a significant impact on this relation. To undertake field-scale experiments, understanding the coherency of rock physical relations on geophysical proxies is crucial. The dominating difference between the properties of the solid and fluid constituents correlates with porosity in most cases [Schön, 2004], whereas the fluid component mainly drives the properties of a saturated rock [Jaya et al., 2010]. Since pores provide the main fluid storage capacity [Schön, 2004], this offers the opportunity to quantify rock physical relations by exchanging or modifying the fluid component impacting saturation and effective porosity. Several experiments have been conducted on this to illustrate the impact of a fluid exchange and a fluid modification on geophysical proxies.

The first experiment describes a methane injection underneath a hydraulic low permeable layer. The fluid component will change and its properties alike. The second experiment resembles the first one but will use hydrogen instead of methane. In the third experiment, a hot water injection into the subsurface, modifying the temperature of the rock's fluid to 75 °C, is described. The last experiment is based on the concept of the first heat injection experiment, where additional extraction, and standby periods are performed.

2.2 Geophysical Proxies and Challenges

To find a suitable experimental setup to correlate geophysical data with changes in the subsurface and related rock physical parameters, several questions have been addressed:

- Which rock physical parameters need to be changed in order to obtain a detectable variance in the subsurface?

  - Water saturation (gas content respectively) and temperature distribution have been defined as target values. They can be externally manipulated in a controlled manner. The temperature can be modified in defined ranges and areas. Injecting gas can be controlled in depth, volume and speed.

- Which parameter depends on the measured variable?

  - The changed variables in the subsurface are temperature and water saturation. This will influence the rock's matrix, more specifically it's

effective porosity, pore fluid viscosity, hydraulic conductivity, temperature of the matrix and the fluid. Those parameter changes will have direct impact particularly on seismic properties such as seismic P-wave velocity and amplitude.

- Which parameters are suitable to quantify rock physical relations at the near surface?

  – This question will be addressed in Section 2.3.1 and 2.3.2.

- How is it possible to change and detect those parameters?

  – The experimental setup and the realization of the injection process is explained in Section 3.2. The simulation of a suitable set-up to detect gas-induced variations is explained in Section 4.2.

- Is the experimental setup repeatable? How can that be verified and how can we assure data quality?

  – Chapter 5 as well as Chapter 6 will capture those questions.

- Is it possible to extend the modification of the subsurface in coordination of scale? If the manipulated area is too wide, different behaviour of the geophysical proxy at different wells will not be visible. If the manipulated area is too narrow, it will not be possible to detect any occurring changes.

  – This topic will be discussed in Chapter 6.

- Can the experiment be performed in heterogeneous environment with meaningful interpretation?

  – This question will be captured in Chapter 6 again. Generally yes and no, since it was not possible to measure all parameters.

2.3   Rock Model Concepts

For geophysical investigations, reliable proxies are needed for the injection experiment to detect saturation and temperature changes in the subsurface. As mentioned in 1.1.4 the seismic P-wave is affected by the moisture content in unconsolidated materials [Allen et al., 1980]. [Grosso and Mader, 1972] has investigated its dependence on temperature changes. Hence, the signal velocity and amplitude is sensitive to water saturation and temperature changes. Assuming that the attenuation will change in the experiment caused by the alteration of the fluid component, it will be indicated by the seismic amplitude and the related quality factor. Seismic velocity, amplitude, and energy are therefore found to be excellent proxies to image gas and temperature-induced parameter changes in the near surface.

2.3.1 Changing pore fluid: gaseous phase

The rock-physical properties are mainly driven by the fluid component and thus are the corresponding geophysical proxies [Birnstengel et al., 2024]. Injecting gas into a saturated rock will modify the rock fluid. Yet the rock-physical properties, similar to the geophysical proxies, are likely to change. To qualitatively detect gaseous components (indirect property), the investigation focuses on seismic velocity and amplitude analyses (direct property). Figure 2.1 shows the main types of models for elastic properties. To tackle the petrophysical problem of fluid substitution and the preferred derivation or estimation of gas content, the layered model as a subgroup of the bound and the pore fluid effect models will be described, applied, and discussed.
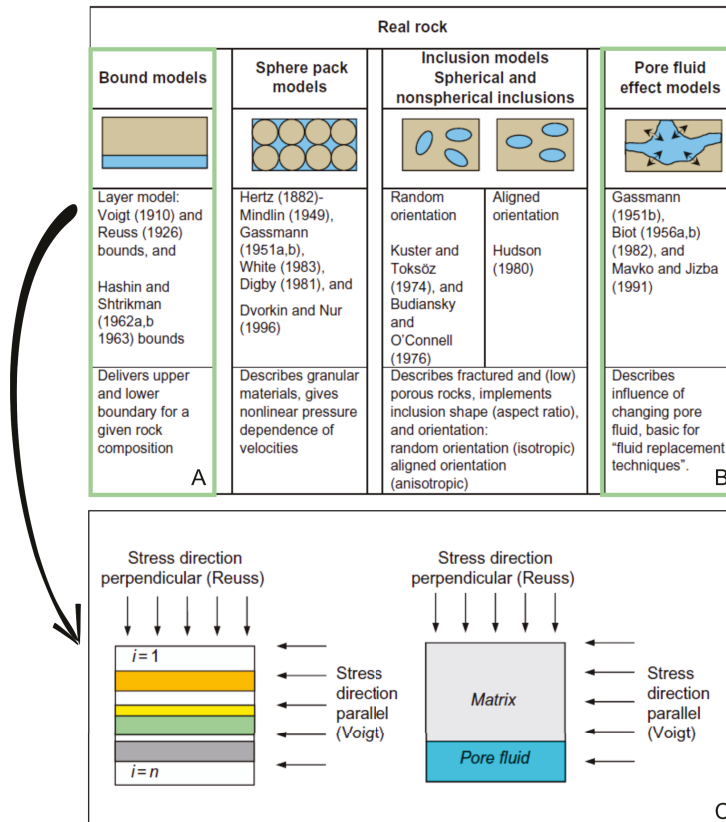
Figure 2.1: Main types of models for elastic properties. A) The Bound- and B) Sphere pack model have been applied. C) Shows the Voigt and Reuss model for the general case of a rock with n components (left) and a simple porous rock with two components: matrix and pore fluid (right) [Schön, 2015]

Bound models

To connect petrophysical parameters with the model of unconsolidated material under homogeneous stress and strain, [Reuss, 1929] and [Voigt, 1910] introduced a basic conceptual model: "The principle of spatial averaging". Suppose the material consists of n isotropic components with a volume fraction V_i, the compressional moduli K_i and the shear moduli μ for homogeneous stress and strain. In that case Voigt's average (parallel) and Reuss' average (serial) is described by Equation (2.1, 2.2), [Schön, 2015]. This concept relies on the separation of individual rock components and its arrangement as a sequence of sheets ("sheet model") [Birnstengel et al., 2024]. In the case of a gas injection, the perpendicular assumption applies since the changes in the subsurface occur vertically with
"water saturated sand" | "gas saturated sand" | "water saturated sand", (Figure 2.1).

$$K_V = \sum_{i=1}^{n} K_i \cdot V_i \qquad \mu_V = \sum_{i=1}^{n} \mu_i \cdot V_i$$

$$K_R = \Big[\sum_{i=1}^{n} \frac{V_i}{K_i}\Big]^{-1} \qquad \mu_R = \Big[\sum_{i=1}^{n} \frac{V_i}{\mu_i}\Big]^{-1} \tag{2.1}$$

$$K_V = (1 - \Phi) \cdot K_m + \Phi \cdot K_f, \quad \mu_V = (1 - \Phi) \cdot \mu_m$$

$$K_R = \big(\frac{1 - \Phi}{K_m} + \frac{\Phi}{K_f}\big)^{-1} \qquad \mu_R = 0 \tag{2.2}$$

Modifications of the model allow applying a seismic traveltime analysis, using the time-average relation 2.3, proposed by [Wyllie et al., 1956]. It is often not specifed with velocity terms but with transit times that are related to a wave path of l = 1m and practically represents a reciprocal velocity [Schön, 2004].

$$\Delta t = \frac{1}{v} = (1 - \Phi)v_m + \frac{\Phi}{v_f} \tag{2.3}$$

The transit time of a wave $\Delta t = \frac{1}{v}$ through a rock with the porosity Φ and v_m, v_f as the matrix and fluid velocity respectively. This relationship, also based on the application of the sheet model in porous rocks, is mainly applied to determine or estimate (matrix-) porosity and is, as an assumption, only valid if:

- the wavelength is small compared to the typical pore size
- pores and grains are homogeneously arranged perpendicular to the ray path
- for consolidated materials with intermediate porosity.

Therefore it does not apply to the given case. However, the wavelength is not small compared to the pore- and grain size, but it is small compared to the areas where saturation changes are occurring [Birnstengel et al., 2024]. Furthermore, [Schön, 2015] announces the problem of multi-phase pore fluids where the

modulus of the mixtures is dominated by the phase with the lowest modulus and, therefore, highest compressibility. If water and gas are evenly distributed in the pore, this results in a jump from the bulk modulus of the gas (K_g) level to the bulk modulus of water (K_w) level immediately at $S_w \to 1$ with S_w as the water saturation. Given the case that fluids are not mixed uniformly, [Schön, 2015] considers a "patchy saturation" whereupon Voigt's average gives the upper bound of the effective elastic modulus and Reuss' average gives the lower bound (2.2,2.1), [Schön, 2015]. They generally describe the upper and lower limit of the effective moduli, the limit of elastic parameters of a composite medium for any mixture [Birnstengel et al., 2024]. Thus, the time-average relation [Wyllie et al., 1956] based on this can be applied in equation 2.6 to estimate gas-induced parameter changes independent from the subsurface density.

Application of the time average relationship

The time-average equation describes the total traveltime recorded on the log as the sum of the seismic wave traveltime through the solid part of the rock and the traveltime through the fluids in the pores [Birnstengel et al., 2024]. When subtracting the P-wave traveltime through a partly saturated rock from the P-wave traveltime through a fully saturated rock the, gas content Θ_g is obtained with:

$s =$ distance from SB to $RB2$,
$t_{fs} =$ traveltime in full saturated rock,
$\Phi =$ porosity,
$v_m =$ interval velocity of the matrix material,
$v_f =$ interval velocity of the pore fluid:

$$\frac{t_{fs}}{s} = \frac{1}{v_f}\Phi + \frac{1}{v_m}(1 - \Phi) \tag{2.4}$$

It describes the total traveltime of the seismic P-wave through the fully saturated rock. The gas injection provides an additional term with t_{ps} as traveltime of the partially saturated rock and v_g as the interval velocity of the injected gas. S_w is the water saturation.

$$\frac{t_{ps}}{s} = \frac{1}{v_g}\Phi(1 - S_w) + \frac{1}{v_w}\Phi S_w + \frac{1}{v_m}(1 - \Phi) \tag{2.5}$$

The water content Θ_w can be defined as: $S_w = \frac{\Theta_w}{\Phi}$. The gas content as Θ_g respectively is received when subtracting equation 2.5 from equation 2.4

$$\frac{\Delta t}{s} = \frac{t_{fs} - t_{ps}}{s} = (1 - S_w)\Phi(\frac{1}{v_g} - \frac{1}{v_w})$$

$$\frac{\Delta t}{s} = \Theta_g(\frac{1}{v_g} - \frac{1}{v_w}) \tag{2.6}$$

$$\Theta_g = \frac{\frac{\Delta t}{s}}{\frac{1}{v_g} - \frac{1}{v_w}}$$

where: s = distance to SB,
Δt = traveltime difference between fully- and partly saturated rock,
v_w = interval velocity of water,
v_g = interval velocity of the injected gas.

Pore fluid effect models

A refined relation applicable for saturated porous rocks with any fluid of known properties is derived by [Gassmann, 1951], (Figure 2.1). It is based on the pore fluid effect model and is natural for unconsolidated rocks. He derived an expression for the corresponding properties of the rock when saturated with any fluid of known properties under the assumption that any relative motion between solid and fluid constituent is negligible [Schön, 2004]. This results in an inertial density of the saturated rock (2.8). It justifies its application only for investigations of elastic waves at low frequency ranges from 10-100 Hz [Diallo, 2000, Benson and Wu, 1999]. [Biot, 1956] extended the model by including dynamic effects through connected pores and allowing relative fluid flow, resulting in a frequency-dependent seismic wave velocity. The low-frequency Gassman-Biot Theory [Gassmann, 1951, Biot, 1956] predicts the relationship between the effective bulk moduli of the dry and the saturated rock K_{dry}, K_{sat} with the shear modulus μ being independent on saturation [Birnstengel et al., 2024].

$$\frac{K_{sat}}{K_m - K_{sat}} = \frac{K_{dry}}{K_m - K_{dry}} + \frac{K_f}{\Phi(K_m - K_f)} \qquad \mu_{dry} = \mu_{sat} \tag{2.7}$$

with:
Φ = porosity,
K_m, K_f = bulk moduli of the mineral- and the fluid material [Mavko et al., 1995].

Application of the fluid substitution equation

Gassmannn's relation is often described as a relation to predict seismic velocities when exchanging the fluid, such as predicting saturated-rock velocities from dry-rock velocities, the so-called fluid substitution problem [Mavko et al., 2020]. The bulk modulus K_i and the shear modulus μ can be derived from P-wave,

and S-wave velocities with ρ as density of the rock, ρ_f as density of the pore filling and ρ_m as density of the mineral phase:

$$K = \rho(v_P{}^2 - \frac{4}{3}v_S{}^2)$$
$$\mu = \rho v_S{}^2$$
$$\rho = \Phi\rho_f + (1 - \Phi)\rho_m. \tag{2.8}$$

Since the shear velocity is unknown, the bulk modulus K_i cannot be extracted from the equation. For this scenario, [Mavko et al., 1995] presented a method to approximate the fluid substitution transform of v_P without knowing v_S by operating directly on the P-wave modulus M. Using the fluid substitution equation of [Mavko et al., 2020] leads to an analogy of equation 2.7 with M_{ps} as the partially saturated P-wave modulus:

$$\frac{M_{sat}}{M_m - M_{sat}} \approx \frac{M_{dry}}{M_m - M_{dry}} + \frac{M_f}{\Phi(M_m - M_f)}, \qquad v_{sat} = \sqrt{\frac{M_{sat}}{\rho}} \tag{2.9}$$

$$\frac{M_{ps}}{M_m - M_{ps}} \approx \frac{M_{dry}}{M_m - M_{dry}} + \frac{M_w}{\Phi S_w(M_m - M_w)} + \frac{M_g}{\Phi(1 - S_w)(M_m - M_g)} \tag{2.10}$$

According to the study, changes in the bulk modulus are linked to the [Reuss, 1929] average of the P-wave modulus M_R, as the pore fluid varies and is defined by equation 2.11 [Birnstengel et al., 2024]:

$$\frac{1}{M_R} = \frac{\Phi}{M_f} + \frac{1 - \Phi}{M_m} \tag{2.11}$$

with $M_m = K_m + 4/3\mu_m = \rho v_P{}^2$ as the mineral- and $M_f = K_f$ as the fluid modulus. [Bachrach and Nur, 1998] consider the gas bulk modulus $M_g = M_f$-M_w as part of the effective modulus of the pore fluid for partially saturated rocks at low frequencies:

$$\frac{1}{M_f} = \frac{S_w}{M_w} + \frac{1 - S_w}{M_g} \tag{2.12}$$

With known P-wave velocities, the density variations can be extracted.

With known S_w the materials density ρ can be derived with ρ_f separated into ρ_w (density of the fluid) and ρ_g (density of the gas) from:

$$\rho = \Phi(S_w\rho_w + (1 - S_w)\rho_g) + (1 - \Phi)\rho_m \tag{2.13}$$

In addition[Bachrach and Nur, 1998] introduced a ratio equation for the case of $S_w < 0.9$, with $M_{ps} \approx$ constant. They state if the residual water saturation at dry conditions can be estimated and average density ρ_1 can be calculated, then the density change (due to saturation change) $\Delta\rho$ can be extracted using:

15

$$\rho_1 v_{P1}^2 \approx (\rho_1 + \Delta\rho)v_{P2}^2 \tag{2.14}$$

with ρ_1 and v_{P1} as the density and the velocity of the unsaturated sand and v_{P2} as the velocity of the fully saturated sand [Birnstengel et al., 2024]. Using the definition of the fluid saturation as depending on fluid content and the porosity of the fluid containing rock (Equation 2.15), the saturation parameters can be calculated with Equation 2.8, 2.13 in 2.14. The gas content can be derived with $S_g = 1 - S_w$ as the gas saturation and Θ_g as the gas content [Birnstengel et al., 2024]:

$$S_g = \frac{\Theta_g}{\Phi} = (1 + \frac{1-\Phi}{\Phi}\frac{\rho_m}{\rho_w})(\frac{v_{P1^2}}{v_{P2^2}} - 1) \tag{2.15}$$

This approach takes recourse to the conceptual model of [Reuss, 1929,]. According to the literature, this model requires a water saturation $< 99\%$ for partially saturated media and applies to the opposite scenario (coming from partial saturation, going to full saturation). The adjustment has been made by flipping the players. Using the elastic moduli for data interpretation remains delicate since the pressure dispersion will likely vary during the injection experiment. Two aspects still contradict the application of the Gassmann relation in the analysis. Fluid changes are assumed to happen due to high pressure [Schön, 2004], which is not the case during the injection experiment. The other aspect is the usage of frequencies > 100 Hz during the experiment.

Biot - Willis

An additional approach related to [Li and Schanz, 2011], is examined. They investigate wave propagation in a 1-D partially saturated poroelastic column using Gassmann's equation with the compressibility $\alpha = 1 - \frac{K_{dry}}{K_m}$, the Biot - Willis coefficient [Biot and Willis, 1957]. $K_m =$ bulk modulus of the solid skeleton and v_P according to equation applies to:

$$K = K_{sat} + \frac{\alpha}{\frac{\alpha - \Phi}{K_m}} = \Phi(\frac{S_w}{K_w} + \frac{S_g}{K_g}), \qquad v_p = \sqrt{\frac{K + \frac{4}{3}\mu}{\rho}} \tag{2.16}$$

Calculating P-wave velocities with changing gas saturation leads to decreased P-wave velocity with increasing water saturation, with a drastic increase for the nearly saturated case (Figure 2.2). The figure shows that increasing water saturation increases the average mixture density and slows the P-wave velocity. The effective bulk modulus K_{sat}, on the other hand, also increases, which speeds up the P-wave. According to [Li and Schanz, 2011], generally the P-wave velocity will increase rapidly, corresponding to the increase of water saturation for large saturation values.
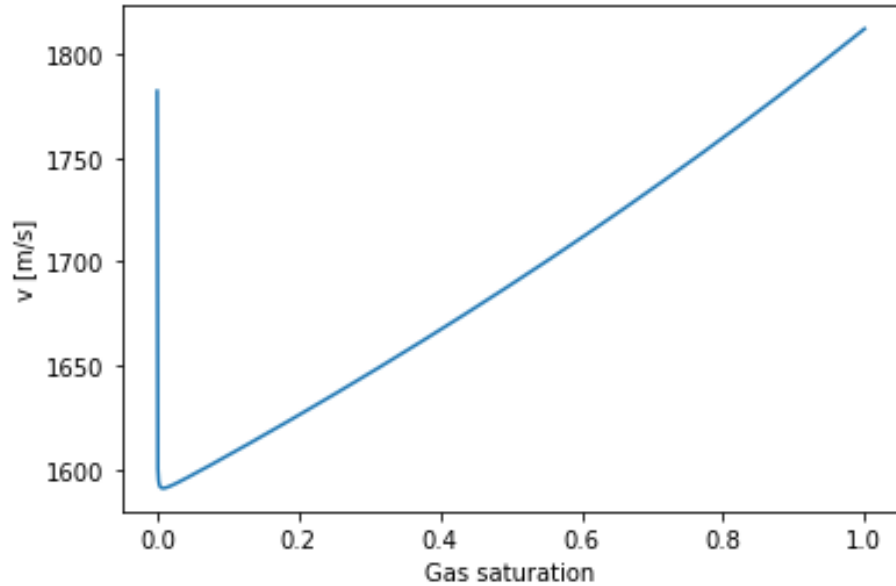
Figure 2.2: P-wave velocity versus gas saturation [Li and Schanz, 2011]

2.3.2 Changing pore fluid temperature

Spatial variability in porosity, fracture density, fluid saturation, tectonic stress, lithology, and temperature contribute to the spatial variability of seismic velocities [Jones et al., 1980, Boitnott and Bonner, 1994]. Studies addressing seismic observations for geothermal applications are mainly focused on laboratory studies and field studies in consolidated rocks. Especially high depth-, temperature- and pressure ranges are imaged [Fehler and Pearson, 1984, Milsch et al., 2008, Jaya et al., 2010, Jaya and Milsch, 2013]. Laboratory temperature-dependence measurements primarily use dry samples under high pressure (6000 bar) and high temperatures (1000 °C). Low-temperature ranges have been covered by [Jaya et al., 2010]. They all show a decrease of seismic P-wave velocity with increasing temperature [Kern et al., 2001]. As already mentioned in the introduction, the effect of temperature on seismic velocities is closely related to thermo-physical characteristics of the fluid, meaning that heat-induced thermo-physical changes of the pore fluid dominate the thermo-physical properties of the sediment [Jaya et al., 2010, Wang and Nur, 1990]). Changes in the pore fluid change the rock bulk modulus, seismic velocity, and attenuation accordingly. That allows a fluid substitution analysis according to the Gassmann relations.

17

Impact of temperature variations on the P-wave velocity

The mentioned studies show that the seismic P- wave velocity decreases with increasing temperature for high temperatures while micro-fracturing and gas bubbles are assumed to account for that behavior. [Zhang et al., 2012] explain the variations with changes of the P-wave when evaporation starts, between room temperature and 400 °C. [Jaya et al., 2010] additionally show that the P-wave velocity slowly increases in water up to a temperature of 75 °C and rapidly decreases in the temperature range between 75 °C and 250 °C. The viscosity of water decreases rapidly up to 75 °C and only gradually after that. Generally, increasing temperature is equivalent to lowering the fluid viscosity, thus lowering its rigidity and its velocity [Bourbie et al., 1987]. The lab investigations of [Grosso and Mader, 1972] (1.1.2) on the speed of sound in water show that for water temperatures between 0 - 73°C, the seismic P-wave velocity is increasing. Recent laboratory studies also indicate that the number, size, and location of pores significantly influence the P-waves propagation independent from the rock's porosity [Di Martino et al., 2021].

Impact of temperature variations on the quality factor

The quality factor (Q-factor) is affected by temperature changes through the liquids' viscosity, bubbles' formation, and thermal micro-fracturing. The increase of the Q-factor in low-temperature ranges has been described by [Dvorkin and Nur, 1993], whereas [Jones et al., 1980] has observed the decrease of the Q-factor at higher temperature ranges. [Jaya et al., 2010] assumes this behavior is related to bubble formation. It is, in general, believed to relate strongly on the thermo-physical properties of the specific pore fluid but is also related to changes in fluid density and viscosity. The authors further assume that a low seismic P-wave velocity together with signs of attenuation are likely indications for rocks being saturated with a high temperature liquid. Those rocks are then subjected to thermal fracturing processes responsible for the generation of patchy saturation distribution due to bubble formation. A high seismic velocity and high attenuation are more likely indicators for rocks being saturated with liquid, subject to a liquid-steam transition or a steam phase. [Vasheghani et al., 2009] shows that one order of magnitude change in viscosity is equivalent to one order of magnitude change in the quality factor.

Application of the Gassmann equation

Revisiting the Gassmann equation expressed with the Biot-Willis coefficient [Biot and Willis, 1957] $\alpha = 1 - K_{dry}/K_m$ will lead to:

$$K_{sat} = K_{dry} + \alpha^2 B$$
$$B = \frac{K_m}{(1 - K_{dry}/K_m) - \Phi(1 - K_m/K_f)} \quad (2.17)$$

With B as the pore-space modulus, the P-wave velocity can be derived to Equation (2.16)

$$v_p = \sqrt{\frac{K_{sat} + 4/3\mu_{sat}}{\rho_{sat}}} \qquad (2.18)$$

$$\rho_{sat} = \rho_{dry} + \Phi\rho_f > \rho_{dry}$$

[Zhijing Wan, 1990] states that in crack-rich rocks, the pore fluid's viscosity also affects rocks' velocities. When its viscosity is high, the pore fluid does not have enough time to reach equilibrium during a half period of the wave, so that the measured velocities are higher. This phenomenon would be especially common in crack-rich rocks such as granite and many sandstone. Especially the changes in viscosity are a main driver for the variation in P-wave velocities. [Jaya et al., 2010] accounts for this with a modification of the Gassmann equation by introducing a temperature-dependent fluid bulk modulus K_f into Equation 2.17.

$$K_f(T) = \rho_f(T)v_f(T)^2 \qquad (2.19)$$

with $\rho_f(T)$ and $v_f(T)$ as temperature dependent fluid densities and their related P-wave velocity. Since the shear wave velocities are unknown, the approximation of fluid substitution after [Mavko et al., 1995] has been applied returning:

$$\frac{M_{sat}}{M_m - M_{sat}} \approx \frac{M_{dry}}{M_m - M_{dry}} + \frac{M_f}{\Phi(M_m - M_f)}, \qquad v_{sat} = \sqrt{\frac{M_{sat}}{\rho}} \qquad (2.20)$$

In theory, this allows the calculation of M_{sat} from P-wave velocities and the bulk density and M_{dry} can be calculated as the inverse of equation 2.17. In a second step, the temperature-dependent $K_f(T)$ is used to derive the changed M_{sat} [Jaya et al., 2010].

3

Conception of the test site

Figure 3.1: Wittstock/Dosse is located in the north of Germany. The test site
"TestUM" (red rectangle) is situated at an old military airport south of a solar
park.
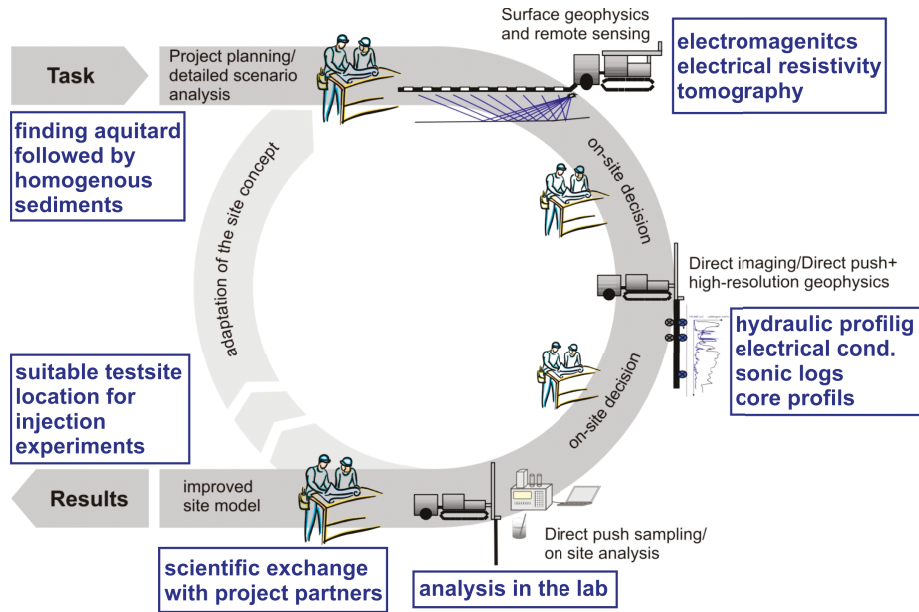
Figure 3.2: The cycle scheme of an adaptive approach adjusted to our research question. The cycle has been re-run until a suitable test site has been found.

3.1 Pre-site survey

The test site "TestUM" ("**Test**feld zur **U**ntersuchung und zum **M**onitoring durch die Nutzung des Untergrundes induzierter reaktiver Mehrphasentransportprozesse in oberflächennahen **Aquiferen**") is located in the north of Germany close to Wittstock/Dosse (N 53° 11'77 38.9616, E 12° 30' 11.178). It has partly been used for a $CO2$ storage experiment in 2010 [Peter et al., 2012], (Figure 3.1) and continues now to be used for our gas and heat storage experiments by applying selected geophysical methods. For an extensive pre-site survey we combined geophysical and in situ hydrogeological exploration techniques. Therefor we used an adaptive exploration approach (Figure 3.2) that resulted in a comprehensive picture of the geological and hydrogeological subsurface properties. The main goal of the preliminary investigation was the definition of suitable test areas in terms of subsurface character. The subsurface need to meet certain requirements for on-site experiments including a low permeable upper boundary followed by a homogeneous layered Quaternary sand. The enclosure by an aquiclude (geological material fluid flow = 0) was preferred. At the very beginning we need to gain information about possible obstacles in the near subsurface to assure drilling clearance in the area. This has been accomplished by 2D-electromagnetic (EM) surveys in connection with 2D-electrical resistivity tomography (ERT). Those information have been gathered with in situ hydraulic characterization in selected areas using direct push (DP) tech-

nologies [Dietrich and Leven, 2006, Köber et al., 2009]. Measurements with the hydraulic profiling tool (HPT) [Dietrich et al., 2008] and the electrical conductivity (EC) log resulted in a depth orientated strati-graphical interpretation.

3.1.1 Electromagnetic Survey (EM)

Initially, we extensively explored the whole test site via electromagnetic induction (EMI) using a CMD-Explorer and a CMD-Mini-Explorer (GF Instruments, Brno). With three different coil separations we explored various depths of investigation from 0.5 m up to 6.7 m depth (Figure 3.3 A, B, C). The positioning took place via differential global positioning system (DGPS). The obtained results allowed conclusions on possible obstacles such as metal scrapes, old wiring or remains of buildings in the upper 6 m, that should be bypassed to assure drilling clearance when establishing experimental set ups. Old wiring was located running from the north east to the south west of the test site. This part has been excluded from further exploration. The northwest border area showed prominent anomalies. Small scale anomalies have been allocated over the whole test site area and very prominent ones in the center. High anomalies indicated anthropogeneous or earth deposits. Those areas have also been excluded from further exploration [Dahmke et al., 2021].
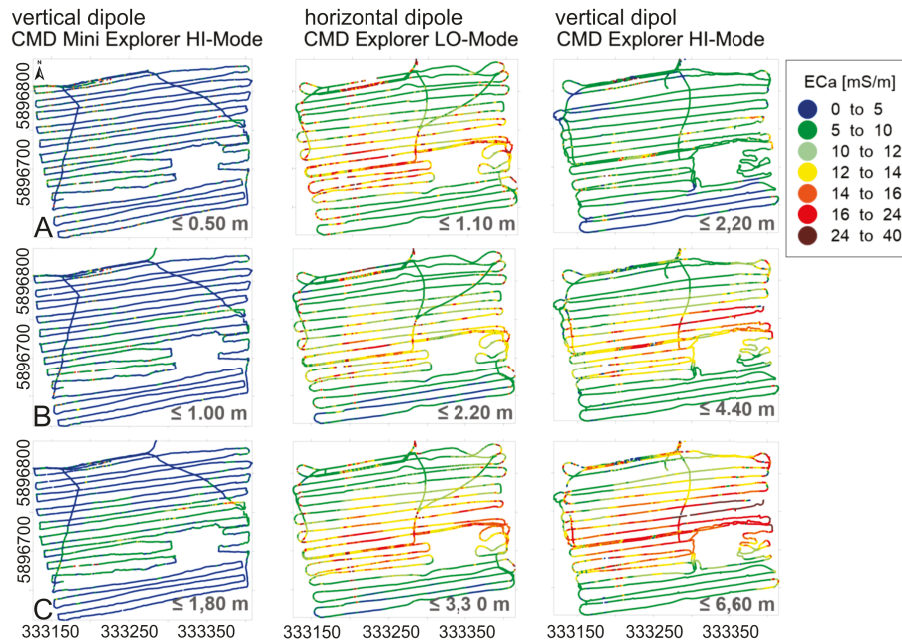
Figure 3.3: Electromagnetic induction survey with different coil separation and hence different depths of investigation. HI-Mode stands for vertical-dipole and LO-Mode for horizontal dipole respectively. The inter-coil spacing for the CMD - MiniExplorer is 0.32 m, 0.71 m, 1.18 m, and for the CMD - Explorer the inter - coil spacing is 1.48 m, 2.82 m, 4.49 m.

3.1.2 Electrical resistivity tomography (ERT)

The evaluation of the electromagnetic measurements lead to the location of six ERT-profiles. They have been layed out from North to South and West to East directions between 110 m and 270 m length (Figure 3.4). A multi-channel system (Resecs, Geoserve, Kiel) in Wenner α configuration with an electrode spacing of 1 m has been used. The measurements provided an initial stratigraphical information of the upper 2 m [Hausmann, 2013, Lamert et al., 2012, Peter et al., 2012]. With the Boundless Electrical Resistivity Tomography Software (BERT), based on the pyGIMLi core libary, we obtained 2D plots that showed the distribution of earth deposits and excavated material at the near surface. They allowed first estimations of near-surface homogeneity (Figure 3.5). The resolution of the measured resistivity decreased with depth. High resistivity anomalies in the near surface indicated deposits with anthropogeneous origin (P01, P04). They occurred less often in the central part of the field site. We identified zones that have been free of interference. They obtained priority for further geophysical surface exploration [Dahmke et al., 2021].

ERT Arrays along the test site

We installed several ERT configurations on the test site to obtain electrical conductivity and sensitivity information at different depths. Their locations are outlined in Figure 3.4. The Wenner α configuration showed, as one of many, a comprehensive picture of the test site.

- P01 - Wenner α, a = 18 m, path at 159-161 m spread: 0-268 m, W-O

- P02 - Wenner α, a = 18 m, spread: 200 m N-S

- P03 - Wenner α, a = 18 m, path at 128 m. 131m, spread 0-223 m, W-O

- P04 - Wenner α, a = 18 m, spread 0-118 m, N-S

- P05 - Wenner α, a = 18 m, path at 134,5 - 137 m, spread 249 m, N-S

- P06 - Wenner α, a = 30 m, spread 111 m, W-O

Figure 3.5 shows the results of the electrical resistivity measurements with additional topographic information. We find a generally homogeneous subsurface overlaid by high impedance deposits (wires, earth deposits, paths) at several locations. Those areas are excluded from further measurements.

3.1.3 Hydraulic Profiling Tool & Electrical Conductivity

Hereinafter we combined EM and ERT information with a high-resolution vertical characterization and parametrization of the aquifer using direct push (DP) technologies. In Figure 3.6, the important parts for hydraulic and electrical
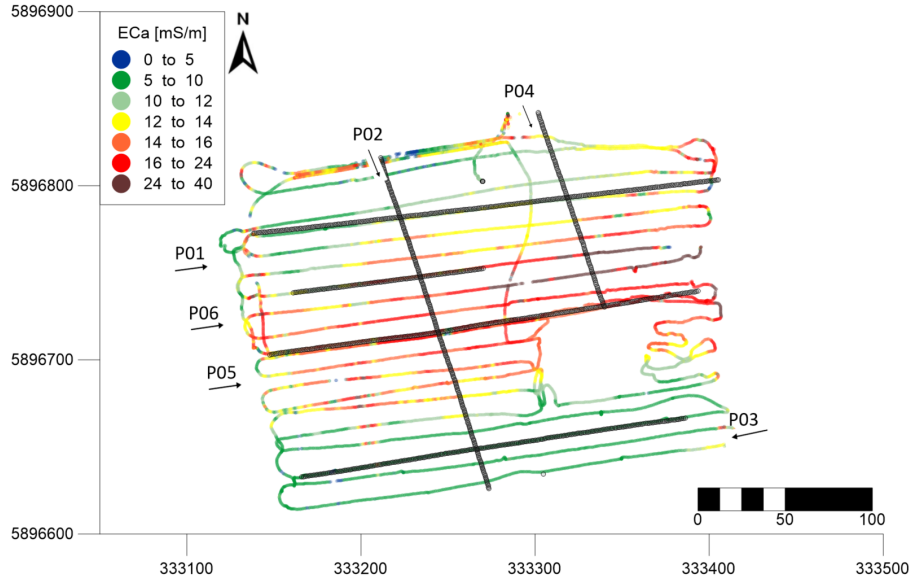
Figure 3.4: The location of additional electrical resistivity measurements (P01 - P06) was based on electromagnetic exploration results using the CMP Explorer in HI-Mode exploring depths $\leq 6\,\mathrm{m}$. The profiles extend in different directions.

profiling are marked. Measurements with the hydraulic profiling tool (HPT) [Dietrich et al., 2008] and electrical conductivity log (EC) resulted in a depth orientated stratigraphical interpretation.

The HPT defines stratigraphic units with different hydraulic properties listed in (Table 3.1). The probe, installed on a 1,5" rod, is being pushed and hit with a sounding-speed of $20\,\mathrm{mm/s}$. During that process water is injected into the subsurface via a lateral filter to capture line pressure and flow rate (Figure 3.6 D). The injection rate varied between 12 to 15 l/h. The ratio of flow rate Q_f and pressure P (corrected for hydrostatic and atmospheric pressure) lead to a relative hydraulic conductivity $k_f = \frac{Q_f}{P}$. High pressure and slow flow rate correspond to low permeable sediments (silt), and low pressure and high flow rates indicate high permeable sediments (sand). To calculate the accurate injection pressure P, the total pressure (sum of hydrostatic, injection, and atmospheric pressure) need adjustment by atmospheric and hydrostatic pressure. To characterize whether an aquifer is confined or unconfined, recording the static pore water pressure at every depth is necessary while the sounding stops and comparing the slope of the curve. An additional four-point electrode array (Figure 3.6 E) detected the electrical bulk conductivity of the sediments. Those parameters are recorded every $15\,\mathrm{mm}$. The increased electrical conductivity shows an increased incidence of clay minerals in the geological subsurface. We must consider that the HPT only serves as a proxy for the hydraulic conductivity of the

25
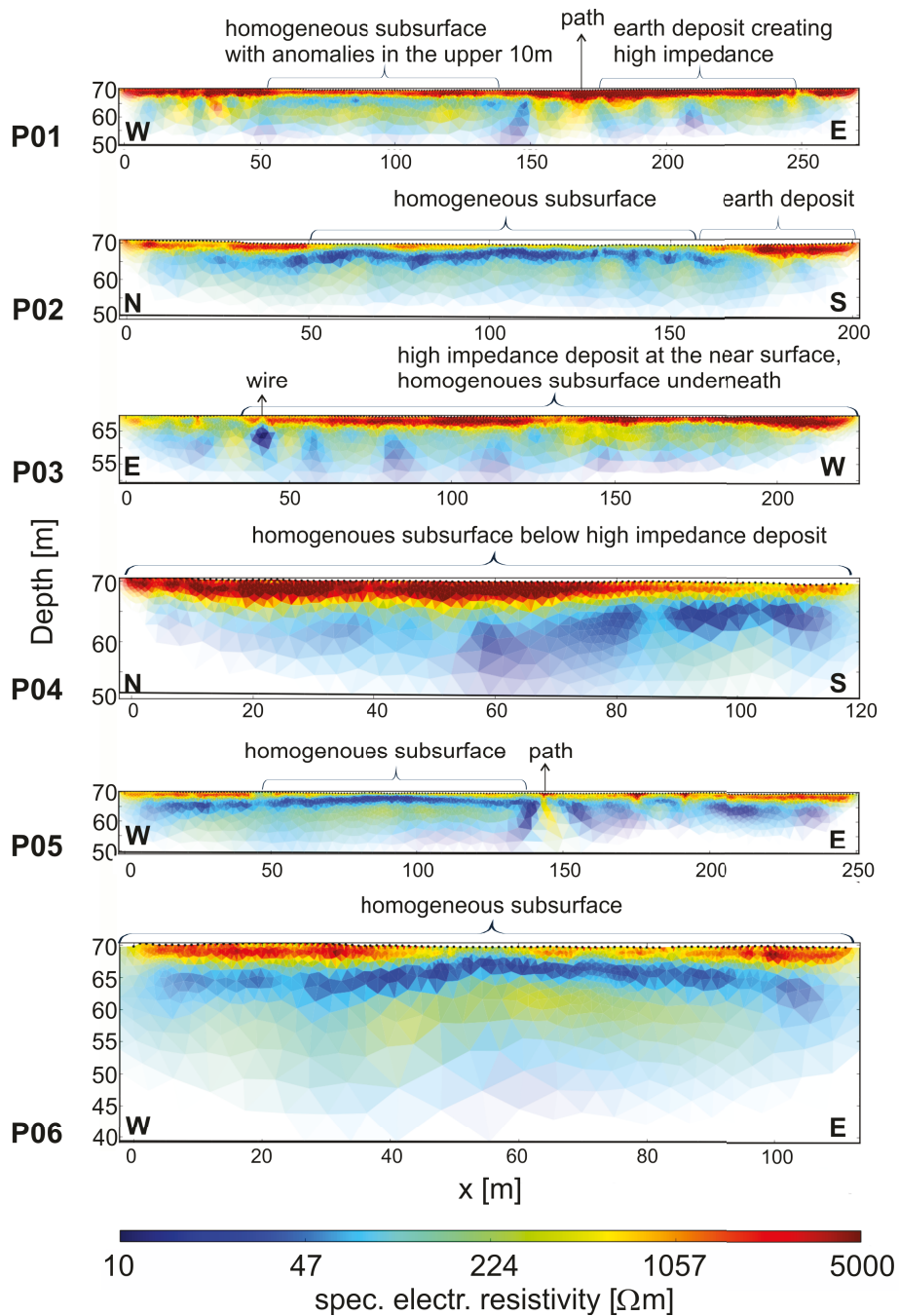
Figure 3.5: Inversion results of electrical tomography installed at the surface. High resistivity contrasts between 10 to 5000 Ωm.
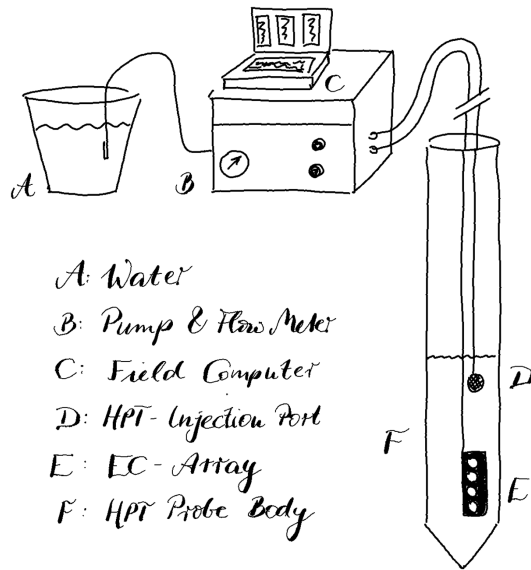
Figure 3.6: Scheme of a Hydraulic Profiling Tool (HPT). Water (A) flows into a pump and flow meter (B). From there it is being pumped trough the rod to the HPT-Injection Port (D). The injection pressure is measured. With the EC-Array (E) the electrical conductivity is measured with a four-point array.

subsurface in order to distinguish between different hydrostratigraphic layers.

Table 3.1: HPT parameters and information that can be attained by HPT measurements

Parameters to analyze	◇ depth ◇ electrical conductivity ◇ sounding velocity ◇ HPT pressure at the sensor ◇ flow rate ◇ atmospheric pressure ◇ Q/P ◇ ground water level
	◇ hydrostratigraphic units (Proxy Q/P) ◇ properties of the aquifer (confined, unconfined) ◇ ground water level

Exemplary results are visible in Figure 3.7 B. In the Northeast at MP002 we resolved a low-permeable area that indicates clayey-loam between 2 - 6 m depth followed by a hydraulic permeable layer with a low electrical conductivity be-
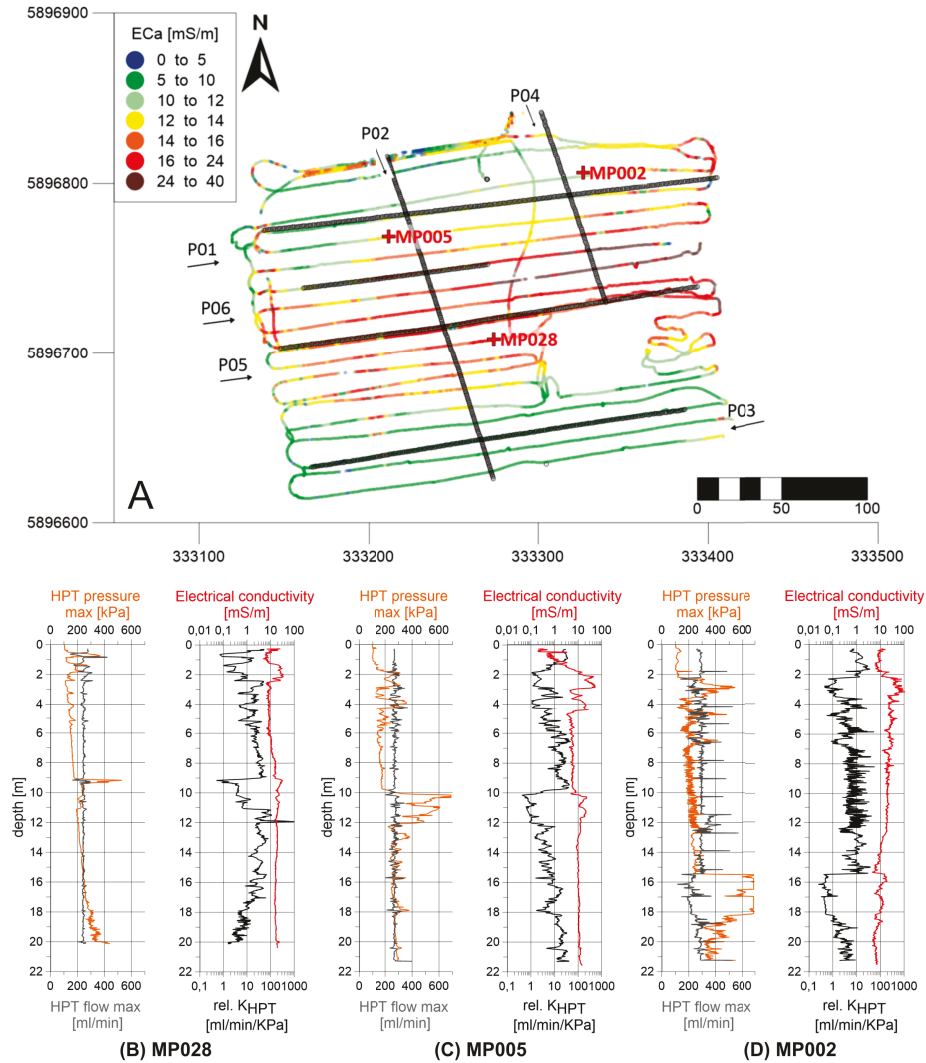
Figure 3.7: (A) The location of three selected HPT measurements is marked in red on the map of the electromagnetic conductivity up to $\leq 6.6\,m$ depth. (B-D) The HPT diagrams below show the HPT flow maximum (dark gray) together with the pressure maximum (red)on the left side and the relative hydraulic conductivity (black) together with the electrical conductivity (red) on the right side of the plot.

tween $6\,\text{-}\,15\,m$ that indicates an aquifer consisting of sand and/or gravel. At $15.5\,m$ depth, we identified a hydraulic low-permeable layer with slightly but not significantly higher electrical conductivity. The log of MP005 represents

28

the western area (Figure 3.7 B) with a high electrical conductivity contrast. Together with a substantial variation in hydraulic conductivity, we assume clay lenses are located close to the surface. Between 5 m and 10 m, the electrical conductivity has no strong variation. At 10 m, the log indicates a local maximum, together with the drop in hydraulic conductivity. Starting at 12 m going down to 21 m, there are only intermittent hydraulic low permeable areas that could indicate silty loam. The southwestern area, represented by MP028 (Figure 3.7 C) is characterized by alternating hydraulic and electric conductive to non-conductive layers in the near-surface down to a depth of 3 m. From 6 m to 9 m depth, all probings show constant hydraulic and electric conductivity. From 9 m to 12 m, the hydraulic conductivity drops. The electrical conductivity shows only a slight deflection. It stays relatively constant until end of sounding, whereas the hydraulic conductivity decreases with depth. The western, especially the southwestern part holds distinct low-permeable layers only deeper than 12 m. The example results of the HPT elucidate the geological variability of the whole area. According to the adaptive approach, we defined areas for core sample collection to verify the hydraulic and electrical profiling results. The EC- and HPT-logs enable the detection of hydraulic low-permeable layers and areas with geological homogeneity. Those homogeneous layers are suitable areas for the injection experiment. They are additionally easy to identify and parameterize. The HPT approach provides continuous hydraulic conductivity information [Dahmke et al., 2021], which enables us to correlate the measured HPT values with the absolute hydraulic conductivity from reference measurements such as slug-tests (3.1.4).

3.1.4 Slug test

We conducted and evaluated slug tests [Butler, 1997] at distinct groundwater observation wells (Figure 3.8). Within the defined test sites, slug tests help to reference the hydraulic conductivity results. With the absolute hydraulic conductivity values, aquifer connections within the whole area can be detected to prove whether an aquifer is confined or unconfined. We conducted the measurements within a 2" high-density polyethylene (HDPE) well that was filtered along two meters at a specific depth. The results are listed in Table 3.2 and 3.3. The slug test at MP002 shows a confined aquifer situation with hydraulic contact between the upper and the lower aquifer. The slug test at MP028 shows an unconfined upper aquifer and a slightly confined lower aquifer. They are detached from each other. The results correlate well, with the sediment core analysis (Chapter 3.1.5). By analyzing the groundwater observation wells we identified the thickness of the aquifer (Table 3.3).

3.1.5 Core analyses

In the last step, we gathered sediment core samples with the drill (SonicSamp-Drill). Core samples help to validate the hydrogeological evaluation and support
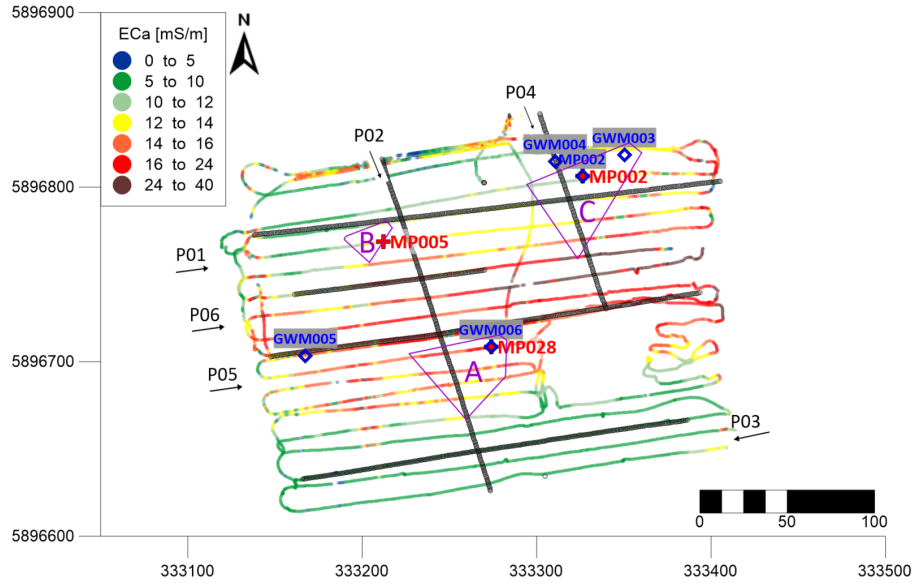
Figure 3.8: This map shows the three selected test sites marked in purple (A: methane injection, B: hydrogen injection, C: heat injection). The blue diamonds mark the positions of wells where slug tests have been performed.

Table 3.2: Slug test results of MP002 and MP028

Well	Depth [m]	$kf[\frac{m}{s}]$	Description
MP002	10	$7,15 * 10^{-4}$	strongly medium grained sand, fine grained sand
	14	$7,04 * 10^{-4}$	medium grained sand, fine grained gravel
	17	$4,41 * 10^{-6}$	clayey silt
MP028	10	$1,9 * 10^{-5}$	Aquitard, silty fine grained sand
	13	$3,96 * 10^{-4}$	fine grained sand
	16	$4,29 * 10^{-4}$	fine grained sand

Table 3.3: Slug test results of the groundwater level wells (GWM003 - GWM006)

Well	$kf[\frac{m}{s}]$	Thickness aquifer [m]
GWM003	$1,79 * 10^{-3}$	5-20
GWM004	$6,27 * 10^{-5}$	6-18
GWM005	$8,02`10^{-3}$	3-10
GWM006	$4,34 * 10^{-3}$	11-20

the geological interpretation. We attain an informative picture of sediment parameters at a local scale and defined a suitable test site for methane-, hydrogen-

and heat injection experiments (Figure 3.11, 3.9, 3.10). We chose the test sites according to the most homogeneous architecture of the geological properties to configure the boundary conditions for our injection experiment as manageable as possible.
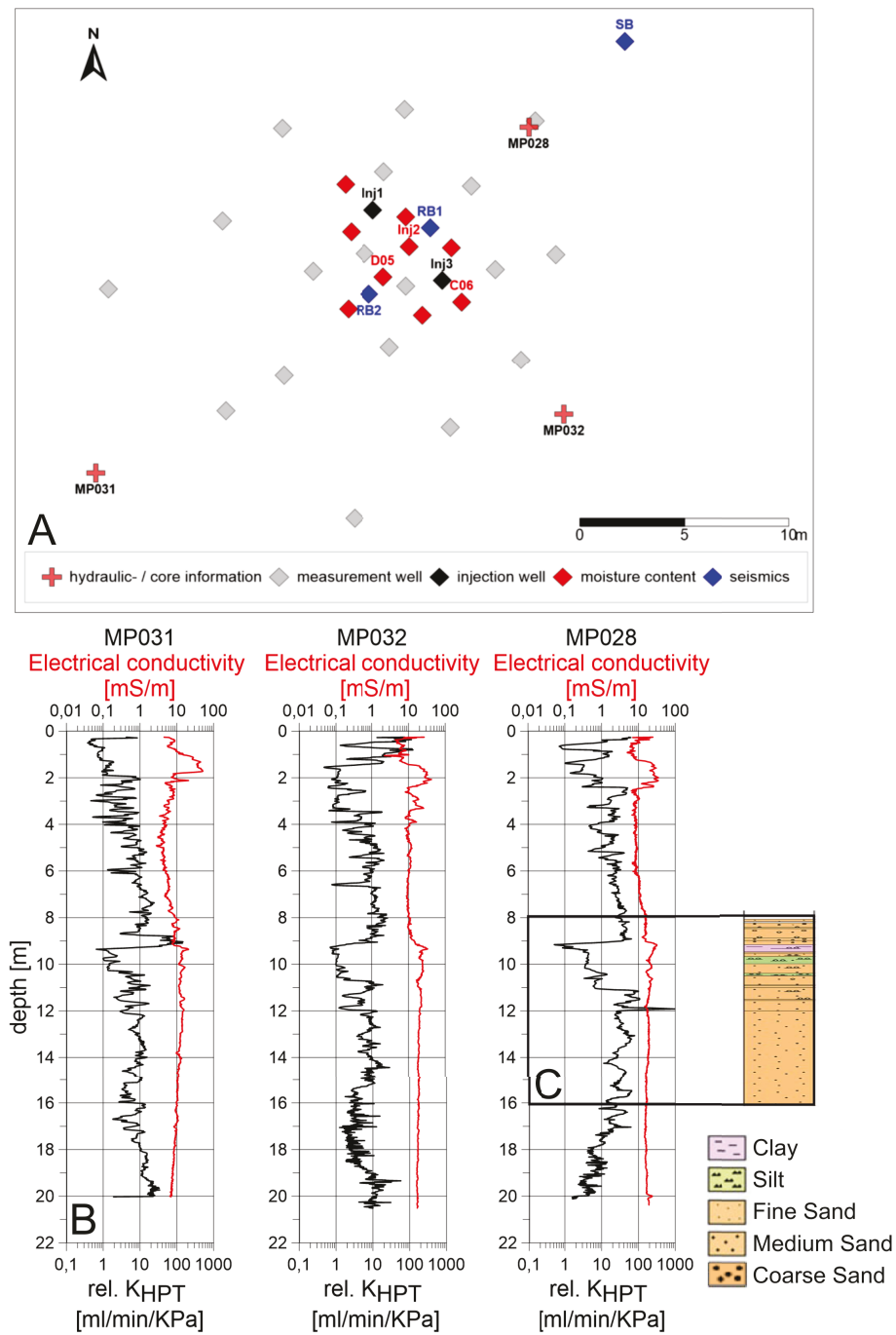
Figure 3.9: (A) CH_4 injection test site including soil moisture measurement wells, on the basis of the HPT- and sediment core analysis, (B) hydraulic and core information at designated wells, (C) Core information at MP28 with stratigraphic information
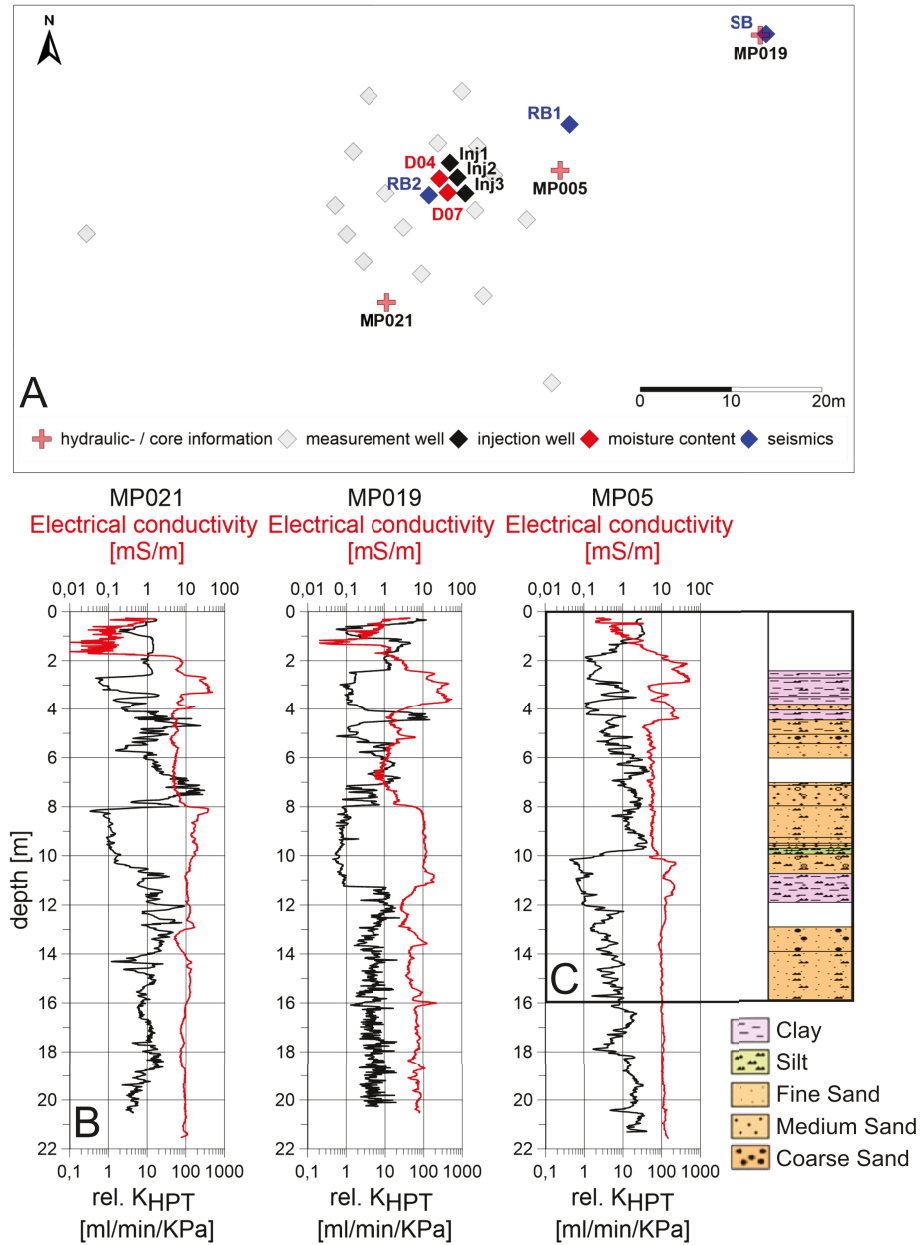
Figure 3.10: H_2 injection test site including soil moisture measurement wells, on the basis of the HPT- and sediment core analysis, (B) hydraulic and core information at designated wells, (C) Core information at MP05 with stratigraphic information
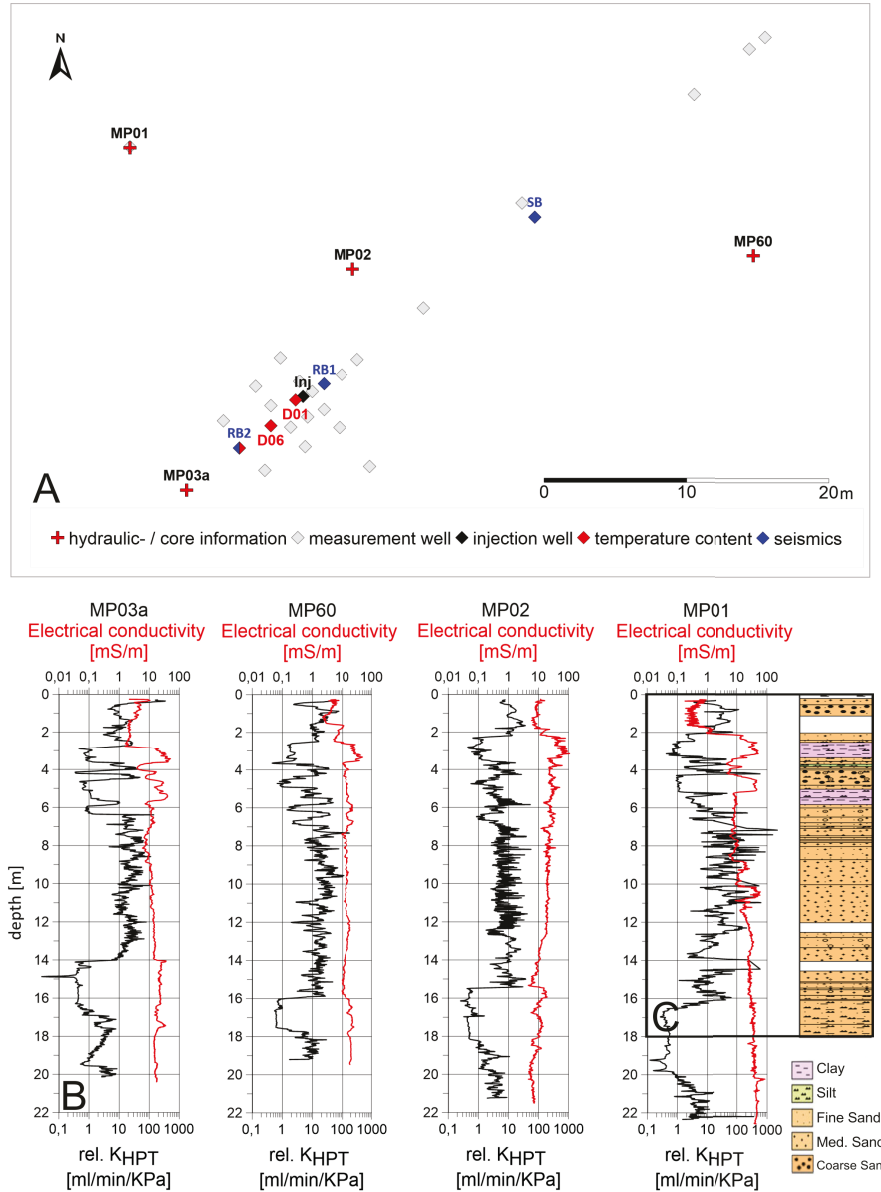
Figure 3.11: First heat injection test site including temperature measurement wells, on the basis of the HPT- and sediment core analysis, (B) hydraulic and core information at designated wells, (C) Core information at MP01 with stratigraphic information
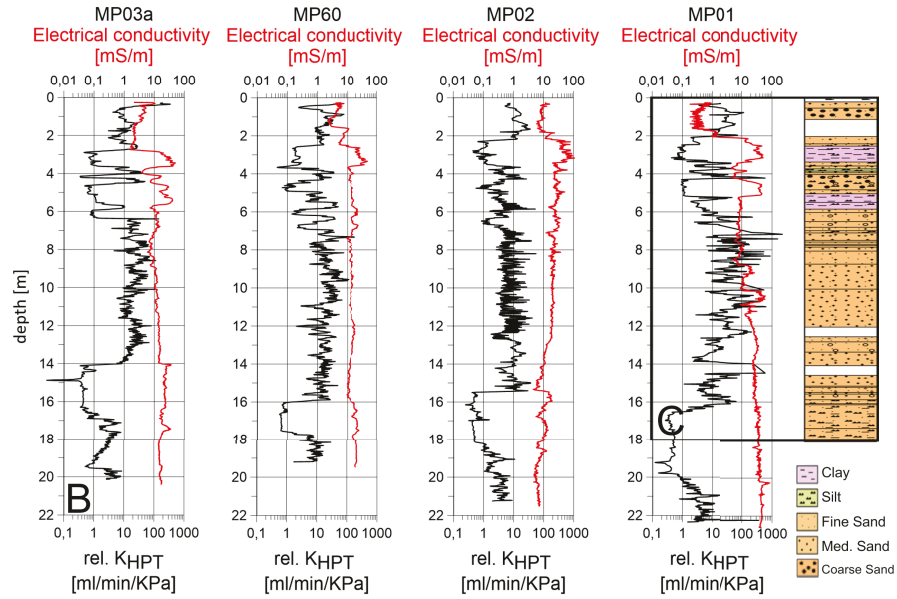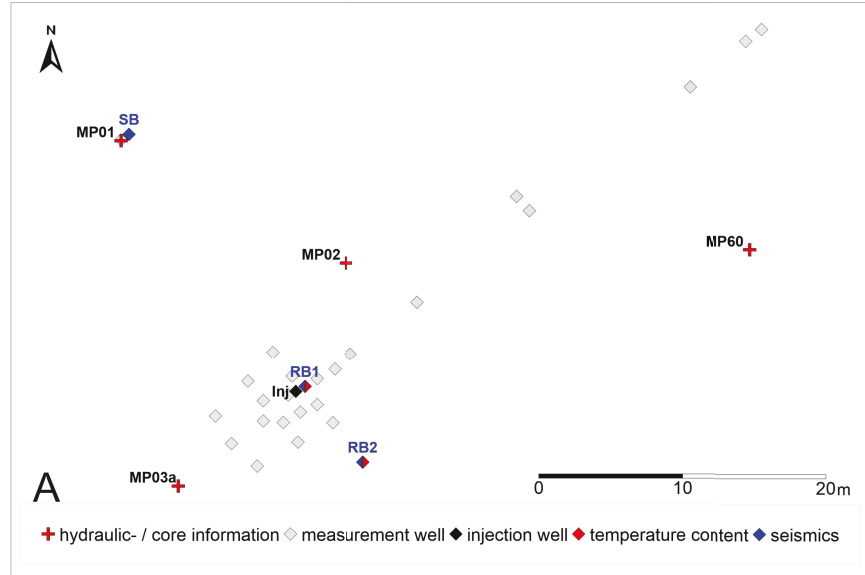
Figure 3.12: Second heat injection test site including temperature measurement wells, on the basis of the HPT- and sediment core analysis (B) hydraulic and core information at designated wells, (C) Core information at MP01 with stratigraphic information

3.2   Injection test site

The evaluated data of the preliminary investigation results in the definition of three test site areas (Figure 3.8). Field A is used for methane, field B for the hydrogen, and field C for the heat injection. The injection depths have been defined according to the encountered aquifer. Fugro Germany Land GmbH has done the construction of the injection installation. Figure 3.13 A, B shows the technical setup for both injection scenarios.

Methane injection test site

The sediment core showed coarse-grained sand on top, followed by a clay layer and subsequent fine-grained sand intermittent by clay and silt. The effective porosity obtained by sieve analysis from colleagues in Kiel averages to $\Phi = 0.2$. The horizon of fine-grained sand at 17.5 m depth with an injection lance filter length of 20 cm, was found suitable for a methane injection.

Hydrogen injection test site

The subsurface shows clay and silt material between a depth of 2.40 m and 4 m followed by a mixed silty to coarse-grained sand layering down to 10.80 m. From 10.80 m to 12 m depth, we find another clay boundary. Followed by relatively homogeneous coarse-grained sand. The effective porosity obtained by sieve analysis is $\Phi = 0.19$. The area between 12 m and 18 m is evaluated as suitable for the hydrogen injection. Three injection lances are installed at a depth of 18,20 m with a filter length of 20 cm.

Heat injection test site

The heat injection test site is located in the Northeast of the test field. The subsurface model shows anthropogeneous deposits mixed with sand in the upper 2 m. From 2,40 m to 5,80 m, a sorted clay-silt boundary can be found intermittently by coarse-grained silty sand. Starting from 5.80 m we find layered fine to coarse-grained sand down to approximately 16 m depth, followed by silty material. Homogeneous domains of quarternary sand are located between 7 m - 14 m depth, followed by clayey material at 15 m. It locates the vertical boundary of our investigations. The low permeable areas are varying in depth (between 2 m - 7 m) and thickness (1 m - 3 m). The effective porosity obtained by sieve analysis to $\Phi = 0.21$. The horizon between 7 m and 14 m depth is suitable for heat injection experiment. The injection of the heated water via one well takes place along the whole range between 7 m and 14 m depth.

Construction

The **gas** is stored in a bottled reservoir at the surface. A mass flow rate regulator is controlled by the control unit with an integrated emergency shutdown to regulate the injection rate. An additional ventilation system has been installed or the hydrogen injection to ensure the evacuation of explosive gas. Gas is injected via three injection lances and emitted radially. Monitoring soil gas happens via self-constructed soil-gas-lances to see changes driven by possible gas migration (Figure 3.13 A).

For the **heat** injection, cold water is being extracted with an extraction rate of 15 L/min within a distance of 40 m to the injection location. It is pumped to a cold water tank and heated to 75°C using a heat exchanger. After pumping the water to a hot water tank, it gets injected via gravitational forces and a flow rate of 14.5 L/min to a target depth of 7 - 14 m. Thermocouples measured the temperature (red dots in Figure 3.13 B).

3.2.1 Prominence of the experiments

A decisive part of the work aims to the installation of the globally second CH_4 injection and first H_2 injection test site to provide a wide-ranging data basis for the initial spreading of gaseous methane and hydrogen in near-surface aquifers as well as its related geophysical, hydraulic, hydrochemical and microbial effects. It is additionally supposed to advance the data-based evaluation of the prediction excellence of geophysically, hydraulically, and hydrochemically affected temperature variations in lab- and field experiments. Close coordination with the project partners was necessary, as decisions had to be made based on previously achieved results. Parts of the tasks for which the individual groups were responsible are briefly presented.

Characterization of the test site - Geological and hydrogeological conditions

According to the regional geological conditions, the subsoil at the test site is characterized by glacial and glaciofluvial sediments of Quaternary age. The encountered layer are assigned to Saalian and Weichselian sediments
[Peter et al., 2012]. An aquifer with low permeable interbeddings of different grain sizes (clay, till, fine, medium, and gravel sand) reaches a depth of 10 m below ground. In app. 4 m and 12 m depths follow an interrupted hydraulic low permeable layer with variable thickness of several cm right up to 2.5 m (silt - fine sand). Due to the interrupted nature of the low-conductivity layer, it can be assumed that there are hydraulic connections between the aquifers. A second relatively homogeneous aquifer is located between 10 - 21 m depth. According to the HPT/EC-Logs varies, the aquifer in depth and thickness. Its base is formed by a horizontal low permeable layer identified as boulder clay
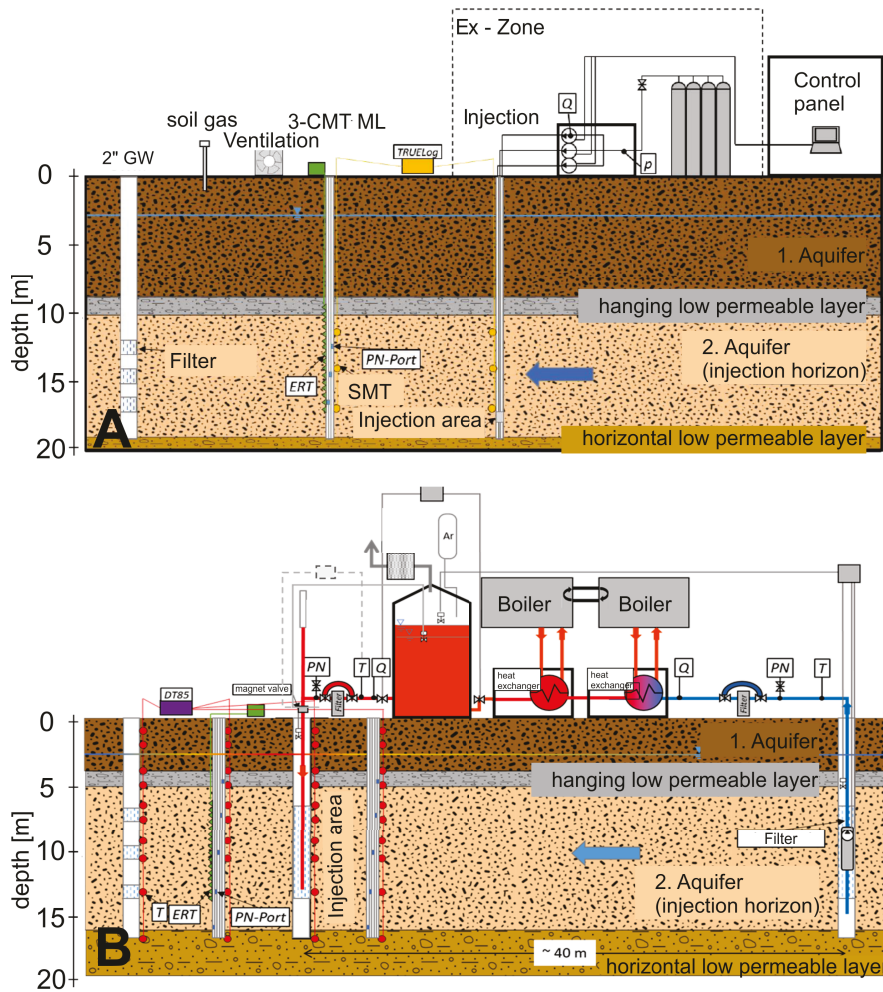
Figure 3.13: Schematic view of A) the gas injection installation and B) the heat injection installation. Changed after [Dahmke et al., 2021]

in [Peter et al., 2012]. Performed soundings were able to detect those layer between 14 m - 20 m depth in the northern and central part of the test site. However, it was not recorded down to a depth of 21 m in the western and southern area. Based on core analysis, electrical- and hydraulic profiling logs, a geological structural model (Figure 3.14 has been constructed by colleagues in Kiel [Dahmke et al., 2021]. The data, logs of our pre-investigation, and model served as a basis for the work of our project partner research groups. A mapping of the hydraulically low conductive layers was done using the sediment cores. The hydrogeological conditions show an east-west directed groundwater flow with a groundwater depth of about 3 m below ground level. Determinations of the hydraulic gradients based on spot day measurements of groundwater levels. According to field test observations, values in the range of 0.10 m/d can be assumed. The characterization of the test site happened in collaboration with the Geoscience Department of the University of Kiel and the Department of Isotope Biogeochemistry of the Environmental Research Centre (UFZ) in Leipzig. Geophysical exploration, hydraulic- and core information are obtained by the Monitoring- and Exploration Department at the UFZ Leipzig.
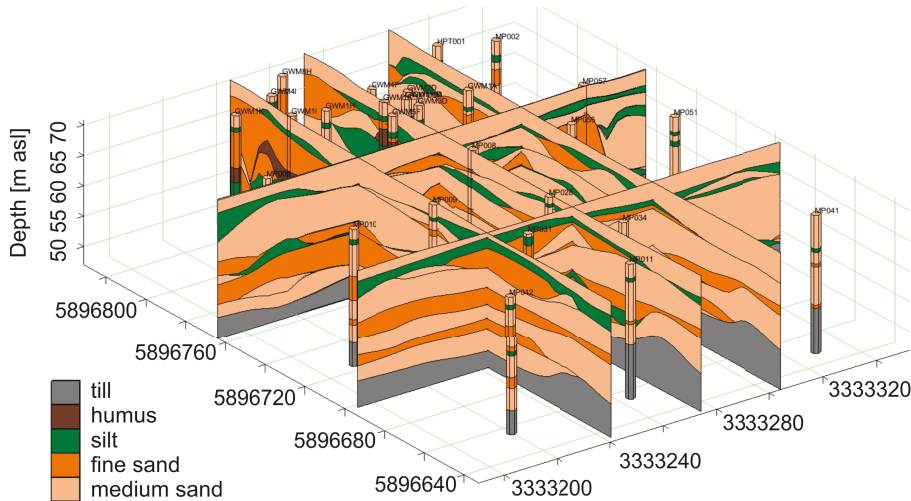
Figure 3.14: Broad structural model of the whole test site based on core analysis and depth orientated logs [Dahmke et al., 2021].

Geohydromodelling, Kiel

The hydraulic- and thermal characterization of process parameters has been done with field investigations and lab analyses. That resulted in developing and applying of numerical models regarding gas and temperature distribution and

induced pressure changes at the test sites. Thermal- and hydraulic processes have been coupled to allow for density-driven convection. The prediction of temperature distribution has been accomplished using numerical finite-element-process models OpenGeoSys by coupling the temperature-dependent groundwater flow and the heat equation. Isotrope and anisotrope permeability has been anticipated. Forecast simulations of the pressures, gas saturation and solute concentrations have been done with ECLIPSE (Schlumberger). Those prediction models have later been used for comparison with the experimental field data. After installing a monitoring network (Temperature, Soil Moisture) on the basis of numerical modeling, continuous temperature, pressure, water saturation and solute concentration measurements were performed. The injection rates, supply temperature, water pressure, and saturation in the surrounding geological layers have been measured continuously and spatially distributed during the injection. [Heldt et al., 2021b] documents results examining the heat injection experiment. [Hu et al., 2023] presented results of the cross-well multilevel pumping test.

Aquatic Geochemistry and Hydrogeology, Kiel

To ensure the acquisition of hydrogeochemical effects during the field experiments, the characterization and parametrization of induced geochemical processes depending on different temperature- and gas injections have been done in lab experiments using provided test site material. They complied with the monitoring of spatial and temporal variations of the groundwater chemistry by heat- and gas injections in the field. Their work considered lab- and solid-phase investigations with sediment of the aquifer as well as different sediment-groundwater combinations and pressure conditions. There has also been groundwater sampling to detect geochemical heterogeneity. Detecting the variability of the geochemical conditions and the distinction and classification of heat- and gas-induced concentration changes have been another important aspect. Relevant rock parameters such as density and porosity have been identified in the lab.

Department of Isotope Biogeochemistry

The investigation of the test site's microbiology and isotope geochemistry behooved the Isotope Biogeochemistry Departement. They validated methods for fast and sensible detection of micro-biological gas oxidation processes in the near-surface using isotope monitoring. The detection of microbiological gas reactiosn by analyzing microbial communities and the detection of heat-induced variations of microbial diversity has been realized. Microbiological studies on the effects of gas and heat inputs on various microorganisms, soil gas, groundwater sampling, and isotope analyses were carried out. The monitoring results of spatial and temporal hydrogeochemical and isotope-chemical plume evolution downstream of the gas phase and induced heat processes (up to 80°C) as well as the analysis of induced effects on follow-up processes with associated influ-

ence on the microbial aquifer community can be found here [Löffler et al., 2022], [Keller et al., 2021].

Department of Soil System Science

Colleagues conduced to the evolution of experimental models and numerical dimensioning as well as the interpretation of the field experiments. They promoted prognostic multi-phase simulations for observing the gas phase's propagation behavior in the field scale and small scale lab-experiments to estimate permeability - saturation relations using μ-CT analysis. Together with the parametrization of the models, they took gas trapping and the solution of the residual gas phase into account [Zulfiqar et al., 2020].
[Geistlinger and Zulfiqar, 2020] studied the influence of wettability and surface roughness on fluid displacement in detail, whereas a simplification will be applied here, that the injected gas displaces the fluid phase.

4

Crosshole Seismic

> The saddest aspect of life right
> now is that science gathers
> knowledge faster than society
> gathers wisdom.
>
> Isaac Asimov

4.1 Concepts of seismic crosshole monitoring

Common surface seismic approaches such as reflection and refraction measurements failed due to the high energy absorbing near-surface. Seismic borehole measurements are also usual investigation methods when characterizing the subsurface. Seismic transmission enables us to monitor controlled subsurface variations in a confined area. One application is the VSP, where the source is whether located at the surface with an offset to the wellhead and the receivers got clamped onto the borehole wall or the source is located in the well, and conventional geophones detect the signal at the surface. Cross-hole tomography is another borehole application where the receiver and source are located inside different boreholes. Different types of sparkers can serve as sources when operating below the water table. As receivers serve hydrophone chains or single hydrophones according to the measuring purpose. Such a tomography can be focused on a simple transmission measurement, where the source and receiver are acting in the same depth to evaluate relations and dependencies of rock physical parameters on seismic properties. The still sparsely used seismic crosshole techniques are applicable to monitor changes in reservoir conditions and gas injections [Ng et al., 2019]. As already mentioned in 1.1.4, we benefit from an interpretation independent from the source signal while also being decoupled from surface noise by applying the cross hole set [Diallo, 2000]. Here, we decide to apply a cross-hole seismic set-up to acquire the velocity and amplitude of P-waves between receiver boreholes by analyzing data of the horizontal transmission.
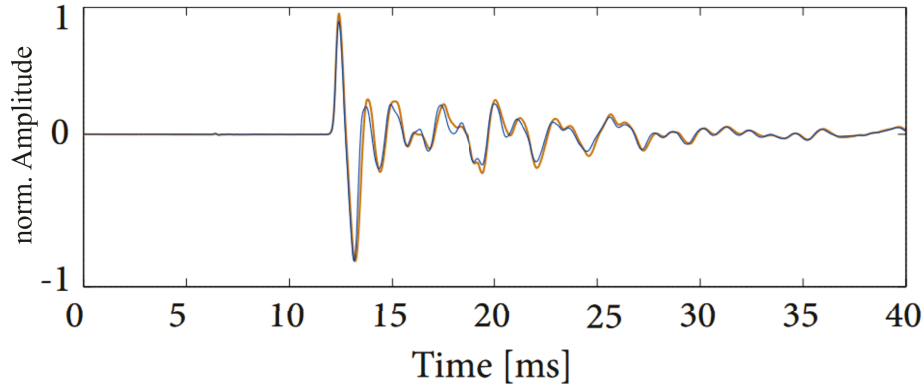
Figure 4.1: Signal repeatability of the SBS 42 P-Wave Source (Geotomographie GmbH)

The source and the two receiver hydrophones are located at the same depth in three boreholes analogical to a tomographic setup with $\overline{RB1RB2} \ll \overline{SBRB1}$. The shot energy is recorded in two boreholes simultaneously at each depth and analyzed for horizontal transmission. That enables us to monitor controlled subsurface variations in a delimited area [Birnstengel et al., 2024].

Seismic source: [Winbow, 1991] investigates the benefit of airgun and explosive sources. The author evaluates both sources by comparing signal strength and the creation of unwanted tube waves. Airguns produce a radiation pattern which is difficult to extract from the data. With explosives, on the other hand, the casing will be affected by explosive sources, as will the formation of building microcracks. The signal, on the other hand, will be much stronger and get to formation directly without forming strong tube waves. [Rechtien et al., 1993] and [Ballard et al., 1991] recommend high-frequency sparker sources when operating in the shallow subsurface with small borehole separations. They are presenting performance tests on high-frequency borehole seismic sources.
[Hardee et al., 1987] state that the energy of the source is not getting lost to surface waves. The energy of borehole sources is smaller than surface sources, but we also need less energy since we are already in the formation we want to explore. The authors developed a downhole controlled seismic source that generated polarized shear waves. The experiments at our test site would have profited from additional shear waves in order to resolve geotechnical parameters and impedance. We suffered limitations in the borehole size so that we could not test the behavior of shear waves on injected gas or heat in the near-surface.
A source borehole (SB) and two receiver boreholes ($RB1$, $RB2$) are installed inline. The gas and heat injections takes place between $RB1$ and $RB2$ (Figure 3.11, Figure 3.9, Figure 3.10, Figure 3.12). The small distances (Table 4.1 column b) between $RB1$ and $RB2$ allow a detectable gas saturation (tempera-

ture) change in the area. We focus our measurements on the upper area between
8/10 - 13/18 m depth based on the preconditioned models of gas and heat mi-
gration [Dahmke et al., 2021]. SB is equipped with a borehole sparker SBS42
generating a highly repeatable P-wave. The signal is provided by an impulse
generator IPG5000 (Figure 4.1) that operates at 5 kV for high voltage power
supply, manufactured by Geotomographie GmbH, Germany. Two hydrophone
strings (BHC4 from Geotomographie GmbH) with 17 / 24 hydrophones of small
diameter are mounted into $RB1$ and $RB2$ accordingly from 8/10 m - 13/10 m
depth with a hydrophone spacing of 1 m. We released a first set of ten shots
at the lowermost depth, and the sparker was pulled up with a shot increment
of 1 m (Figure 4.2). In both receiver boreholes, we recorded and stacked 10
shots for each depth during the baseline measurement and every monitoring
cycle in order to increase the signal-to-noise ratio. Our sampling interval was
20.833 μs, and the recording covered 30 ms. Source and receivers were acting
below groundwater for coupling reasons. The wells siltation process restricted
our operational depth to 13 m during methane injection, 17 / 18 m for hydro-
gen injection and 14 / 15 m during heat injection [Birnstengel et al., 2024]. In
order to obtain comparable data for time series measurements, and assure data
quality and repeatability, all baseline and monitoring measurements have been
repeated throughout their whole execution. A complete dismantle and rebuilt
of the seismic cross-hole setup was done to verify reliable detection at the hy-
drophones and to exclude manual handling errors throughout the measuring
process. The raw data consists of a total number of 48 traces per time step for
six different depths. We resorted the data to account for horizontal transmis-
sion. At every depth, we are looking at six different traces per receiver borehole
[Birnstengel et al., 2024]. The concept of seismic cross-hole measurement (Fig-
ure 4.2) is transferable to all test sites.

Table 4.1: Layout Injection-Experiments

Experiment	a [m]	b [m]	operating depth [m]
Methane Injection	17	4	8 - 13
Hydrogen Injection	24	17	10 - 18
Heat Injection 1	18.8	7.5	8 - 15
Heat Injection 2	21.5	6.6	8 - 15

4.2 Simulation of the P-wave for the gas injection

The influence of gas on the P-waves travel time behavior can be replicated by
a simplified model simulation (Figure 4.3, Figure 4.4). Therefore, we used the
2.5D finite-difference time domain program FDBH (Finite Difference BoreHole),
originally developed by Thomas Bohlen and described by [Randall et al., 1991].
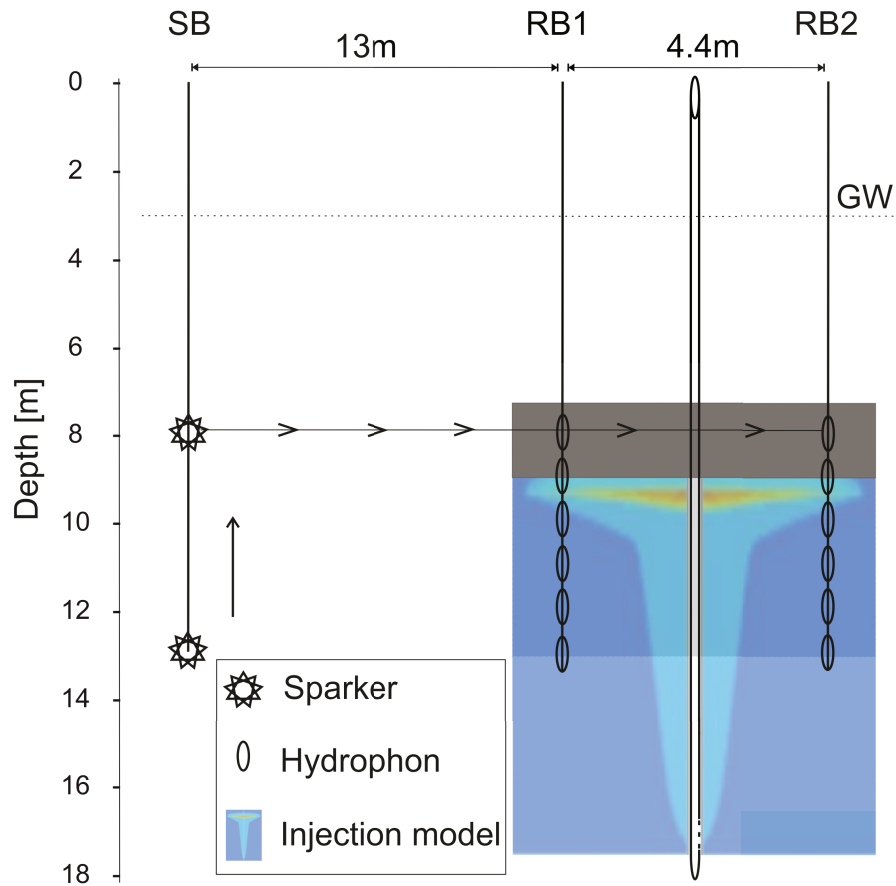
Figure 4.2: Conceptual layout of seismic cross hole monitoring, here exemplary for the methane gas injection.

It has been extended by [Hellwig, 2017] and is used to simulate the propagation of seismic waves in and around boreholes. Details about the program that is based on the velocity-stress formulation of the seismic wave equation are available in [Hellwig, 2017].

For the model, we used the following parameters:

Model dimension

- Dimension x: -5 m - 25 m, z: 0 m - 15 m
- Source (star): 8 m - 13 m depth
- Two receiver bohreholes with distances of 13 m, 17.4 m to the source borehole
- Two hydrophone chains (triangles) from 8 - 13 m depth each
- source pressure rate is first deviation after time of a bell curve, main frequency: 4.8 kHz

Material parameter

- unsaturated sand: 0 - 2.5 m depth, v_P= 800 m/s, v_S=500 m/s, ρ=1800 kg/m3
- transition zone: 2.5 m - 3.0 m depth. Linear interpolation between saturated and unsaturated material
- saturated sand: 3.0 m - 9 m depth, v_P=1630 m/s, v_S=420 m/s, ρ=1900 kg/m3
- silty clay: 9 m - 11 m depth, v_P=1760 m/s, v_S=360 m/s, ρ=2000 kg/m3
- saturated sand: 11 m - 15 m depth, v_P=1630 m/s, v_S=420 m/s, ρ=1900 kg/m3
- gas-water saturation lens: central area ("white spot") radial gas concentration decrease to 5 m lateral extend, injection at z = 12 m , x = 14.5 m from source, v_P= 800 m/s, v_S=430 m/s, ρ=1850 kg/m3

On the right side of Figure 3, we can clearly see the gas influence on the waves' travel time below the low permeable layer. In Figure 4, the P-wave simulation in 13m depth, refraction and reflections, also within the low permeable layer, are occurring.

The simulation in Figure 4.3 and Figure 4.4 show the P-wave travelling radially from the source. Reflections occur at, and within the clay boundary (low permeable layer), as well as at the groundwater surface. We can see another reflection occurring when the wave travels from the water-saturated,- to an unsaturated medium at the groundwater level. The wave travels faster through the low permeable layer. Refractions occur at the silty clay and water-saturated boundary. When the P-wave enters the gas-water-saturated zone, velocity is slowed noticeably right underneath the low permeable layer, where the gas will likely be "trapped". We assume gas being detectable in the P-waves signal. A head wave radiates with low amplitude. We see less influence from surface
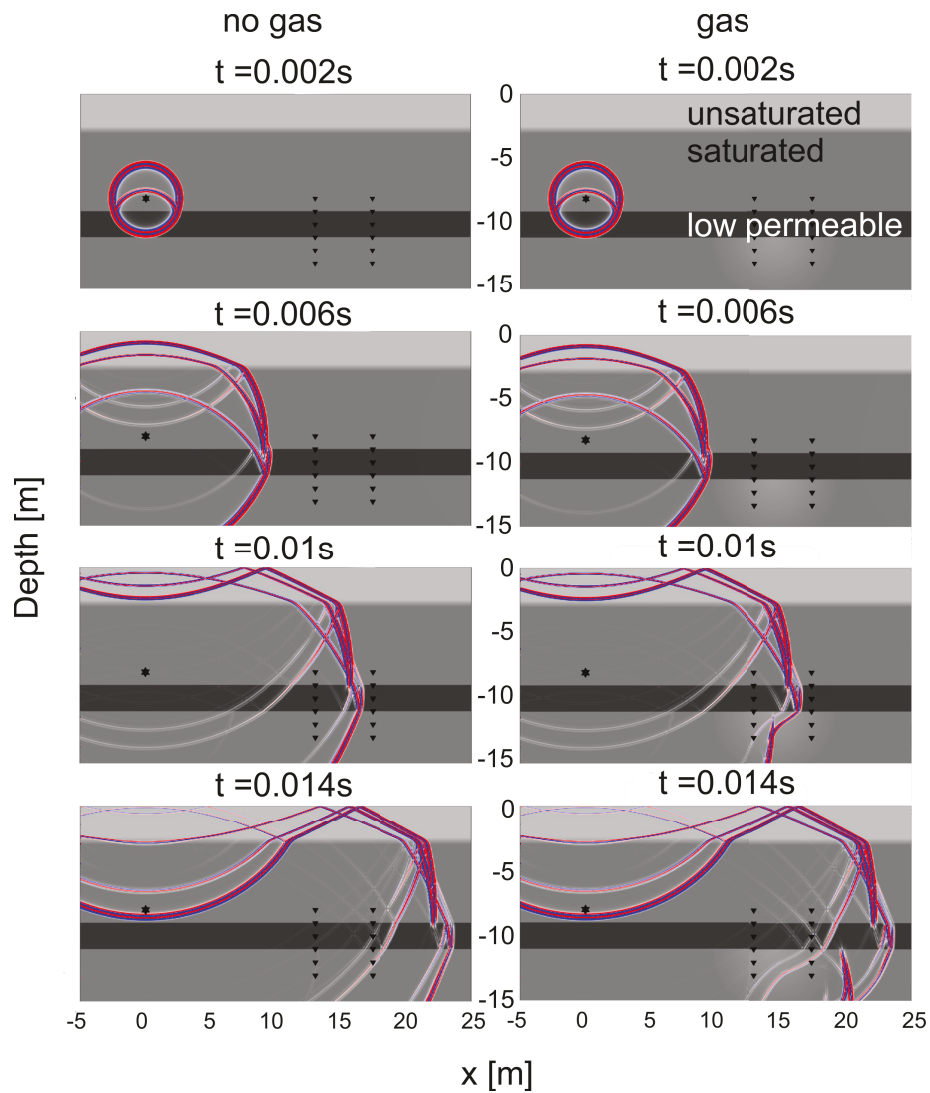
Figure 4.3: Simulated P-wave travel path for shot at 8 m depth (left) with gas lens center at x = 14.5 m, z = 12 m (right) [Birnstengel et al., 2024]. The different gray scales indicate an unsaturated zone at the top followed by a water saturated zone that is intermitted by a low permeable layer.
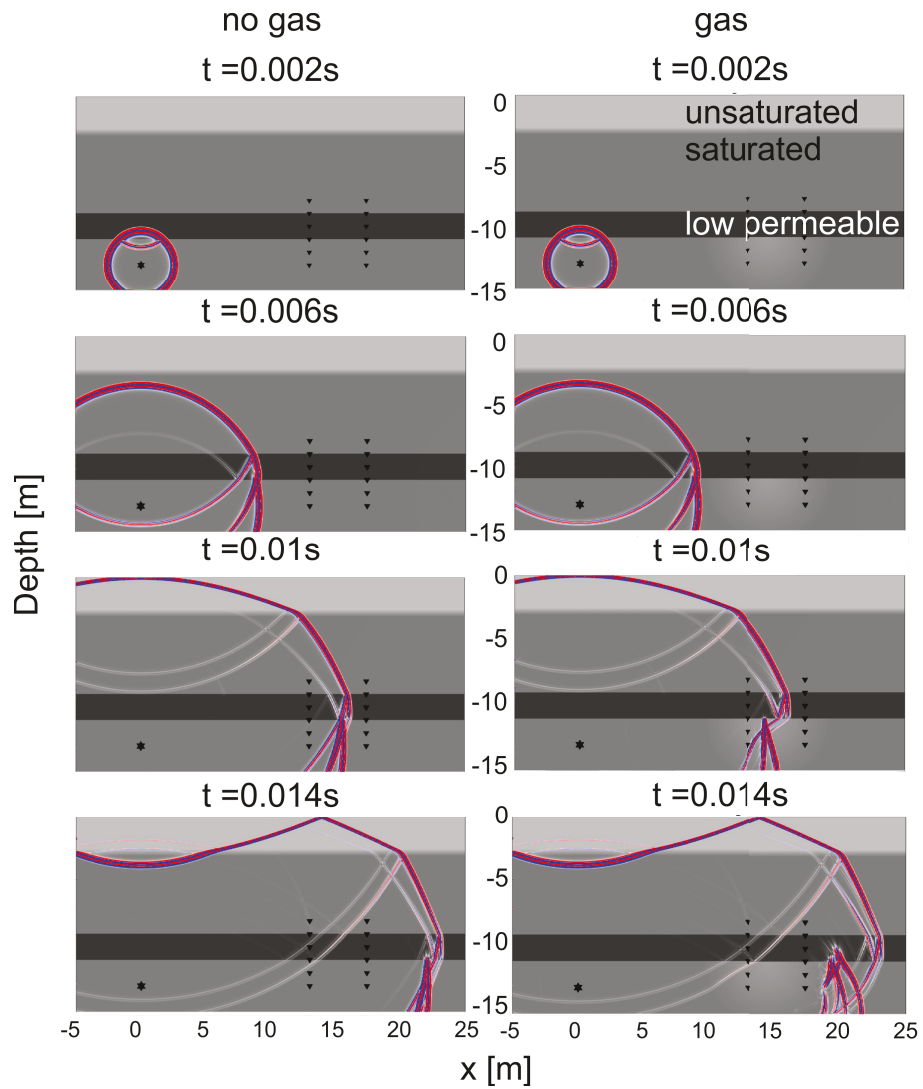
Figure 4.4: Simulated P-wave travel path for shot at 13 m depth (left) with gas lens center at x = 14.5 m, z = 12 m (right)
[Birnstengel et al., 2024].

reflections in Figure 4.4. The model shows that we can not assume 1D conditions. Refracted waves along the boundary between the low permeable layer and the sandy aquifer become obvious. Therefore we consider conducting a time-lapse study, where comparisons between the baseline and the monitoring cycle account for changes in the subsurface [Birnstengel et al., 2024].

4.3 Monitoring

The whole monitoring comprises one baseline- and several monitoring measurements. All measurements have been conducted twice. After the first cycle of shooting 2 x 10 shots at every depth, the source and receivers have been fully recovered and deployed a second time. The measurement was repeated to avoid errors due to manual handling. The injection takes place over a few days due to the injection rate (Table 4.2).

Table 4.2: Timeline of the methane, hydrogen and first heat injection with baseline, injection and monitoring dates

	Baseline	Injection	Monitoring [days after injection]						
Methane	30.04.2019	14. - 16.05.2019	5	18	49	251	277	294	355
Hydrogen	22.01.2020	28. - 30.01.2020	4	18	35	96	441		
Heat	30.04.2019	23.05. - 28.05.2019	7	36	266	282	344	687	

Table 4.3: Timeline of the second heat injection with baseline, injection, extraction, standby duration times in days and number of cycles

	Baseline	Phase	Heat	Standby 1	Extraction	Standby 2	Cycles
Heat2	09.06.2021	1	14 d	21 d	14 d	7 d	3
Heat2	09.06.2021	2	14 d	-	14 d	-	3

4.4 Data Processing

Assuming 1-D conditions in the subsurface and small geological contrasts between the layers, we neglect reflections within them. We detect the P-wave's first arrival in the receiver boreholes $RB1, RB2$.

Quality check (QC)

The QC of the data is the first step for evaluating the data's potential. Shots with coupling problems of the source or the receiver, high SNR due to ongo-

ing work at the surface, bad trigger connection, bad channels due to receiver damage, bad shots due to a weak source signal or recording failures have been cleared from the data.

Travel time analysis

The data has not been filtered to preserve all information of the borehole measurement. For each experiment, we gain two datasets of ten stacked seismograms per operation depth. Hence, we validate the data repeatability and increase the SNR. The apparent P-wave velocity is obtained by manual first break picking (FBP) with a picking accuracy of 2.5%. After proofing an impact of the injected gas on the signal at each borehole, we focus our velocity analysis on the area between two receiver boreholes. The absolute difference in apparent velocity will be evaluated over time and depth.

Amplitude analysis, energy and quality factor

To infer the gas-induced effect on amplitudes, we compare the maximum amplitude values from each monitoring time step to the baseline monitoring. Those results will be evaluated over time at different depth levels. The amplitude analysis is based on manually picking the signal's first local maximum for every baseline and monitoring cycle at every depth. Subsequently, investigating the variation of the average energy using the proportional coherence between energy and the square amplitude will help us to understand the energy distribution at each depth depending on the monitoring cycles. In addition, we analyze the quality factor Q, defined by: $2\pi E/\Delta E$ with $E = A^2$. The ratio of stored energy to dissipated energy [Schön, 2004,] is a useful indicator when analyzing the gas impact and attenuation properties on the seismic signal. We compare the energy in $RB1$ with the energy in $RB2$, so that $\Delta E = E_{RB1} - E_{RB2}$. In a second approach, we compare the energy stored in the baseline measurement with the energy still available in the monitoring cycles, $\Delta E = E_{\text{Baseline}} - E_{\text{Monitoring}}$.

Fresnel Volume

Travel time analyzes can only image changes that occur in the direct pathway. We can not assume 1D conditions to capture the amplitude since we integrate over a volume. Thus, we need to consider the Fresnel volume around the central ray. Based on the work of [Jordi et al., 2016] and [Watanabe et al., 1999], we calculate the weighting function for the Fresnel volume with our predominant frequency during the baseline measurement and a monitoring cycle. Due to the loss of high-frequency content from the source to the receivers, we simplify the

layout by calculating and comparing the Fresnel volume only with the highest measured frequency in $RB2$ during baseline and a monitoring measurement.

Water-content measurements

Water content has been directly measured with soil-moisture sensors (SMT-100, Truebner) with a measurement accuracy of 1% when calibrating soil-specific [Truebner, 2017]. The recorded absolute water content can be converted to a volumetric relative gas saturation Θ_{rg} which is calculated by using Θ_{fs} as fully saturated water content and Θ_{mw} as measured water content:

$$\Theta_{rg} = \frac{\Theta_{fs} - \Theta_{mw}}{\Theta_{fs}} \tag{4.1}$$

5

Results

5.1 Methane injection

The methane injection experiment has been realized in the southern central part
of the test field (Figure 3.9). The subsurface is characterized by fine sand with
intermittent silty layers and a low permeable clay layer at 9 m depth. Between
the 14th and 15th of May 2019 50 l/min (35 kg) of gaseous $CH4$ was injected at
a depth of 17.5 m. The corresponding baseline and monitoring measurements
timeline are displayed in Table 4.2. Figure 5.1 shows the quality checked signal.
The necessary data repeatability is illustrated in Figure 5.2b. In 70 % of the
measurements the deviation between first and second measurement amounts to
<10 %.

Travel time and P-wave velocity

The evaluation in regards of a borehole deviation is shown in Figure 5.3 A.
We compare the trend of the recorded P-wave velocity. $RB1$ and $RB2$ are
situated at a small distance from each other compared to the position of the
source borehole. The P-wave velocity does not deviate much between $RB1$ and
$RB2$ during the baseline measurement thus we assume that a possible borehole
deviation is negligible. In Figure 5.3 B - D the differences in travel time are
illustrated for the first three monitoring cycles. The travel time differences are
calculated by subtracting, the travel time of the monitoring cycles from the
baseline. A negative dt indicates a decrease in P-wave travel time compared to
the baseline measurement. A positive dt indicates the opposite. We see a clear
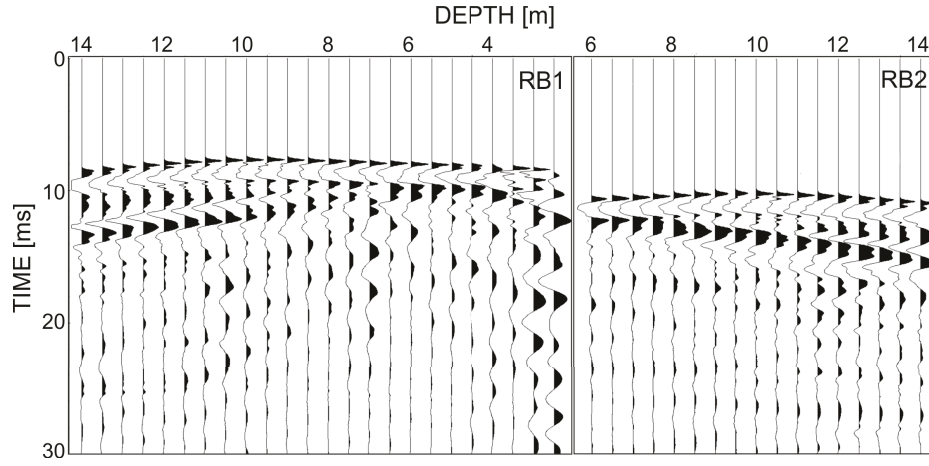
Figure 5.1: Signal of baseline measurement at the methane test site in 8 m depth.

change in travel time 5 - 18 days after injection below 10 m depth. In Figure 5.3 D the travel time difference becomes negligible. We observe travel time changes in both receiver wells and thus assume the whole area between $RB1$ and $RB2$ being affected by gas-induced parameter changes. The following observations of P-wave velocities are therefore focused only on the area between $RB1$ and $RB2$ based on Figure 4.2. Changes in P-wave velocity are clearly visible (Figure 5.4). We assume gas-induced changes in the subsurface mainly occur in the deeper areas.

Water-content measurements

Soil-moisture sensors have monitored the methane injection process. Figure 3.9 illustrates the location of the water content measurement wells. These data can be used to assess the ability of seismic waves to detect or to even quantify gas content in the subsurface. In Figure 5.5 A at the left-hand side, the water content is plotted against the seismic velocity. We can see an almost linear dependency between both parameters. The measured results at all four locations are illustrated on the right side. The event of the gas injection is visible at the data drop. From soil moisture data the relative gas content can be inferred. This gas content has been compared to a calculated gas content inferred from P-wave velocity (Figure 5.5 B). The principle is demonstrated in Section 2.3.1, Equation 2.6. For our calculations, we apply the time-average relationship [Wyllie et al., 1956] at 11 m and 12 m depth. Figure 5.5 C shows the coherency between the measured soil moisture content and the measured P-wave velocity. In table 5.1 we find the results of the calculated gas content derived from P-wave velocities based on [Wyllie et al., 1956]. The calculation of the gas content following [Mavko et al., 1995] and [Bachrach and Nur, 1998]
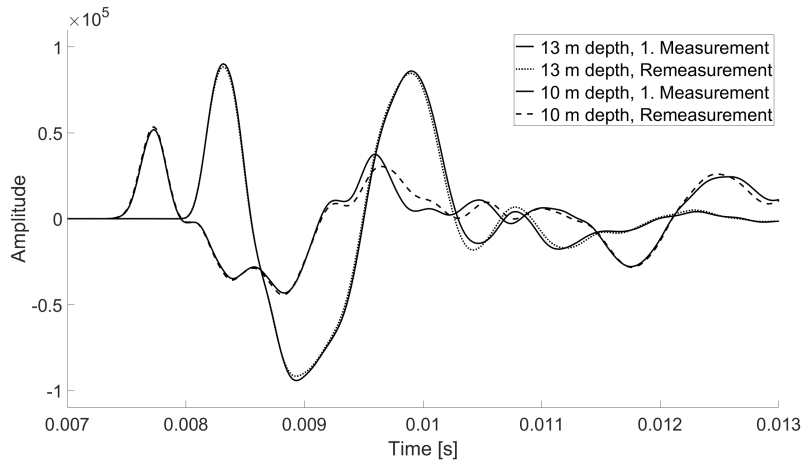
(a) *RB1*
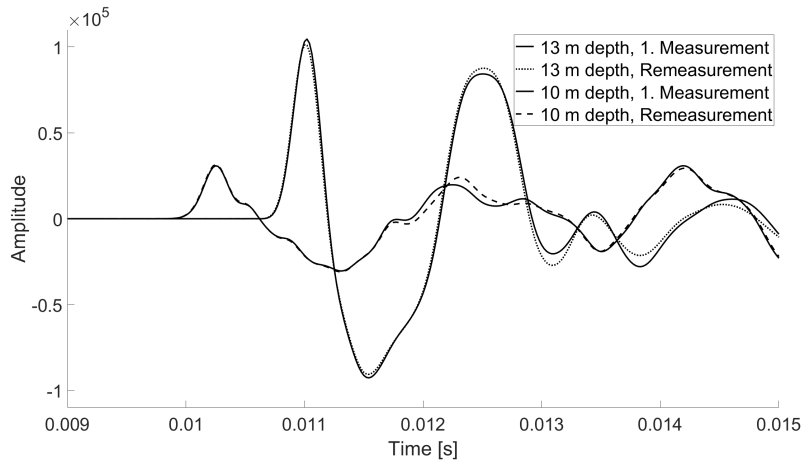
(b) *RB2*

Figure 5.2: Repeated baseline measurements at 10 and 13 m depth. After the first measurement cycle (straight line) the hydrophone strings and seismic source has been recovered and laid out again for a second measurement (dotted, dashed), [Birnstengel et al., 2024].
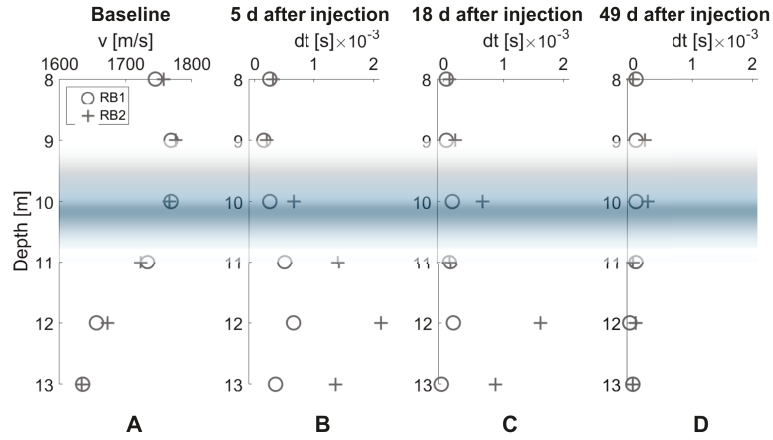
Figure 5.3: (A) P- wave velocity, (B-D) traveltime differences between baseline and monitoring cycles (dt) at different time steps. The blue stripes sketch the hydraulic low permeable layer between 9 - 11 m depth, [Birnstengel et al., 2024].
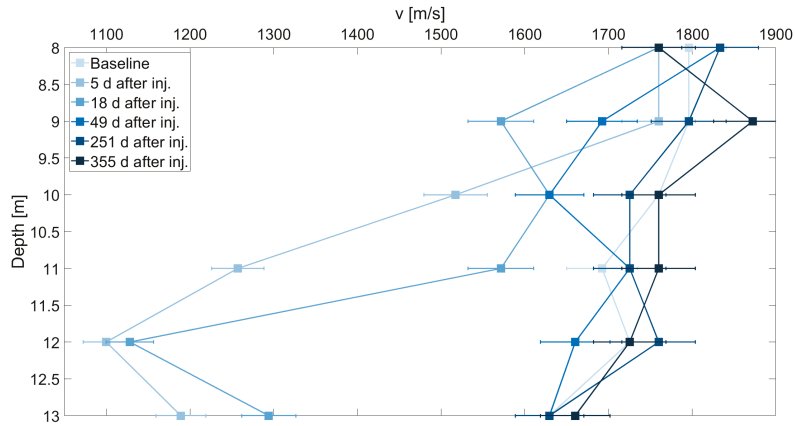
Figure 5.4: P-wave velocity between $RB1$ and $RB2$ during methane injection, [Birnstengel et al., 2024].

has been performed using the parameters in table 5.2.

Table 5.1: Gas content Θ_g in [Vol.%] after [Wyllie et al., 1956] for each depth calculated for four time steps after injection according to equation 2.6 [Birnstengel et al., 2024].

Depth [m]	5 d after inj.	18 d after inj.	49 d after inj.	251 d after inj.
13	4.7	3	0	0
12	7.3	5.6	0.2	-0.4
11	4.9	0	0	-0.4
10	2.3	2.3	0.9	0.2
9	0.7	0.7	0.7	0
8	1	0.4	0	0

Table 5.2: Parameters for calculating P-wave velocity depending on water saturation according to [Mavko et al., 1995, Bachrach and Nur, 1998], [Birnstengel et al., 2024].

Parameter	Symbol	Value	Unit
Bulk density	ρ	1500 - 1800	kg x m^{-3}
Density Water	ρ_f	999	kg x m^{-3}
Density Methan	ρ_g	0.717	kg x m^{-3}
P-wave velocity water	V_{pf}	1480	m x s^{-1}
P-wave velocity methane	V_{pg}	430	m x s^{-1}

Table 5.3: Gas content Θ_g in [Vol.%] for each depth calculated for four time steps after injection following [Bachrach and Nur, 1998].

Depth [m]	5 d after inj.	18 d after inj.	49 d after inj.	251 d after inj.
13	55	33	-	-
12	90	67	2	-4
11	60	-	-	-4
10	27	27	1	-2
9	8	8	8	-
8	12	4	-	-

Amplitude, energy and quality factor

In order to understand the impact of the injected gas on the seismic amplitude, firstly, the amplitude level is evaluated in every monitoring cycle. The amplitude level in $RB1$ at the top and $RB2$ at the bottom is shown in Figure 5.6. After the gas injection, an instant amplitude drop is visible in both receiver boreholes. That figure shows very prominent the increase of the amplitude over time. After one year of observation, the amplitude level of the baseline measurement has not yet been reached. The amplitude changes have been evaluated in percentage
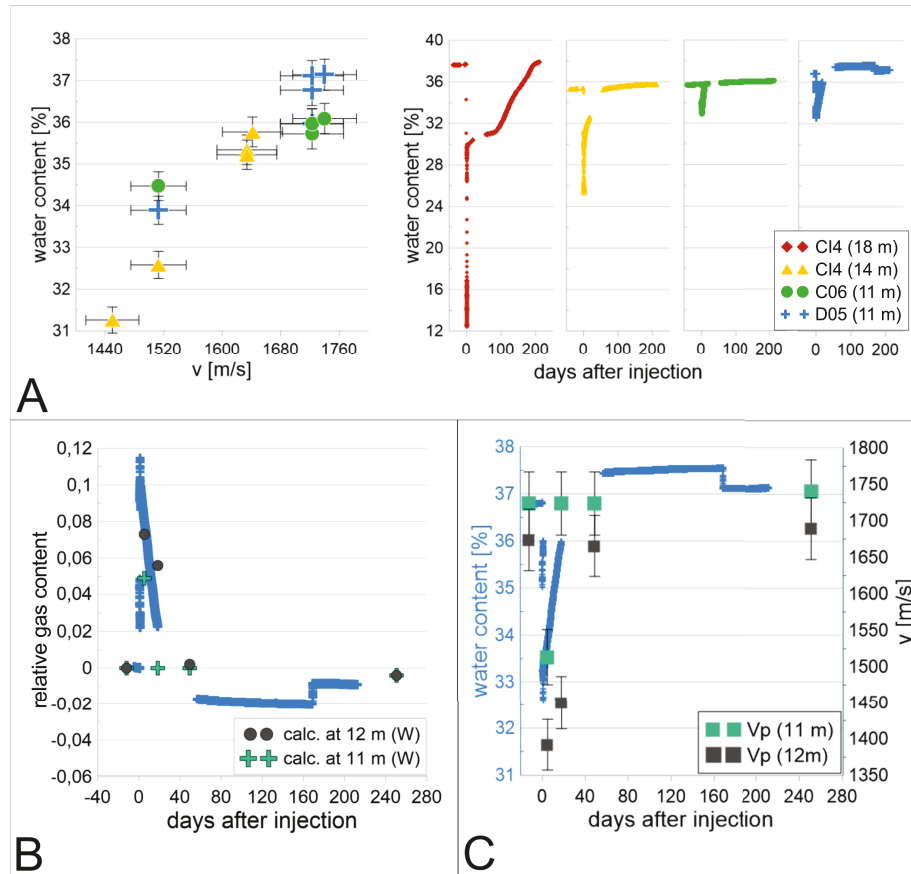
Figure 5.5: (A) P-wave velocity between SB and $RB2$ in dependence of water content, measured in well DO5, C06 and CI4 during the injection process. Porosities of D05 = 36.5 %, C06 = 35.5 %, CI4 = 35.1 %. Soil water measurements at the midth injection well CI4 at 14 and 18 m, and at D05 and C06 at 11 m depth. (B) Gas content at D05 at a sensor in 11 m and 12 m depth plotted with the calculated gas content after [Wyllie et al., 1956]. (C) Water content at D05 at a sensor in 11 m depth plotted with the P-wave velocity in 11 m and 12 m depth. Injection timing is indicated by the dashed line [Birnstengel et al., 2024].

based on the baseline measurement for both receiver boreholes (Figure 5.7A, B). The blue line indicates the baseline measurement, which corresponds to the reference to 100%.

Looking at the whole energy level of the signal at different monitoring cycles (Figure 5.8), we see a drop in the energy level directly after the injection in both receiver wells. Zooming in shows a more differential energy loss. Be aware, that the energy level in $RB1$ is shown with 10^8, whereas $RB2$ is plotted with 10^7. The impact on the seismic amplitude can be further assessed with the quality factor, where each dissipation has been recorded between $RB1$ and $RB2$. Figure 5.9 shows the quality factor inferred from the energy at $RB2$ for the baseline measurement at each depth divided by the energy dissipation at each monitoring cycle at $RB2$ and therefore giving an impression over time [Birnstengel et al., 2024]. The instant change is visible, as is the tendency of approaching the baseline level in the last monitoring cycle.
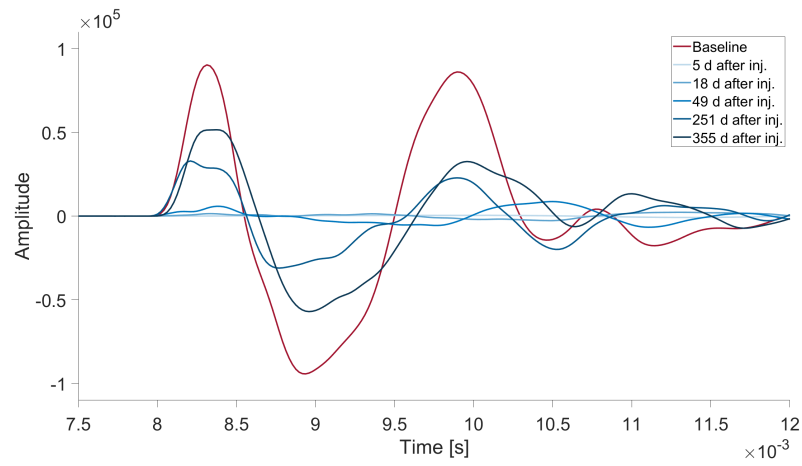
(a) *RB1*
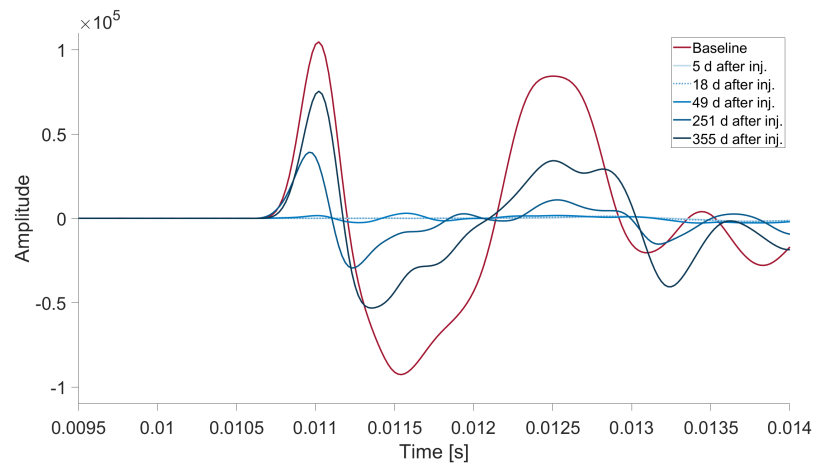
(b) *RB2*

Figure 5.6: Time series of the methane injection monitoring at a depth of 13 m with the focus on amplitude deviation.
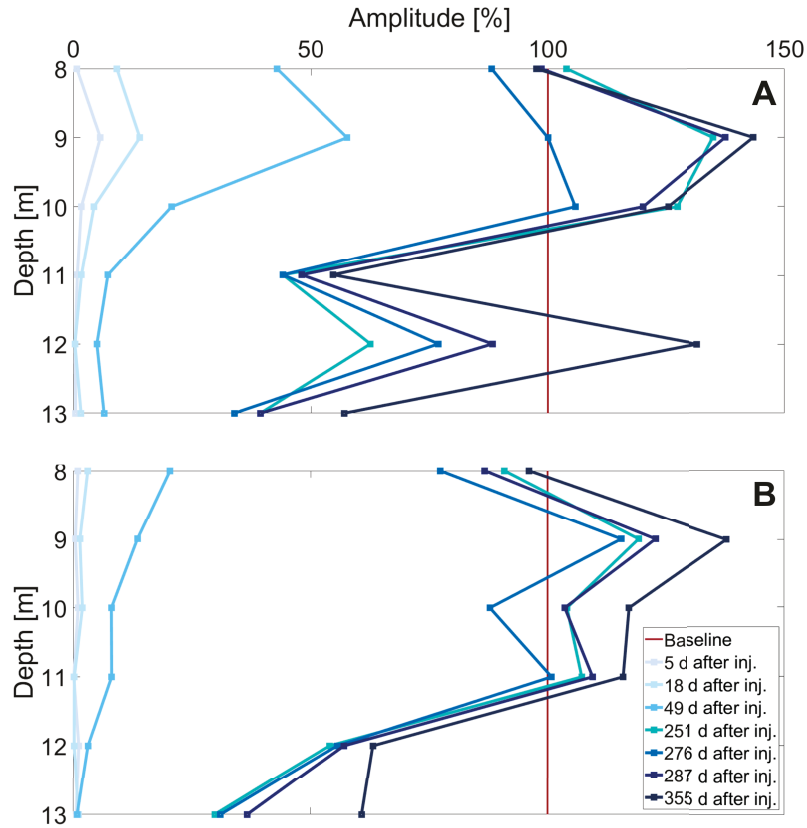
Figure 5.7: Percentage amplitude change relative to the baseline measurement (marked by 100 %) indicates the first break amplitude. (A) displays the amplitude deviation in $RB1$ and (B) in $RB2$ in respect of the baseline measurement [Birnstengel et al., 2024].
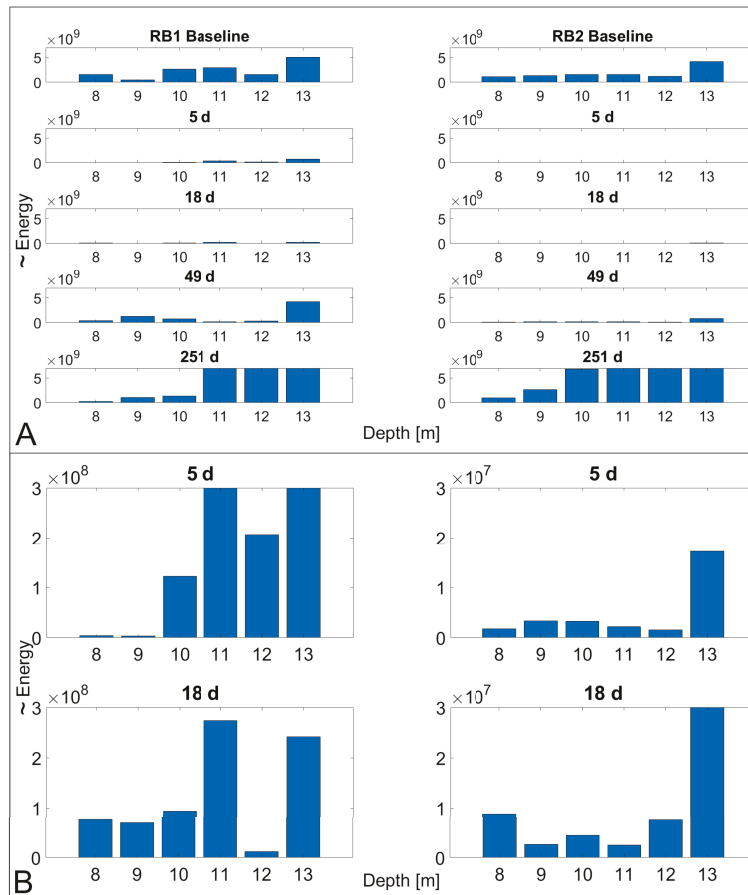
Figure 5.8: (A) Energy level of the cross hole measurements at different monitoring cycles with a (B) zooming window for the first two monitoring cycles.
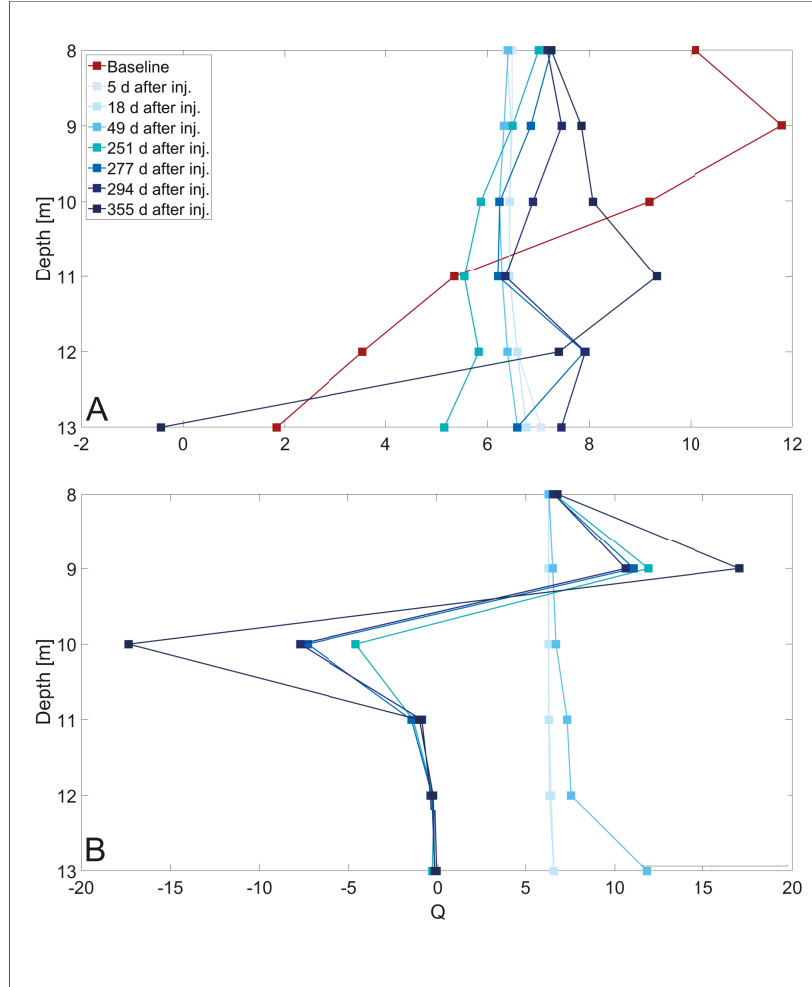
Figure 5.9: The quality factor with depth obtained with (A) The quality factor inferred from the energy at $RB1$ at each baseline and monitoring cycle individually divided by the energy dissipation along the travel path energy $\Delta E = E_{RB1} - E_{RB1}$. (B) The quality factor inferred from the energy at $RB2$ for the baseline measurement at each depth divided by the energy dissipation at each monitoring cycle with $\Delta E = E_{Baseline} - E_{Monitoring}$ at $RB2$ [Birnstengel et al., 2024]
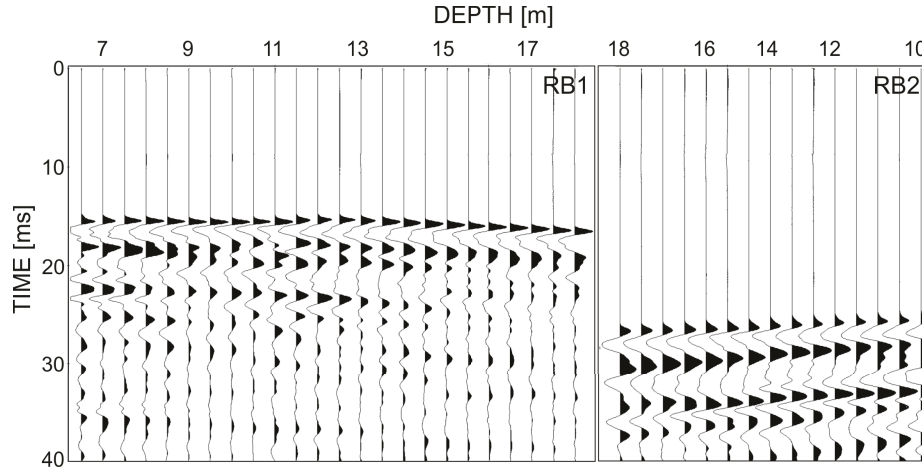
Figure 5.10: Signal of baseline measurement at the hydrogen test site in 8 m depth.

5.2 Hydrogen injection

The injection of gaseous hydrogen took place in the northwestern part of the test site (Figure 3.10). The area is characterized by clayey fine-grained sand intermittent by clay and silty clay layers at groundwater level and 8 - 10 m depth. The injection comprised three days (28th - 30th of January) of inducing 40 NL/min at a depth of 18 m, which in the end summed up to a mass of 12 kg gaseous hydrogen. The signal at a shooting depth of 8 m is shown in Figure 5.10. The repeatability of the data is illustrated in (Figure 5.11).

Travel time and P-wave velocity

Figure 5.12 A shows the P-wave velocities for the baseline measurement. The trend of P-wave velocity recorded in both receiver wells does not deviate much; thus, a possible borehole deviation can be neglected for our investigations. The travel time differences in Figure 5.12 B - D show a deviation between the monitoring 4 35 days after H2-injection compared to the baseline measurement in the depth between 11 16 m. Later, 96 days after injection, the travel time differences match the baseline. Since we can observe an impact of gas-induced changes on the P-wave travel time in both receivers, we infer that the area between $RB1$ and $RB2$ is affected. We focus our investigations between $RB1$ and $RB2$ and illustrate the P-wave velocity for the baseline and five monitoring measurements in Figure 5.13. The first three monitoring measurements show slower velocities compared to the baseline (red). After 96 days the P-wave velocity approaches the baseline level. With clearly visible changes in the P-wave velocity (Figure 5.13) we assume gas induced changes in the subsurface.
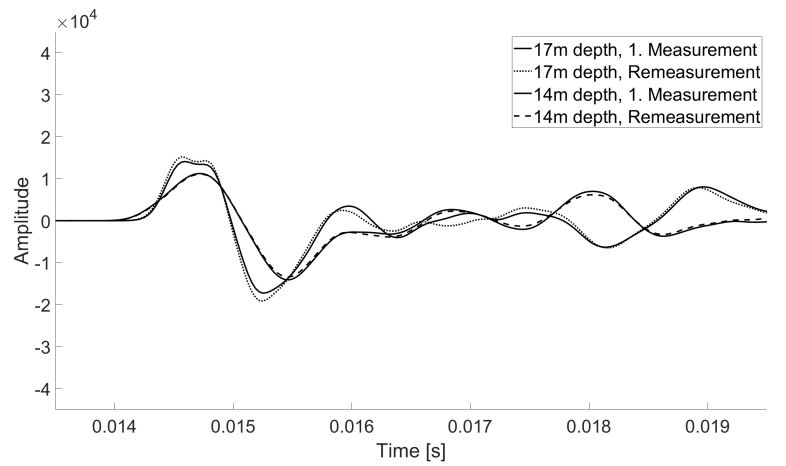
(a) *RB1*
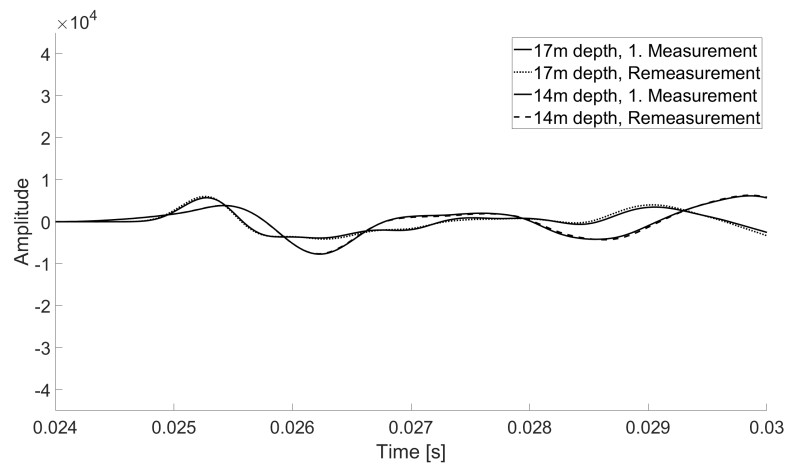
(b) *RB2*

Figure 5.11: Repeated baseline measurements at 14 and 17 m depth. After the first measurement cycle (straight line) the hydrophone strings and seismic source has been recovered and laid out again for a second measurement (dotted, dashed).
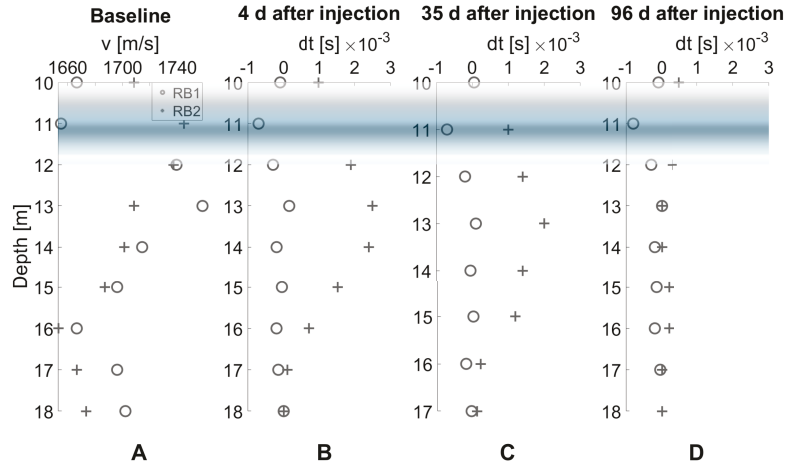
Figure 5.12: (A) P- wave velocity, (B-D) travel time differences between baseline and monitoring cycles (dt) at different time steps. The blue striped sketch the hydraulic low permeable layer between 10 - 12 m depth.
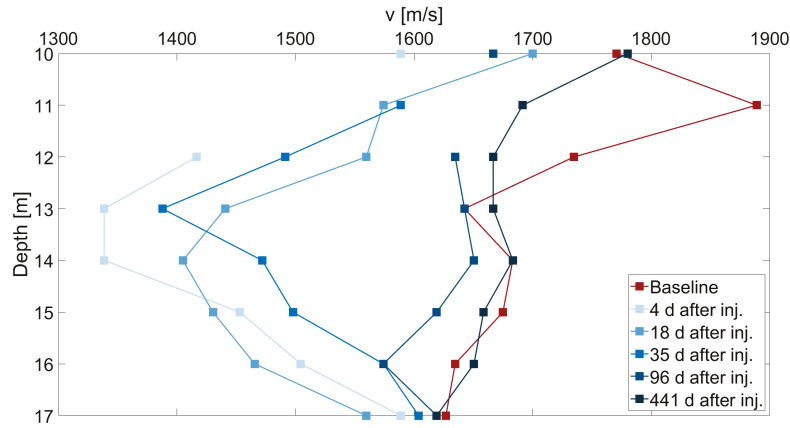
Figure 5.13: P-wave velocity between $RB1$ and $RB2$ for the hydrogen injection. There is no value at four days after the injection at 11 m depth.

Water content measurement

The hydrogen injection process has been monitored by soil-moisture sensors. In Figure 5.14 A, on the left-hand side, the water content is plotted against the seismic velocity. Alike the methane experiment, we can see an almost linear regression between both parameters. The water content measurement at three wells is illustrated on the right side. The gas injection is clearly visible at the data drop. From soil moisture data, the relative gas content can be inferred. This gas content has been compared to a calculated gas content inferred from P-wave velocity (Figure 5.14 B) analogous to the methane injection experiment. The calculation after Wyllie (W) based on the time average relation and the calculation after Mavko (M) [Wyllie et al., 1956], [Mavko et al., 1995] are applied for the parameters in 14 m depth. Figure 5.14 C shows the coherency between the measured soil moisture content and the measured P-wave velocity.

Table 5.4: Gas content Θ_g in [Vol.%] for each depth calculated for four time steps after injection according to equation 2.6

Depth [m]	4 d after inj.	18 d after inj.	35 d after inj.	96 d after inj.	441 d after inj.
18	0	-	-	0	1.1
17	2.3	2.3	2.3	0	0
16	16.7	4.6	4.6	4.6	-6.9
15	34.6	34.6	27.7	4.6	0
14	55.4	43.89	32.34	0	-2.3
13	57.7	46.2	46.2	0	-2.3
12	43.8	43.8	32.34	6.9	2.3
11	-	23.1	23.1	-	6.9
10	23.1	11.5	-	11.5	-2.3

The calculation of the gas content following [Mavko et al., 1995] and [Bachrach and Nur, 1998] has been performed using the following parameters:

Table 5.5: Parameters for calculating P-wave velocity depending on water saturation according to [Mavko et al., 1995, Bachrach and Nur, 1998].

Parameter	Symbol	Value	Unit
Bulk density	ρ	1500 - 1800	kg x m^{-}3
Density Water	ρ_f	999	kg x m^{-}3
Density hydrogen	ρ_g	0.0899	kg x m^{-}3
P-wave velocity water	v_{pf}	1480	m x s^{-}1
P-wave velocity hydrogen	v_{pg}	1280	m x s^{-}1

Amplitude, energy and quality factor

We also want to see the effect of gas-induced changes on the signal's amplitude. Figure 5.15 illustrates the change in amplitude level in $RB1$ (a) and $RB2$ (b). In $RB1$, the amplitude level is rising after injection, whereas $RB2$ shows a drop
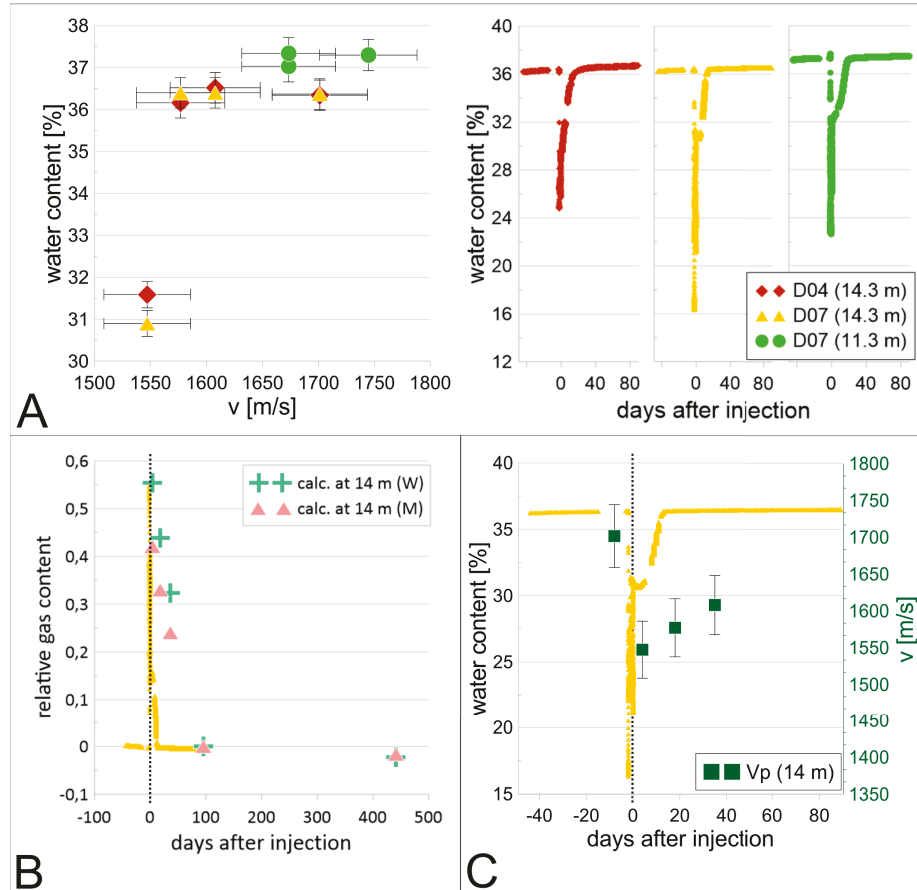
Figure 5.14: (A) P-wave velocity between SB and $RB2$ in dependence of water content, measured in well D04 and D07 during the injection process. Soil water measurements took place at D07 at 11.3 and 14.3 m depth, and at D04 at 11.3 m depth. Porosities of D04 (14.3 m) = 36.18 and in D07 (11.3 m) = 37.17. (B) Gas content at D07 at a sensor in 14.3 m depth plotted with the calculated gas content after [Wyllie et al., 1956] (W) and [Mavko et al., 1995] (M). (C) Water content at D07 at a sensor in 14.3 m depth plotted with the P-wave velocity in 14 m depth. Injection timing is indicated by the dashed line.

Table 5.6: Gas content Θ_g in [Vol.%] for each depth calculated for four time steps after injection following [Bachrach and Nur, 1998].

Depth [m]	4 d after inj.	18 d after inj.	35 d after inj.	96 d after inj.	441 d after inj.
18	0	-	-	0	0.8
17	1.6	1.6	1.6	0	0
16	11.69	3.3	3.3	3.3	-4.9
15	25.9	25.9	20.6	3.3	0
14	42.6	33.4	24.4	0	-1.6
13	44.7	35.4	35.4	0	-1.7
12	34.2	34.2	24.9	5.2	1.7
11	-	17.7	17.7	-	5.2
10	17.3	8.6	-	8.6	-1.7

in the amplitude level. The percentage variation in Figure 5.16 shows an increase in the amplitude in $RB1$, that is small 4 days after injection and increases over time. It shows a decline of the amplitude in $RB2$ with levels exceeding the baseline 441 days after injection.

Furthermore, we investigated the energy level of the signal (Figure 5.17). The energy level in $RB2$ is generally lower (10^7) than in $RB1$ (10^9). In order to obtain the energy level, the amplitude of the signal has been squared. We can see an increase of the energy level in $RB1$ and a decrease in $RB2$. During the monitoring cycles, it happened that the borehole have silted up which prevented us from measuring in 18 m depth. After ensilting the wells, we were again able to go back to 18 m depth. The data of the monitoring 441 days after injection have been spared out since they did not differ very much from the monitoring 96 days after injection.

Another expressive factor is the quality factor inferred from subtracted energy levels (see Chapter 4). Figure 5.18 shows the quality factor at different monitoring cycles. After the injection, we can see a smaller quality factor that goes back to baseline level after 441 days.
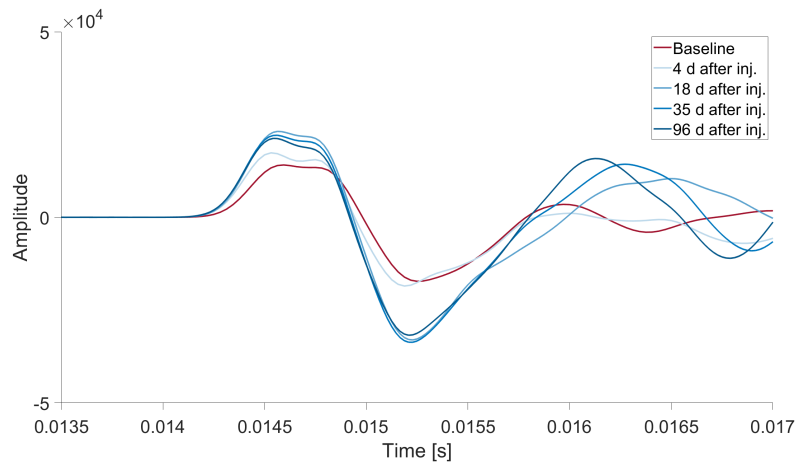
(a) *RB1*
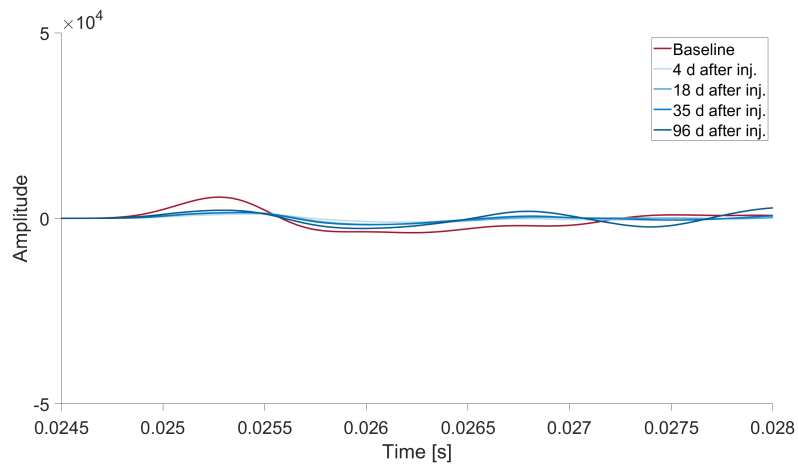
(b) *RB2*

Figure 5.15: Time series of the H2 injection monitoring at a depth of 17 m with the focus on amplitude deviation.
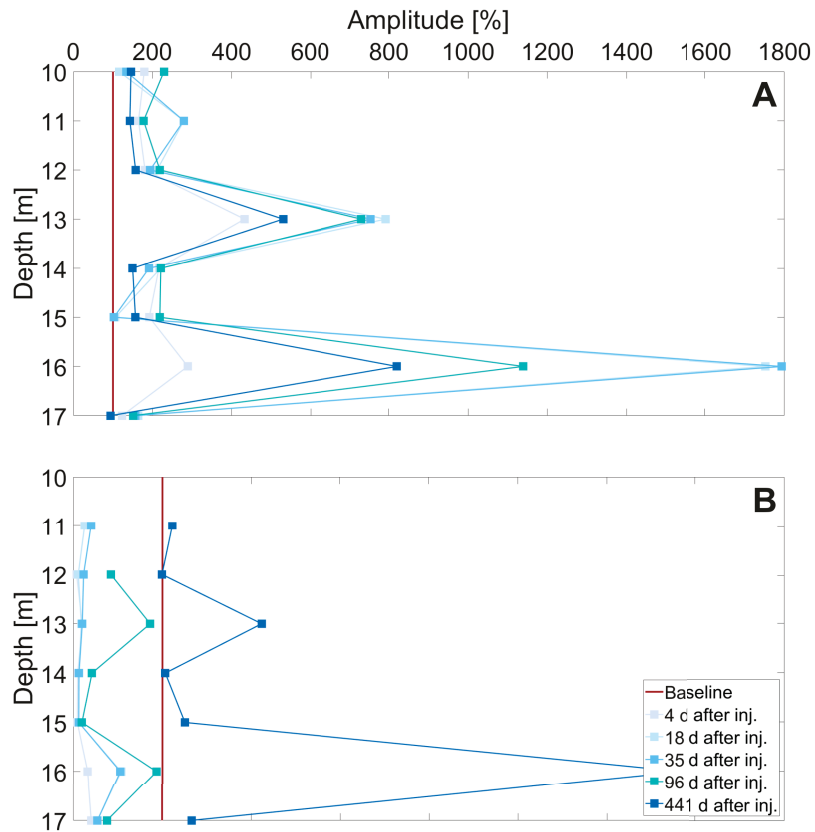
Figure 5.16: Percentage amplitude change relative to the baseline measurement for the hydrogen injection marked by 100% and indicates the first break amplitude . (A) displays the amplitude deviation in $RB1$ and (B) in $RB2$ in respect of the baseline measurement [Birnstengel et al., 2024].
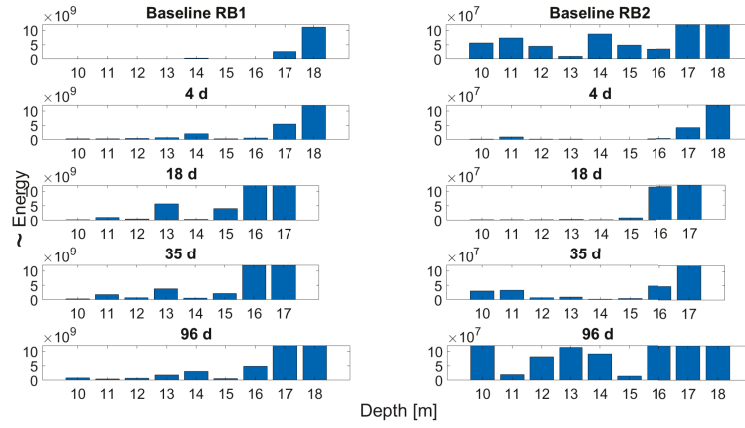
Figure 5.17: (A) Energy levels of the cross hole measurements at different monitoring cycles during hydrogen injection.
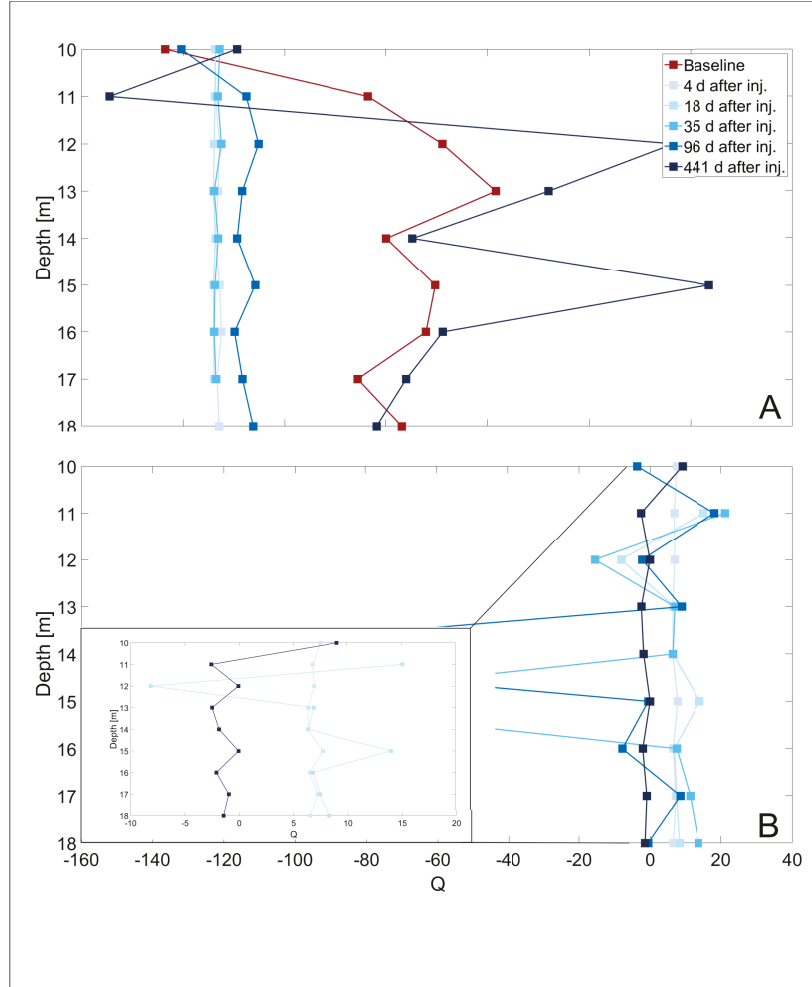
Figure 5.18: The quality factor of the hydrogen injection with depth obtained using (A): The quality factor inferred from the energy at $RB1$ at each baseline and monitoring cycle individually divided by the energy dissipation along the travel path energy $\Delta E = E_{RB1} - E_{RB12}$. (B): The quality factor inferred from the energy at $RB2$ for the baseline measurement at each depth divided by the energy dissipation at each monitoring cycle with $\Delta E = E_{Baseline} - E_{Monitoring}$ at $RB2$ [Birnstengel et al., 2024].

Figure 5.19: Seismogram of the baseline shot at 8 m depth used for travel time picking. In RB1 24 traces got recorded, in RB2 17 traces recorded the P-wave signal for 30 ms. Signal peaks after the initial peak occur as the P-wave gets reflected at the water table, the subsurface and sedimentary boundary layers

5.3 Heat injection

The heat injection experiment took place northeast of the test site, as shown in Figure 3.11. The subsurface is characterized by medium to coarse-grained clayey sand intermittent by silty clay layers between 2 m - 6 m depth. The infiltration of high-tempered water lasted from the 23rd of May to the 28th of May in 2019. 14.5 l of water per minute have been injected between 7 - 14 m depth. That sums up to a volume of 86 l. The timeline of corresponding baseline and monitoring measurements are displayed in Table 4.2. The signal (Figure 5.19), its stability in quality and the repeatability of measurements have been analyzed over the whole monitoring period. They are displayed in Figure 5.20.

Travel time and P-wave velocity

As for the gas injection experiments, a possible borehole deviation can be neglected during our investigations since the trend of the recorded P-wave velocity does not deviate much in both receiver wells. The travel time differences (dt) between the baseline and each monitoring measurement are displayed in Figure 5.21 B - D for three time steps in order to capture heat-induced changes on the seismic signal. Figure 5.21 B shows a decreasing travel time in $RB2$ in 8 - 13 m depth and an increased travel time at 11 m depth in $RB1$ up to 7 days after the injection. Four weeks later, the travel time difference for $RB1$ is almost 0, whereas the travel time difference in $RB2$ between 8 - 11 m depth remains visible (Figure 5.21 C). It becomes negligible 266 days after injection (Figure 5.21

(a) *RB*1

(b) *RB*2

Figure 5.20: Repeated baseline measurements at 9 and 15 m depth. After the first measurement cycle (straight line) the hydrophone strings and seismic source has been recovered and laid out again for a second measurement (dotted, dashed).

Figure 5.21: (A) P- wave velocity, (B - D) travel time differences between base-line and monitoring cycles (dt) at different time steps. The blue stripe sketches the hydraulic low permeable layer between 14 - 16 m depth.

D) for both receiver wells. Due to the indication of a change in travel time (Figure 5.21 B-D) in both receiver wells, we assume the whole area between $RB1$ and $RB2$ being influenced by heat-induced changes. Hence the analyses are focused on the area between $RB1$ and $RB2$, where P-wave velocities are derived from the travel time differences between $RB1$ and $RB2$, referring to (Figure 4.2. The P-wave in Figure 5.22 shows velocity deviations from baseline level during the first two monitoring cycles (7 - 36 days after injection), mainly between 8 - 12 m depth. Follow-up observations 344 days after injection indicate smaller to no changes when the seismic P-wave velocity approaches baseline level.

Amplitude, energy and quality factor

In order to investigate the impact of temperature changes on the seismic amplitude, the observation of amplitudes is displayed in Figure 5.23 exemplary at 8 m depth. In $RB1$ (a), a drop in seismic amplitude occurs compared to the baseline measurement (red) 7 days after injection. The baseline level is reached 36 days after injection, and the monitoring cycles afterwards show higher amplitudes than the baseline. The overall amplitude level in $RB2$ is already smaller than in $RB1$ due to the longer travel path. The most substantial amplitude drop occurs seven days after injection. The monitoring cycles afterwards show a constantly increasing amplitude. Thereupon the cross-hole energy calculated by squaring the signal's amplitude is plotted in Figure 5.24. We see a higher energy level at $RB1$ than at $RB2$. Zooming into the first three measurements shows the impact on $RB2$. The observation 36 days after injection shows a
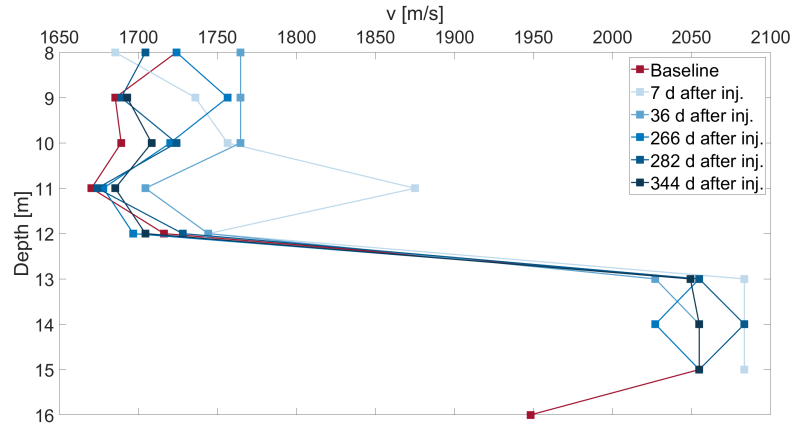
Figure 5.22: P-wave velocity between $RB1$ and $RB2$ inferred from travel time differences between $RB1$ and $RB2$.

weaker signal on both receiver wells, which is attributed to a lower source signal. The observations after 266 and 687 days have been excluded since they do not differ significantly from previous or following observations. Subsequently, the obtained quality factor is illustrated with depth and shows irregular variations throughout all depths and monitoring cycles.
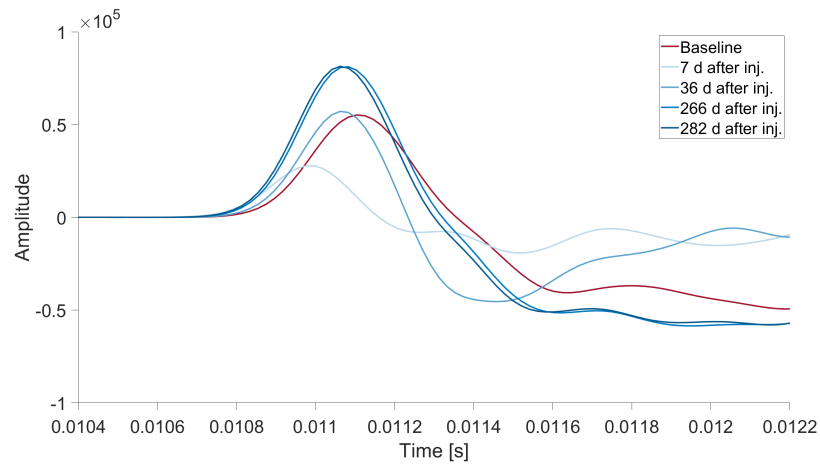
(a) *RB1*
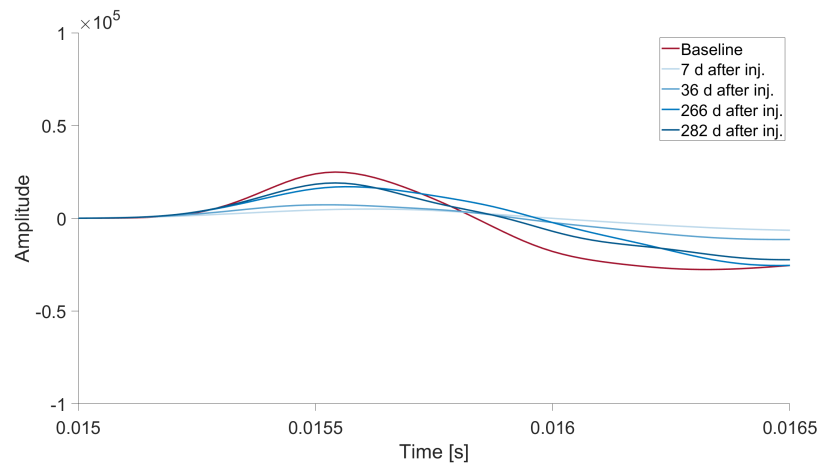
(b) *RB2*

Figure 5.23: Time series of the heat injection monitoring at a depth of 8 m with the focus on amplitude deviation.

Figure 5.24: (A) Energy levels of the cross hole measurements at different monitoring cycles with a (B) zooming window for the first two monitoring cycles.
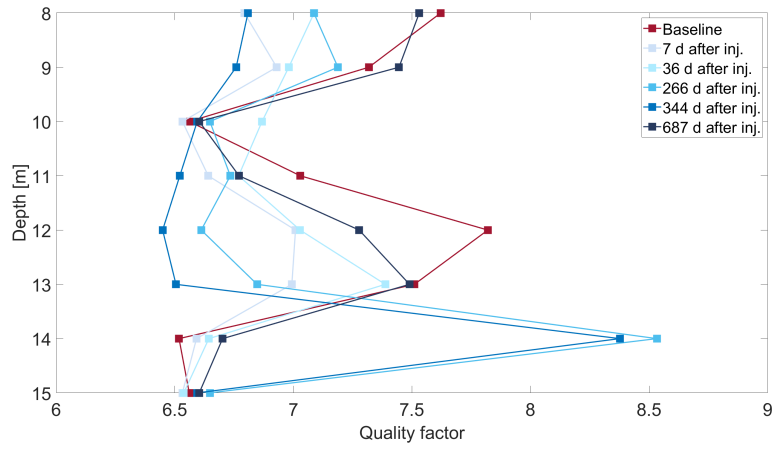
Figure 5.25: The quality factor is inferred from the energy at $RB1$ at each baseline and monitoring cycle. It has been individually divided by the energy dissipation along the travel path energy: $\Delta E = E_{RB1} - E_{RB2}$
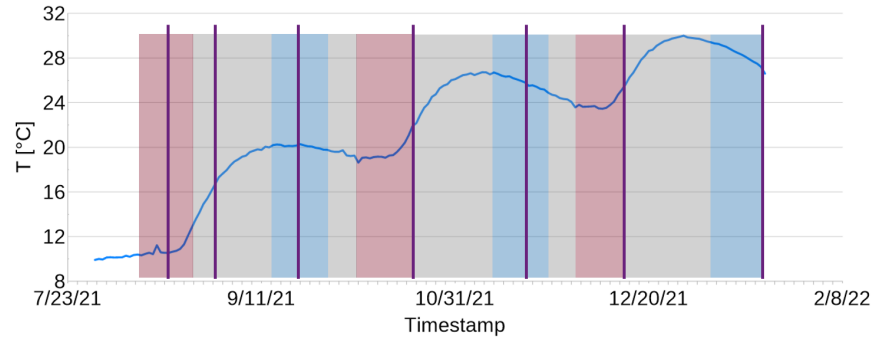
(a) Phase 1
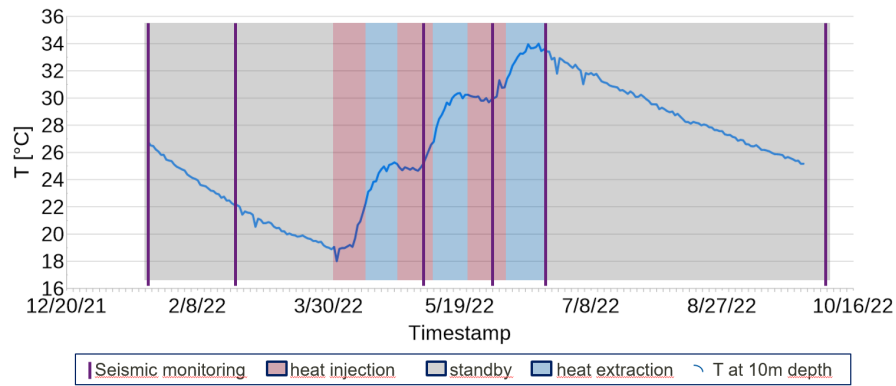
(b) Phase 2

Figure 5.26: Timeline of the second heat injection experiment. The temperature information originates from $RB2$ at $10\,\text{m}$ depth. a) heat injection, standby and extraction periods follow up on each other, b) heat injection and extraction follow up on each other without standby periods in between.

5.4 Heat injection 2

The second heat injection experiment is an extension of the first one with similar injection parameters. The timeline of two phases are displayed in Figure 5.26. The seismic monitoring covers different phases of the experiment. The signal (Figure 5.27), its stability in quality and the repeatability of the experiment has been analyzed over the whole monitoring period displayed in Figure 5.28 with a considered error margin of 3%.
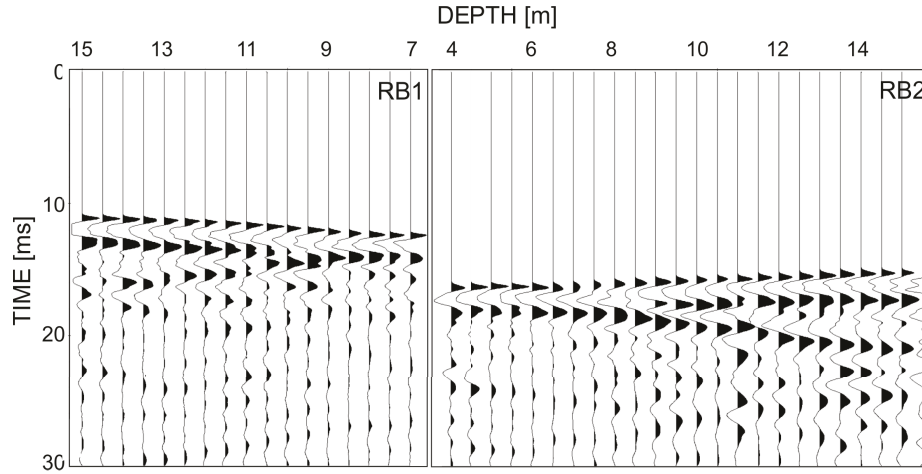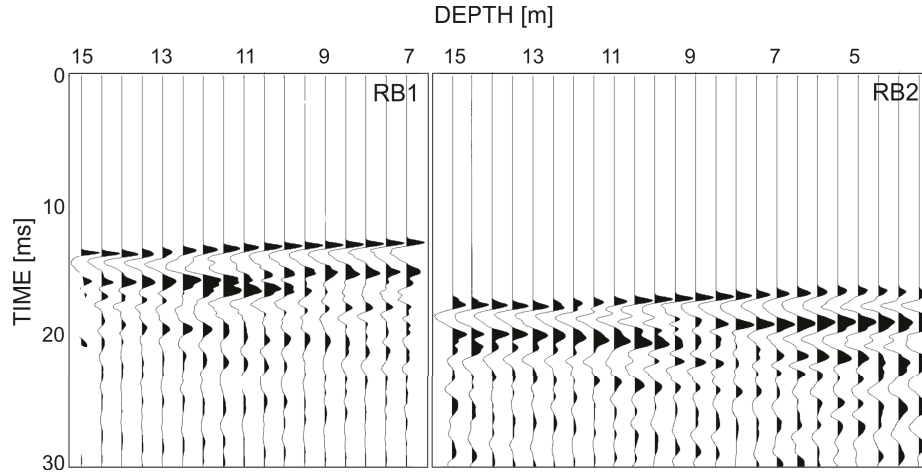
Figure 5.27: Seismogram of the baseline shot at 8 m depth used for travel time picking. In RB1 17 traces got recorded, in RB2 24 traces recorded the P-wave signal for 30 ms. Signal peaks after the initial peak occur as the P-wave gets reflected at the water table, the subsurface and sedimentary boundary layers

Travel time and P-wave velocity

In addition to the already existing boreholes, new ones have been installed perpendicular to the former heat injection test site. A possible borehole deviation on our measurements need to be reconsidered, and the baseline P-wave velocities have been analyzed at $RB1$ and $RB2$ (Figure 5.29 A). The trend of P-wave velocity recorded in both receiver wells does not deviate much; thus a possible borehole deviation can be neglected for our investigations. The travel time differences between the baseline and each monitoring measurement are displayed in Figure 5.29 B - D for three time steps to capture heat-induced changes on the seismic signal. Since the experiment focuses on cyclic temperature changes, the different time steps cover the heat injection, standby and heat extraction period. Figure 5.29 B shows a decreasing travel time in $RB2$ and in $RB1$ during the 2-week injection period between 8 - 12 m depths and a slight increase of the travel time between 12 - 14 m depth. The first standby period lasts for three weeks. The travel time difference in $RB1$ is decreasing. During the extraction period in Figure 5.29 D, which takes place one month after B, the travel time difference in $RB1$ is increasing again. Both receiver wells indicate a change in travel time (Figure 5.29 B-D); thus we assume the whole area between $RB1$ and $RB2$ being influenced by heat-induced changes. Analogue to the other experiments, we focus our analyses on the area between $RB1$ and $RB2$ and derive P-wave velocities from the travel time differences between $RB1$ and $RB2$ referring to Figure 4.2. Figure 5.32 shows the temperature at $RB2$ in 10 m depth. The colored marker in that plot corresponds to the colors of the P-wave velocity plot in Figure 5.30 and Figure 5.31.
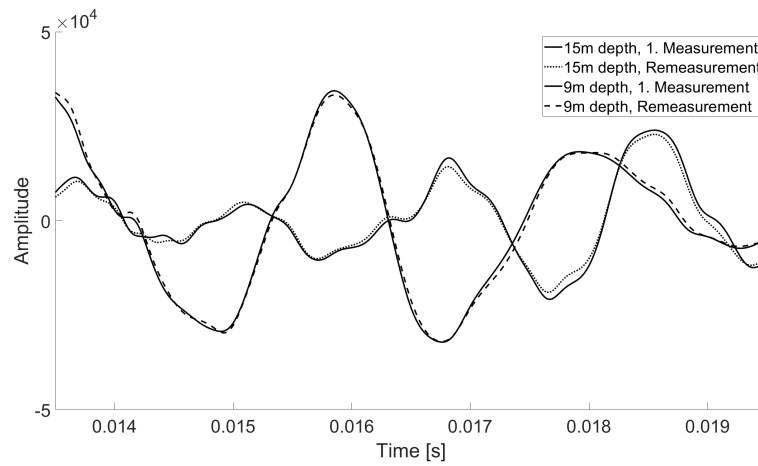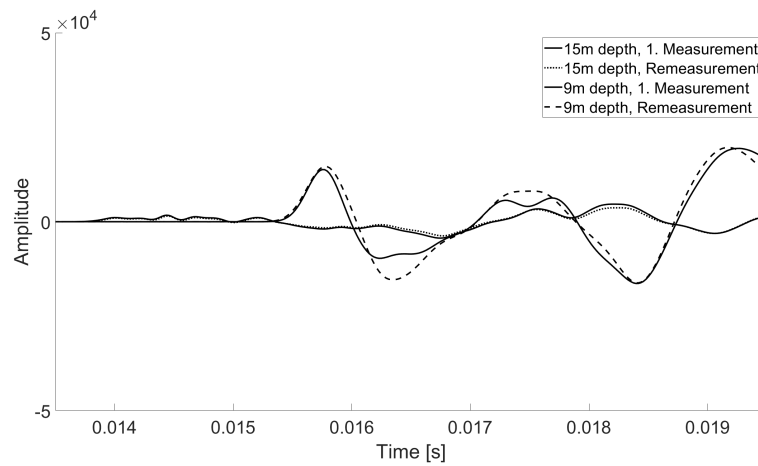
81
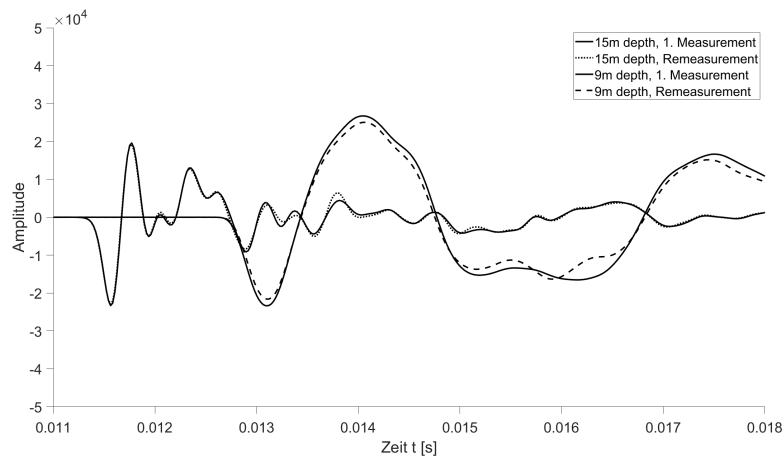
(a) *RB1*
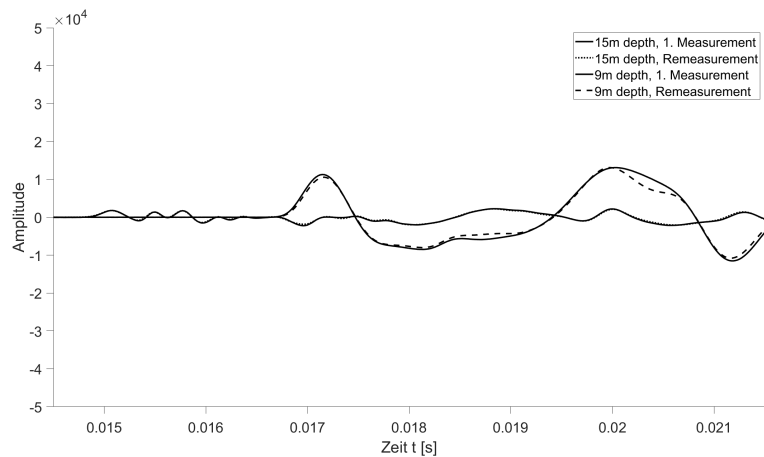
(b) *RB2*

Figure 5.28: Repeated baseline measurements at 9 and 15 m depth.   After the first measurement cycle (straight line) the hydrophone strings and seismic source has been recovered and laid out again for a second measurement (dotted, dashed).
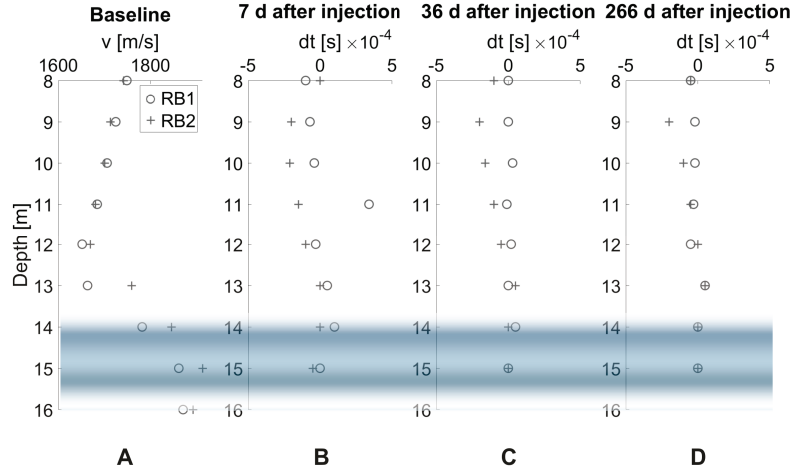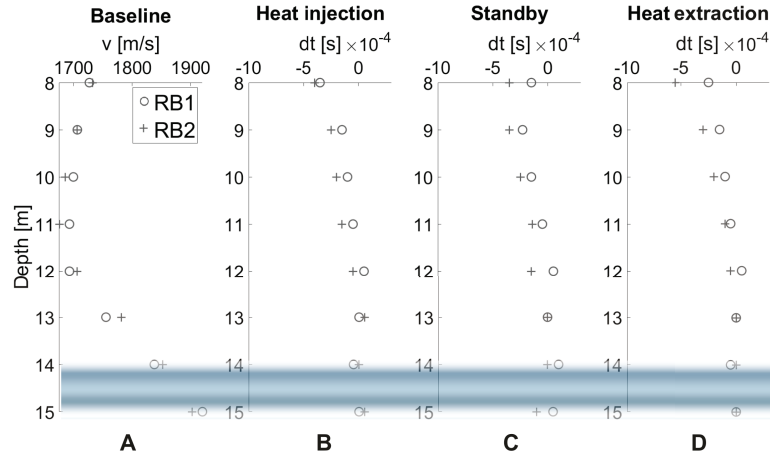
Figure 5.29: (A) P- wave velocity, (B - D) travel time differences between baseline and monitoring cycles (dt) at different time steps for the second heat injection experiment in phase 1. The blue stripe sketches the hydraulic low permeable layer between 14 - 16 m depth.
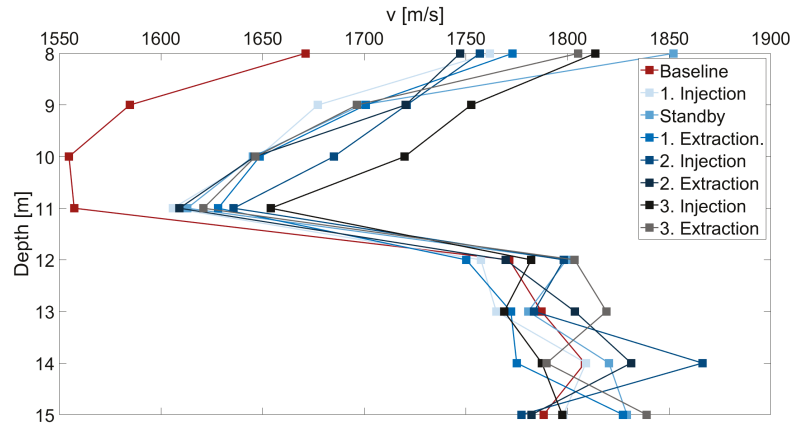
Figure 5.30: P-wave velocity between $RB1$ and $RB2$ during phase 1 of the second heat injection.

83
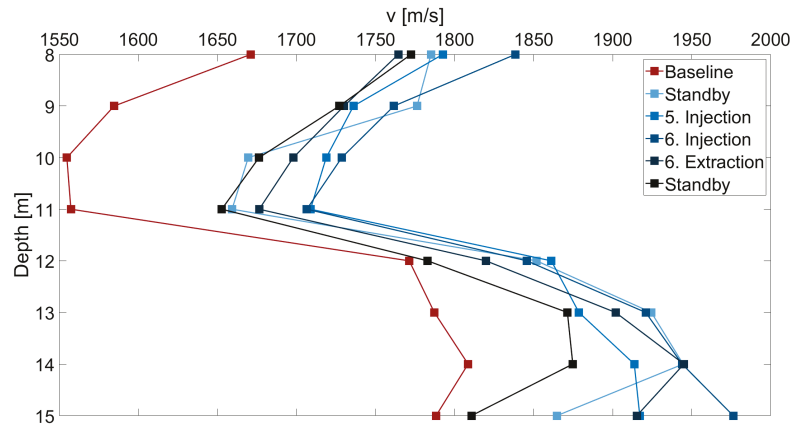
Figure 5.31: P-wave velocity between $RB1$ and $RB2$ during phase 2 of the second heat injection.
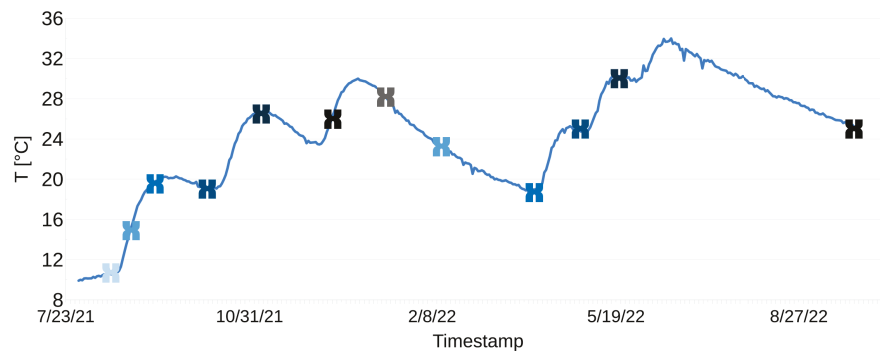
Figure 5.32: Temperature measurement at $RB2$ in $10\,\mathrm{m}$ depth. The coloured marks indicated the coloured measurement time steps of phase 1 and phase 2 in Figure 5.30, 5.31
.

Amplitude, energy and quality factor

The observation of amplitudes is displayed in Figure 5.33 exemplary at 10 m depth for $RB2$. In phase 1 (a) we can see a light drop in seismic amplitude compared to the baseline measurement during the injection period, which becomes stronger during the first standby period. During the extraction phase, the amplitude level reaches the baseline. The measurement of the second standby period takes place right after the second heat injection. The amplitude level decreases. During phase 2 (b), no standby periods occur between the heat injection and extraction. The measurement during the fifth injection shows an increase in the amplitude level whereas an amplitude drop indicates the extraction. The standby signal during the standby period after the cyclic alteration shows similar levels to the standby period before phase 2.

Thereupon the cross-hole energy has been calculated by squaring the amplitude of the signal and is plotted in Figure 5.34. Note that the energy level for the baseline and the first standby measurement are in 10^9. We see a higher energy level at $RB1$ than at $RB2$ for both phases. Nevertheless, we also see a higher energy in Phase 1 compared to Phase 2. Strongest variations happen for $RB1$ during the first extraction and at a depth of 13 - 15 m. The energy level in $RB2$ decreases after the first standby period during extraction. The amplitude in Phase 2 is consistently lower than in Phase 1. Variations in both receiver wells are significant during the sixth extraction.

Interesting behavior shows the quality factor. It is illustrated with depth and shows irregular variations throughout all depths and monitoring cycles in Figure 5.35. During Phase 1, when standby periods slow down the hydraulic stress of the system a manifestation of depth-dependent quality factors is taking place. The amplitude is decreasing during injection and increasing during extraction and standby. During Phase 2 the cluttering increases with stronger variations in 13 - 15 m depth.
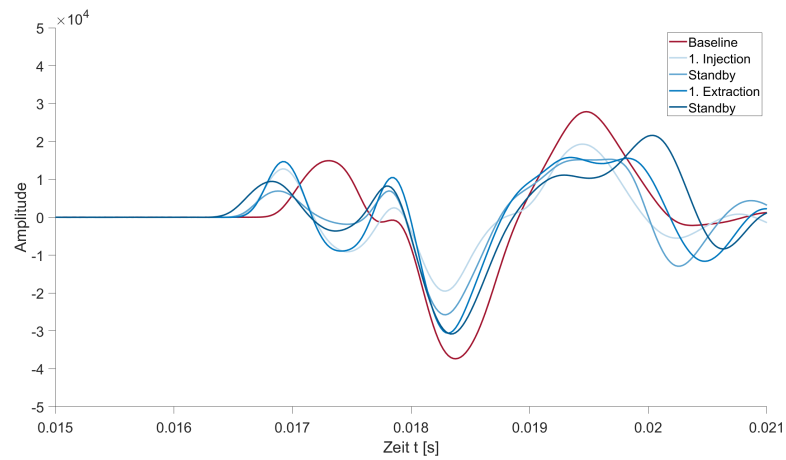
(a) *RB2* Phase 1
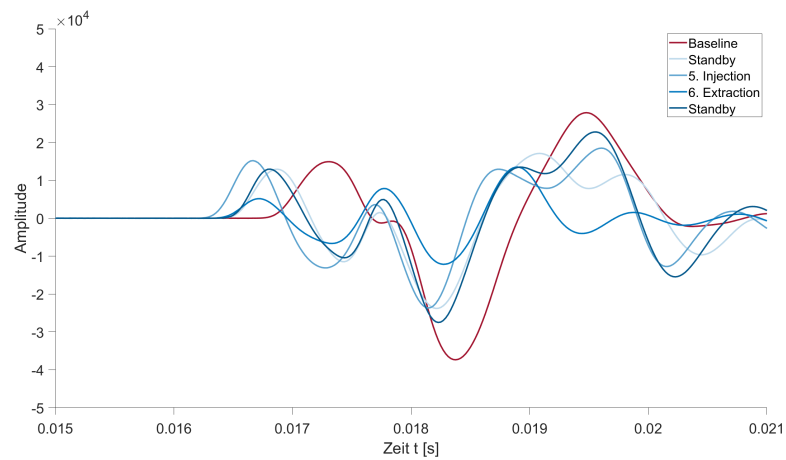
(b) *RB2* Phase 2

Figure 5.33: Time series of the second heat injection monitoring at a depth of 10 m with the focus on amplitude deviation.
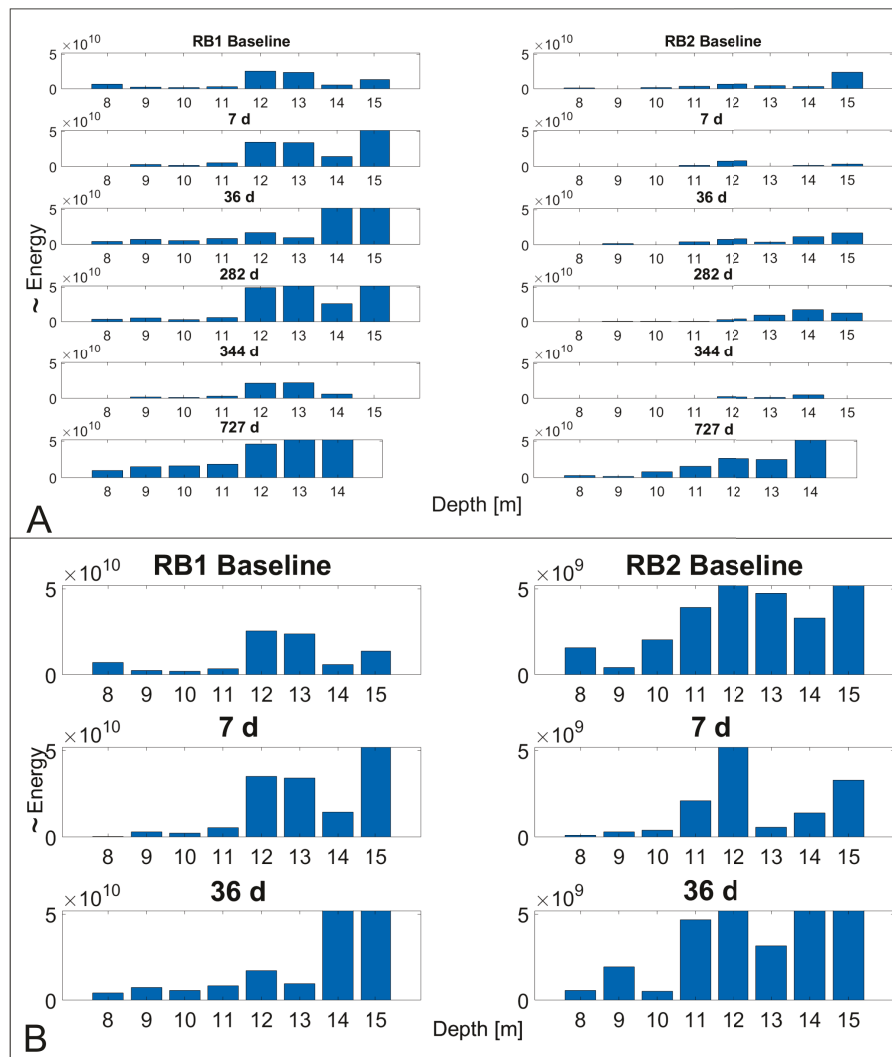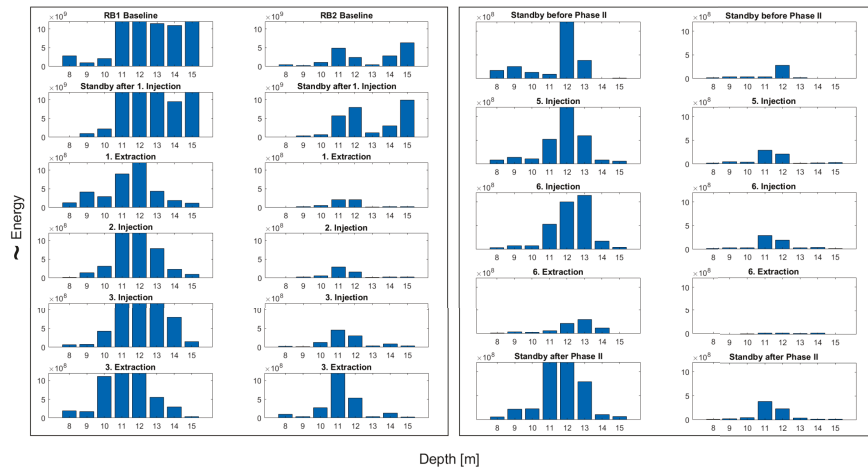
Figure 5.34: Energy levels of the cross hole measurements at different monitoring cycles for phase 1 (left) and phase 2 (right) of the second heat injection experiment. Note the different scale for Baseline and the first monitoring measurement.
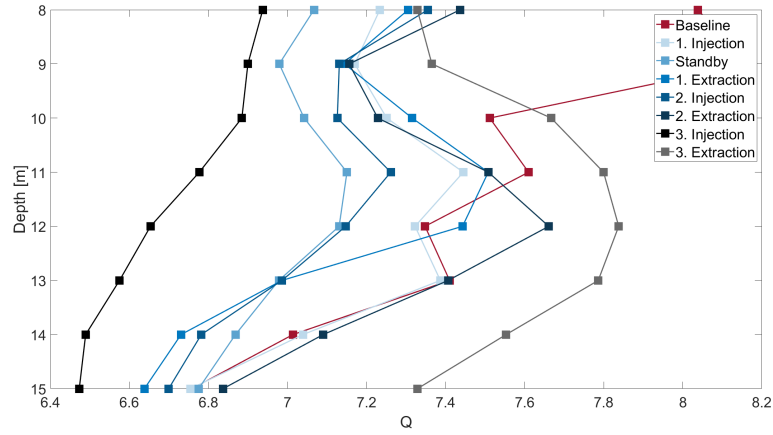
(a) $\Delta E = E_{RB1} - E_{RB2}$
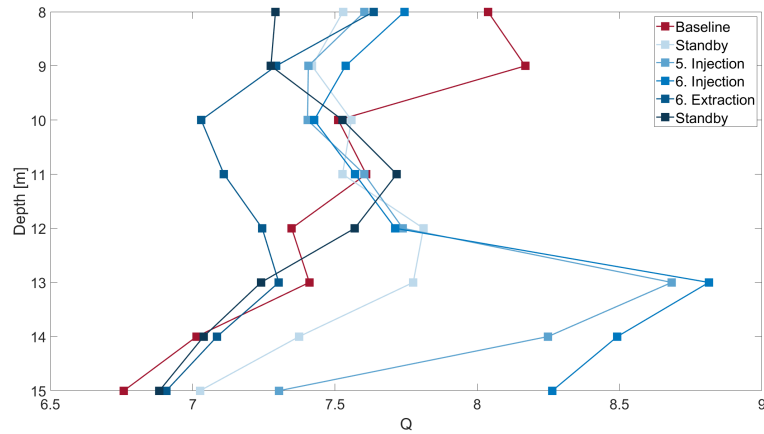
(b) $\Delta E = E_{RB1} - E_{RB2}$

Figure 5.35: a) The quality factor for the second heat injection experiment at phase 1 is inferred from the energy at $RB1$ at each baseline and monitoring cycle. It has been individually divided by the energy dissipation along the travel path energy: $\Delta E = E_{RB1} - E_{RB2}$, b)The quality factor for the second heat injection experiment at phase 2 is inferred from the energy at $RB1$ at each baseline and monitoring cycle. It has been individually divided by the energy dissipation along the travel path energy: $\Delta E = E_{RB1} - E_{RB2}$

6

Discussion

The completed experiments provide high-quality data; thus we managed to develop an experimental set-up where the alterations of subsurface properties happened in coordination of the monitoring scale. The spatial distribution of gas and heat-induced changes have been wide enough to affect our signal. It has also been narrow enough to detect differences within the test site. The results are now taken up here one after the other for interpretation. They will be discussed, among other things, with a view on whether our method is suitable for monitoring gas and temperature-induced changes in the subsurface.

6.1   Methane injection

The initial test site was the methane injection test site. It was performed in the near-surface analogical to [Lamert et al., 2012], measuring CO_2 with ERT, and [Cahill et al., 2017], measuring CH_4 with GPR. In order to detect gas-induced parameter changes with geophysical methods, we applied an old idea to a new issue. We implemented a seismic cross-hole set up, analogous to [Diallo, 2000]. As a result, we closed a gap in near-surface monitoring approaches. With our laborious but favorable re-measurement procedure, we were able to exclude errors due to manually handled equipment (Figure 5.2b). We ensured the repeatability of the experiment and the signal stability in quality. We also assured the procedure of comparing data sets of different time steps. By evaluating P-wave velocities, we could assess the effects of heat-induced parameter changes and hence connect established rock physics theories with hydrogeophysical applications.[Birnstengel et al., 2024].

6.1.1   Borehole deviation, travel time and P-wave velocity

Even after completion of the experiment, it was not possible to measure the actual deviation of each borehole. In order to asses the possible influence, we analyzed the P-wave velocities for both receiver boreholes in Figure 5.3 A. They maintain a lateral distance of 4 m from each other. A similar trend of velocities for both receivers at the baseline measurement signifies a negligible effect of borehole deviation on our measurement. The time series of travel time differences displayed in Figure 5.3 B, C show shifts between the first and the second receiver borehole strongest at 12 m depth. According to the models, the occurring shift in the baseline is likely due to the silty clay boundary. After 49 days past the injection, the travel times in both receiver boreholes are re-approaching baseline level. With this shift and the hydraulic low-permeable layer being situated between 9 - 11 m depth, we assume that gas accumulates beneath the silt layer [Birnstengel et al., 2024]. With the focus of our P-wave velocity analysis on the area between the receiver boreholes $RB1$ and $RB2$ (Figure 3.9) we find the strongest variations of the P-wave velocity within the first two months after injection at a depth of 10 - 13 m (Figure 5.4). Those changes are associated with gas content changes between $RB1$ and $RB2$. At a depth of 9 - 10 m, the velocity remains at a lower level compared to the baseline 49 days after injection. We assume the reason for that to be a slowed process of degassing or dissolving of the gas [Birnstengel et al., 2024], since glacial till has a much smaller permeability than silty sand [Schön, 2004]. A decelerated upwards migration of the injected gas is also a possible explanation. The last monitoring cycle in 355 days after injection indicates no velocity change due to gas saturation changes. We, therefore, assume a complete dissolving of the gas by that time.

6.1.2   Comparison to in-situ soil-water content

[Whiteley et al., 2020] verified their seismic refraction tomography data with the absolute water content in the soil when investigating landslides. We apply this approach to a smaller-scale study in a borehole setup. [Jefferson et al., 1998] studied the effect of the soil-water content on seismic reflection and refraction amplitude. In our setup we compare measured water content inferred from SMT sensors with calculated gas content Θ_g that got derived from calculated water content with the observed P-wave velocities between $RB1$ and $RB2$ (Figure 5.5 A - C). The injection is taking place at 17.5 m depth where we measure an immediate shift at the soil-moisture sensors. It is stronger in higher depths, presumably due to the injection depth. The response of the more distant soil moisture sensors at C06 and D05 at 11 m depths is much weaker (Figure 5.5 A). Alike the mentioned literature, the correlation of water content and P-wave velocity shows that higher gas content corresponds to lower P-wave velocities [Birnstengel et al., 2024]. We use the introduced rock physical relations to estimate the gas content from P-wave velocities and the rock physical properties of the subsurface. Truthfully, performing the calculation of water content or gas content respectively by only relying on the time-average relation does not do

justice to the problem and would narrow the complexity of the topic. One of the approaches is the concept of a "patchy saturation" that allows a simplification of our calculations (Chapter 2.3.1). The detailed comparison of the soil moisture sensor at D05 in 11 m depth with our measured P-wave velocity between $RB1$ and $RB2$ at 11 m depth shows that the calculated P-wave velocity reflects the instant drop of water content by 4.17 %. The P-wave velocity has been obtained five days after the injection showing a drop of 209.73 m/s. The accurate water content at the exact same time amounts to 34.2 % at the water-content measuring well D05 [Birnstengel et al., 2024]. In the gas propagation simulations done by our colleagues in Kiel [Dahmke et al., 2021], they assume that the expected gas plume does not exceed a lateral extent of 2 m radius around the injection point. Well $RB2$ would therefor be affected by gas-induced changes, $RB1$ would not. In our data, we see variations in both receiver wells. We assume, that both wells are affected by gas-induced changes of the rock physical properties. A direct comparison between water content and seismic P-wave velocity is still valid when we take into account that the seismic P-wave transports 2D information on the path between the source and receiver. For higher accuracy, however, the monitoring interval should be increased around the injection period [Birnstengel et al., 2024]. Calculating Θ_g in table 5.1, referring on equation 2.6 complies very well with P-wave velocity data and water content data five days after injection at 11 m depth, where we measure a gas content of 4,9 %. The calculated percent deviation with the measured absolute deviation shows a very good correlation. Therefore, we find our seismic cross-hole measurement not only capable to indicate but also to quantify relative gas content changes in the subsurface. However, [Li and Schanz, 2011] announce that the anomaly of P-wave velocities versus gas saturation happens with even smaller gas content. This cannot be verified with our field data. The recorded fluctuations also indicate heterogeneous distribution of the gas plume. Figure 5.5 shows the compliance of these three parameters but also their following increase beyond baseline level at the end of the monitoring process [Birnstengel et al., 2024]. We do not consider information about the initial absolute water content but only travel time data; thus we are comparing gas content rather than saturation, which is why we do not set the measured moisture content result in relation to the absolute water content here. Analyzing the approach of [Mavko et al., 1995] of inferring K without knowing the S-wave velocity (Equation 2.8, Table 5.3) shows rather high gas contents. Those calculations consider density properties in the subsurface. Although core samples have been analyzed during the project, it was not possible to include density parameters and their variability during the injection process in this work. Thus changes in density can not be evaluated and reconsidered during the experiment, and we cannot provide realistic density assumptions. Therefore this gas content estimation is not fully parameterizable [Birnstengel et al., 2024].

6.1.3 Amplitude, energy and quality factor

We can observe various effects by looking at the amplitude's behaviour before and after the injection process. Since the amplitude signal carries volume information, the levels should not be compared between depths but only one depth over different time steps. Five days after the injection, the amplitude drops in $RB1$ and $RB2$ at all depths as a result of the present gas and the associated reduction of the bulk modulus (Figure 5.6). Amplitude changes are clearly depth-dependent during the gas upwards migration process (Figure 5.7 A, B). In the hydraulic low-permeable layer, the restoring process to the baseline level happens faster than underneath the hydraulic low-permeable layer. The amplitudes increase is stronger in $RB1$ 49 days after injection. That could indicate a gas trapping beneath the hydraulic low-permeable layer. Both receiver boreholes show that the maximum amplitude in 12‑13 m remains at the level of 30‑60 %, whereas the amplitude in 9‑11 m reaches and exceeds the baseline level by 40 %. This could, in fact, indicate a sustainable change in the subsurface pressure distribution, variations in the pore filling or changes in grain-to-grain contact, provided that the gas has been injected with hypercritical pressure [Birnstengel et al., 2024]. Looking at single quality factors in Figure 5.9 A, obtained from the stored energy in $RB1$ and the dissipated energy in $RB2$, a depth dependence is visible in the baseline. Assuming the stored energy to be stable over time, the dissipation of energy in the upper level is smaller than below the low-permeable layer. With the injection of gas, the quality factor is leveled for all depths, which means either a reduction of the stored energy at $RB1$ or an increase of dissipation at the upper level (reverse behavior below the hydraulic low-permeable layer [Birnstengel et al., 2024]). Several monitoring cycles after the injection, the quality factor behaves homogeneous over depth (Figure 5.9 A). During the assumed dissolving and fluctuation process of the gas, a depth dependence is evident. Below the hydraulic low-permeable layer, the energy level is higher compared to the baseline measurement. At 9 m depth, the dissipation decreases with the gas content. According to Figure 5.6, both boreholes are affected by an amplitude decrease. Therefore, we look at the quality factor inferred from the energy at $RB2$ for the baseline measurement divided by the energy dissipation at each monitoring cycle (Figure 5.9 B). We note that the quality factor increases significantly. The level of stored energy in the upper level is very high compared to the energy level of the first monitoring cycle. Zooming in (Figure 5.9 B) shows that the trend continues for the later monitoring cycles. This behavior would suggest a more extended durability of the gas in the upper level [Birnstengel et al., 2024].

Fresnel volume

Another explanation of the amplitude exceeding baseline level in the hydraulic low-permeable layer could be its affection by changes on a spacious level. To gather signal information, we integrate over a larger area than just the direct pathway; thus, we need to take the Fresnel volume around the central ray

into account [Birnstengel et al., 2024]. The background model describes homogeneous water-saturated sand $v_{\text{sand}} = 1630\,m/s$ intermittent by silty clay $v_{\text{clay}} = 1760\,m/s$, a low permeable layer. After injecting the gas, a gas-water-saturated area is described by a circle for $d = 4\,cm$ and $v_{\text{gas−water}} = 1000\,m/s$ at z = -12 m and x = 15 m We calculate the weighting function with frequency measured during the baseline (f = 533 Hz) monitoring and the second monitoring cycle (f = 466 Hz) in 10 m depth in homogeneous sand. The resulting Fresnel volume is illustrated in Figure 6.1. Due to the loss of high-frequency content from source to the receivers, we simplify the layout by calculating and comparing the Fresnel volume only with the highest measured frequency in $RB2$ during baseline and the first monitoring measurement. The modeling of the baseline measurement shows a deviation of the direct travel path caused by the low permeable layer. The occurrence of the gas phase focuses the signal's sphere of influence. At the same time, this additional low-velocity area guides the path towards the low-permeable layer. The higher the velocity contrast between the layer, the higher the deviation, or rather the guidance along the barrier. We find that along with the frequency decline after gas injection, the sphere of influence on the seismic wave decreases, and the deviation increases at the same time. This could explain that the amplitude exceeds the baseline level when gas is trapped underneath the hydraulic low-permeable layer but supports the assumption that the gas is not fully dissolved yet [Birnstengel et al., 2024]. Generally, we have to conclude that we can not assume 1d conditions to simplify our analysis. However, we are conducting time-lapse measurements that allows us to refer to a baseline measurement. We can account all changes in the subsurface to changes in the saturation (or temperature) parameter.
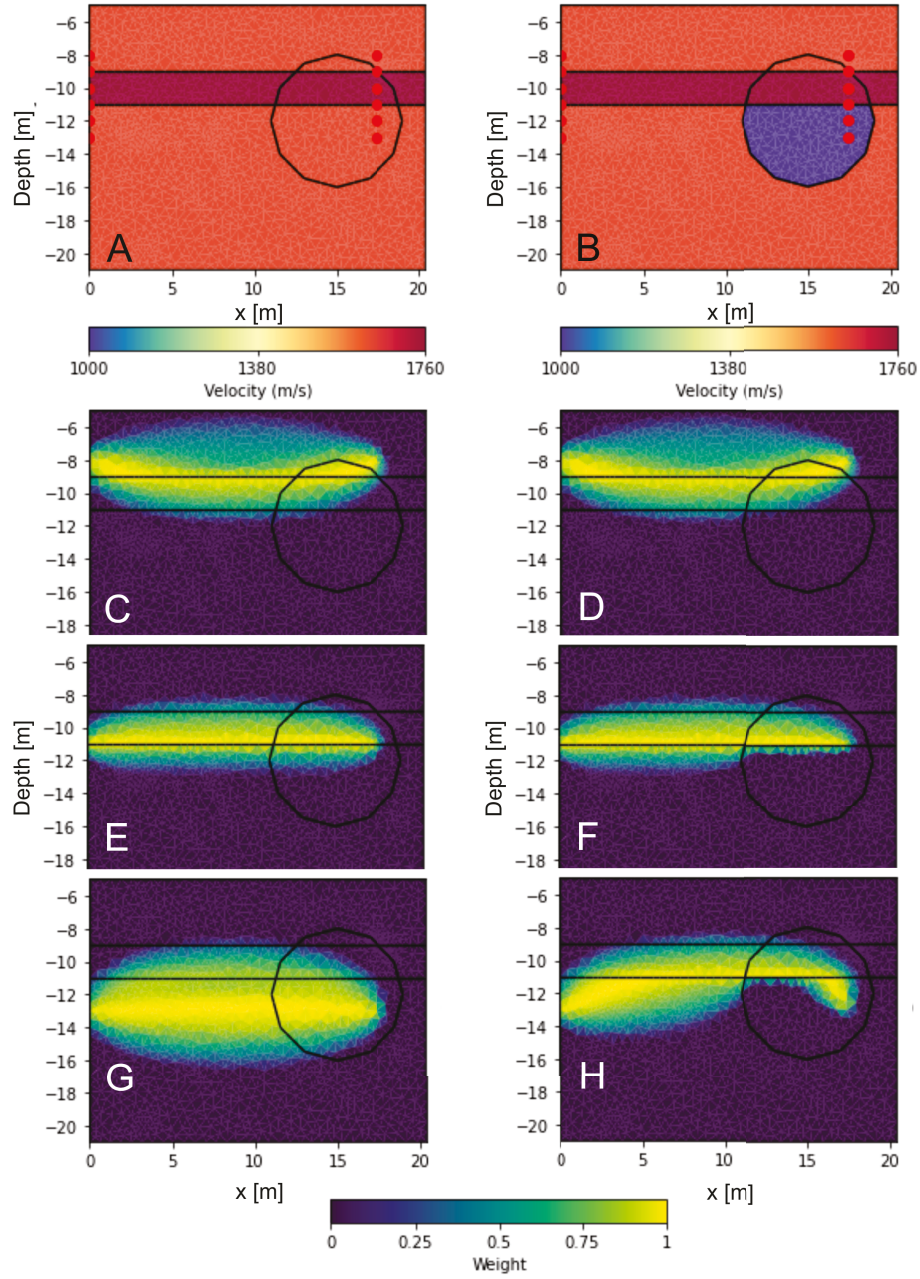
Figure 6.1: Extent of the Fresnel volume for methane injection at 8, 11 and 13 m depth during (A) baseline monitoring with f = 533 Hz and during (B) the first monitoring cycle five days after injection with f = 466 Hz [Birnstengel et al., 2024].

We performed the hydrogen injection experiment in imitation of the methane injection experiment. The remarks concerning our measuring and analyzing routines apply here analogous with Figure 5.11 illustrating the repeatability of the experiment exemplary in 14 m and 17 m depth.

6.1.4   Borehole deviation, travel time and P-wave velocity

The P-wave velocities for both receiver boreholes in Figure 5.12 A show the negligible effect of borehole deviation on our measurement. The time series of travel time differences displayed in Figure 5.12 B, C indicate a significant shift between the first and the second receiver borehole strongest between 12 - 15 m depth. After 96 days past the injection, the travel times in both receiver boreholes are re-approaching baseline level. With this shift and the hydraulic low-permeable layer being situated between 10 - 12 m depth, we assume that gas accumulates beneath the silt layer [Birnstengel et al., 2024] or is at least diffusing at a very low rate through the low permeable layer. Although not equally, both wells are effected by the saturation change due to the gas injection. We, therefor, focus the further P-wave velocity analysis on the area between the receiver boreholes $RB1$ and $RB2$ (Figure 3.10). The strongest variation of the P-wave velocity happens within the first month after injection at a depth of 11 - 15 m depth (Figure 5.13). They are associated with gas content changes between $RB1$ and $RB2$. As mentioned before, this could be due to a slower process of degassing and dissolving. A slowed upwards migration of the injected gas is also possible. During the last monitoring cycle 441 days after injection, velocity changes occurred at 11 m depth. This affects the low permeable layer and could be due to a slowed dissolving and transport process or trapped gas bubbles within the layer.

6.1.5   Comparison to in-situ soil-water content

Similar to the investigation of the methane injection experiment, we compare measured water content and calculated gas content Θ_g using the observed P-wave velocities between $RB1$ and $RB2$ (Figure 5.14 A - C). The injection is taking place at 18 m depth. We measure a strong reaction at the soil-moisture sensors at D07 in higher depths, close to the injection lances. The wells D04 and D07 have the same distance to the injection lances. We can see that higher gas contents correspond to lower P-wave velocities. Using the introduced rock physical relations allow estimations of the gas content derived from P-wave velocities and the rock physical properties of the subsurface. The detailed comparison of the soil moisture sensor at D07 in 14.3 m depth with our P-wave velocity measurements at 14 m depth shows an instant drop of water content by 15 % that is reflected by the calculated P-wave velocity. The P-wave velocity was obtained four days after the injection showing a drop of 150 m/s. The accurate water content at the exact same time amounts to 30.89 % at the water content measuring well D07. Several gas propagation simulations have been done by our colleagues in Kiel [Dahmke et al., 2021]. 1.) They assume that a thin gas layer

migrates underneath the low permeable layer, which exceeds a lateral extent of 30 m radius around the injection point with a direct upwards migration at the injection lances. 2.) An egg-shaped plume forming that does not exceed 5 m radius around the injection well. 3.) An upwards migration with a lateral migration up to 10 m radius in 10 - 11 m depth. $RB1$ and $RB2$ are located in a distance of 24 m from each other, with $RB1$ having a distance of 13.7 m from the mid injection well. Influences of gas-induced parameter changes would be visible in $RB1$ if the gas migration exceeds 13 m. Taking into account, that the P-wave transports 2D information on its travel path we can compare water content and seismic P-wave velocity. We would undoubtedly achieve higher accuracy if the monitoring interval is increased around the injection period. To extend our qualitative study to extract quantitative results by connecting P-wave velocities and gas content. Calculating Θ_g in Table 5.4 referring to equation 2.6 complies very well with water content data, for example, 4 days after injection at 14 m depth with a gas content of 42.6 % and 25.9 % in 15 m depth, calculated after [Mavko et al., 1995]. The values calculated with the time-average relation are slightly higher than those calculated after [Bachrach and Nur, 1998]. The compared calculated percent deviation with the measured absolute deviation show a good correlation.

The hydrogen injection shows, alike the methane injection experiment, that the seismic cross hole setup is capable of quantifying relative gas content changes in the subsurface. However, also here in this experiment, we cannot verify that the anomalies of P-wave velocities versus gas saturation happen with even smaller gas content announced by [Li and Schanz, 2011]. Analyzing the approach of [Mavko et al., 1995] of inferring K without knowing the S-wave velocity (Table 5.3) works very well in this experiment. Those calculations consider density properties in the subsurface. Changes in density can not be evaluated and reconsidered during the experiment; thus we cannot provide realistic density assumptions. Therefore this gas content estimation is not fully parameterizable [Birnstengel et al., 2024] but shows nevertheless sensible results in our hydrogen injection experiment.

6.1.6   Amplitude, energy and quality factor

The amplitude analysis before and after the injection process shows similar effects as already known from the methane injection experiment. The amplitude drops four days after the injection in $RB1$ and $RB2$ at all depths as a result of the present gas and the associated reduction of the bulk modulus (Figure 5.15). During the process of gas upwards migration, the amplitude levels are clearly depth-dependent (Figure 5.16 A, B). In $RB1$ and $RB2$ the level of amplitudes is different due to picks at various depths. The levels should, therefor, not be compared between depths but only within one depth over different time steps. $RB1$ shows higher amplitude levels than the baseline measurement throughout the monitoring process. It is very unlikely that the changes in the hydraulic condition are prominently visible in $RB1$ and not in $RB2$. Unless, the conditions changed in the whole area, also detectable in $RB2$ and the signal in $RB2$

has been superimposed by the attenuation effect of the gas. In $RB2$ we see a clear influence of the gas-induced parameter changes on the amplitudes. The attenuation is visible through all depths. We can also see that variations within depths do not occur for the first month. The amplitude changes back to the baseline level. That is happening faster in 13 m and 16 m depth. This would speak for a high permeable layer with higher degassing or dissolving rates at this depth. Comparing the HPT and core data, we find high permeable layers of coarse-grained sand from 11 m downwards. If the pressure distribution has been changed sustainably after the injection, it would explain the high amplitude rates in $RB1$ by variations in the pore filling or grain-to-grain contact changes. The results of the energy analysis show that the distribution of the cross hole energy decreases in $RB2$ for depths between 10 m to 16 m. In $RB1$, the energy level is generally higher, increasing with the injection. Looking at single quality factors in Figure 5.18 A, obtained from the stored energy in $RB1$ and the dissipated energy in $RB2$, we can see a depth-dependence again. With gas injection the quality factor is leveled for all depths, which means either a reduction of the stored energy at $RB1$ or an increase of dissipation. If the stored energy in $RB1$ is increasing, we can assume that the energy dissipation is also increasing. Several monitoring cycles after the injection, the quality factor is homogeneous over depth (Figure 5.18 A). During the assumed dissolving and fluctuation process of the gas, depth dependence is evident. In 12 m and 15 m depth, the energy in $RB2$ decreases faster. According to Figure 5.15, both boreholes are affected by an amplitude decrease. Therefore, we look at the quality factor inferred from the energy at $RB2$ for the baseline measurement divided by the energy dissipation at each monitoring cycle (Figure 5.18 B). We note that the quality factor increases after the injection. The level of stored energy is high compared to the energy level of the first monitoring cycle. Zooming in (Figure 5.18 B) shows that the trend continues for the later monitoring cycles. This behavior would again suggest a longer durability of the gas in the upper level [Birnstengel et al., 2024]. 441 days after injection Q gets closer to one, which means that ΔE gets smaller. As we noted by looking at the energy level, the energy increases with time. Like that, we can see negative Q values.

Fresnel volume

The background model for the hydrogen injection is also described by homogeneous water-saturated sand $v_{\mathrm{sand}} = 1650\,m/s$ intermittent by silty clay $v_{\mathrm{clay}} = 1760\,m/s$, a low permeable layer. After injecting the gas, a gas-water-saturated area is described by a circle for $d = 4\,cm$ and $v_{\mathrm{gas-water}} = 1300\,m/s$ at z = -15 m and x = 38 m We calculate the weighting function with frequency measured during the baseline (f = 520 Hz) monitoring and the second monitoring cycle (f = 361 Hz) in 12 m depth within homogeneous sand. The resulting Fresnel volume is illustrated in Figure 6.2. We note that the energies and, therefor, amplitudes are exceeding baseline level in $RB1$ and $RB2$. Similar to the previous experiment, the weighting function has been calculated with our max. frequency during the baseline monitoring (f = 520 Hz) and the second monitor-

ing cycle (f = 361 Hz) in 14 m depth. We notice that the sphere of influence is increasing after the injection (Figure 6.2C and D, C and H), and the deviation is also increasing. The increasing sphere of influence after the injection could explain that amplitudes exceed base line level in $RB1$ (Figure 5.15).

[Sheriff, 1975] announces that gas in solution does not behave like a gas at all. We can, therefor, assume a decrease of the amplitude. Contrarily the author points out a lensing effect of gas sand that would bunch and focus energy which would speak for an increase in the amplitude. Also, the impedance behavior on the phase boundaries could affect the focus of energy. We could also explain the amplitude behavior with the presence of a residual gas phase. This has been confirmed by geochemical analysis from colleges in Kiel [Dahmke et al., 2021]. Despite all the simplifications in our monitoring experiment (parallel transmission, controlled change of the saturation parameter, analyzing velocity and amplitude of a pressure wave), we observe a distinct impact on the energy and, therefor, amplitude, which cannot be sufficiently explained. Since the amplitude variation of seismic energy depends on more than just one subsurface condition, there is no simple relationship between amplitude and something significant [Sheriff, 1975]. Whilst repetitive and resilient, the whole signal underlies a complex behavior in the subsurface. It is necessary to develop a model concept which explains the amplitude increase since our observations differ from the common concept. New studies show [Solazzi et al., 2021], when the water content in the vadose zone changes, accounting for capillary suction effects is necessary to explain the observed variations in surface-wave dispersion. This could also apply to gas injections. A full-waveform analysis of this data set would be of great interest, also for tackling potential frequency dependencies, but must handle high frequencies and the elastic approximation in order to image the low variations of the time-series application [Köhn et al., 2013, Köhn et al., 2017]. Another approach would be the analysis of S-wave behavior which would require different well sizes and borehole equipment. This basic field experiment shows the urgent need for further and continuative investigations of rock physical dependencies at the field scale [Birnstengel et al., 2024].

6.2   Heat injection I

In the first heat injection experiment, hot water was injected once into the subsurface. The monitoring measurements covered the heating and cooling processes in the subsurface. The remarks concerning our measuring and analyzing routines apply here analogous to the gas injection experiment with Figure 5.20 illustrating the repeatability of the experiment exemplary in 9 m and 15 m depth.

6.2.1   Borehole deviation, travel time and P-wave velocity

In the first heat injection experiment, the receiver boreholes have a lateral distance of 7.5 with no influential borehole deviation, as we can see similar P-wave velocities for both receiver boreholes (Figure 5.21 A). The times series of travel
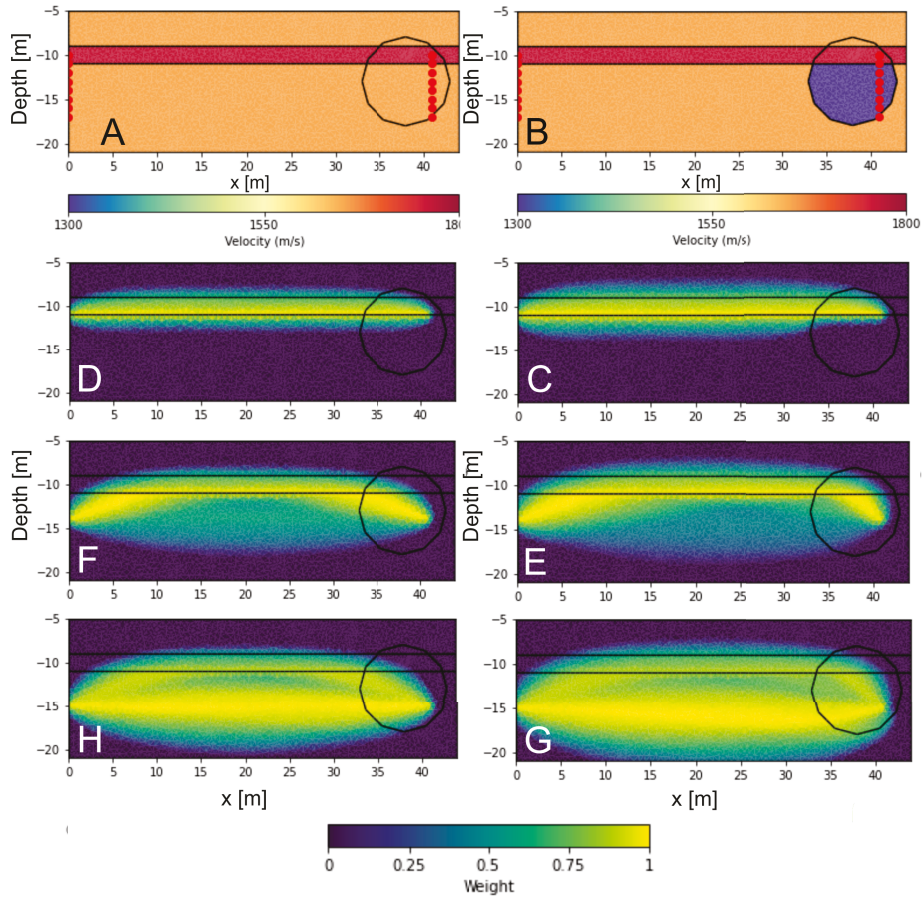
Figure 6.2: Extent of the Fresnel for hydrogen injection at 11, 14 and 15 m depth for (A) baseline monitoring with f = 520 Hz and (B) during the first monitoring cycle 4 days after injection with f = 361 Hz. [Birnstengel et al., 2024].

time differences illustrated in Figure 5.21 B‑D for three time steps shows a possible outlier seven days after injection in 11 m depth. The trend shows minor changes in the travel time difference occurring between 8 and 11 m depth seven and 36 days after injection. In 9 m depth, we can see a difference in travel time 266 days after injection for $RB2$. The area between both receiver wells is affected by heat-induced changes, mainly detectable between 8 - 11 m depth. We focus the analysis on the area between $RB1$ and $RB2$. The P-wave velocity shows a strong shift in 12.5 m depth visible in Figure 5.22. The core analysis in Figure 3.11 show hydraulic low permeable silty sand at a depth of 14 m. Nevertheless, more compact material may be located in shallower areas within the test site producing this shift. We can also see a reduction of the P-wave velocity between baseline and the first two monitoring cycles by 50 m/s between 8-11 m depth. With the last monitoring cycle 344 days after injection, we found no indication of heat-induced changes in the velocity analysis. We assume that the subsurface temperature is back to its origin. The increase in velocity due to temperature changes in the subsurface is nevertheless inconsistent in the data.

6.2.2 Amplitude, energy and quality factor

The amplitude, here exemplary shown for 8 m depth in Figure 5.23, indicates different effects whether we look at $RB1$ or $RB2$. In $RB1$, we would assume a minor effect of temperature-induced changes due to the groundwater flow direction from NW to SE. We can see a reduction of amplitude, which signifies a higher attenuation seven days after injection in both receivers. 36 days after injection, the amplitude level is equal to the baseline in $RB1$ but still on a lower level in $RB2$. This could mean that the higher temperatures are to find within a smaller radius. In $RB1$, we recognize that the amplitude is rising higher than baseline level, and we assume, that the hydraulic setting has been changed during the injection process. However, we can not see the effect in $RB2$ where the amplitude level is still lower than baseline. Looking at the energy level derived from squared amplitudes (Figure 5.24), we see effects between 8 - 10 m depth. At the end of the survey, the energy changed to a higher level in $RB1$ in almost every depth. The quality factor at figure 5.25 shows an expected drop between 8 - 9 m depth and between 11 - 13 m depth. According to [Jaya et al., 2010], the quality factor is rising with higher temperatures between 50 - 150°C. They attribute that behavior to the temperature-dependent viscosity and velocity of the pore fluid and find it more likely that the increase of quality factor (decrease of attenuation) in the temperature range 50-125 °C is related to a quick decrease of viscosity. We found no statements for lower temperatures that exclude perpetuating effects due to steam bubbles.

Fresnel volume

The background model for the heat injection is also described by homogeneous water-saturated sand $v_{\mathrm{sand}} = 1750 \, m/s$ intermittent by silty clay $v_{\mathrm{clay}} =$

$1650\,m/s$, a low permeable layer. The seismic baseline provides lower P-wave velocities at the low permeable layer, which differs from the gas injection experiments. After injecting the heat, a temperature-induced area is described by a circle for $d = 4\,cm$ and $v_{\text{temperatur}} = 1800\,m/s$ at z = -14 m and x = 20 m We calculate the weighting function with frequency measured during the baseline (f = 461 Hz) monitoring and the second monitoring cycle (f = 569 Hz) in 14 m depth in water-saturated homogeneous sand. The resulting Fresnel volume is illustrated in Figure 6.3.

The deviation of the travel path looks different due to the inverted velocity arrangement. The velocity contrast between the water-saturated sand and the temperature-induced area is comparatively small, and we can still see a sphere of influence that is more focused in Figure 6.3 F, H compared to the baseline model.
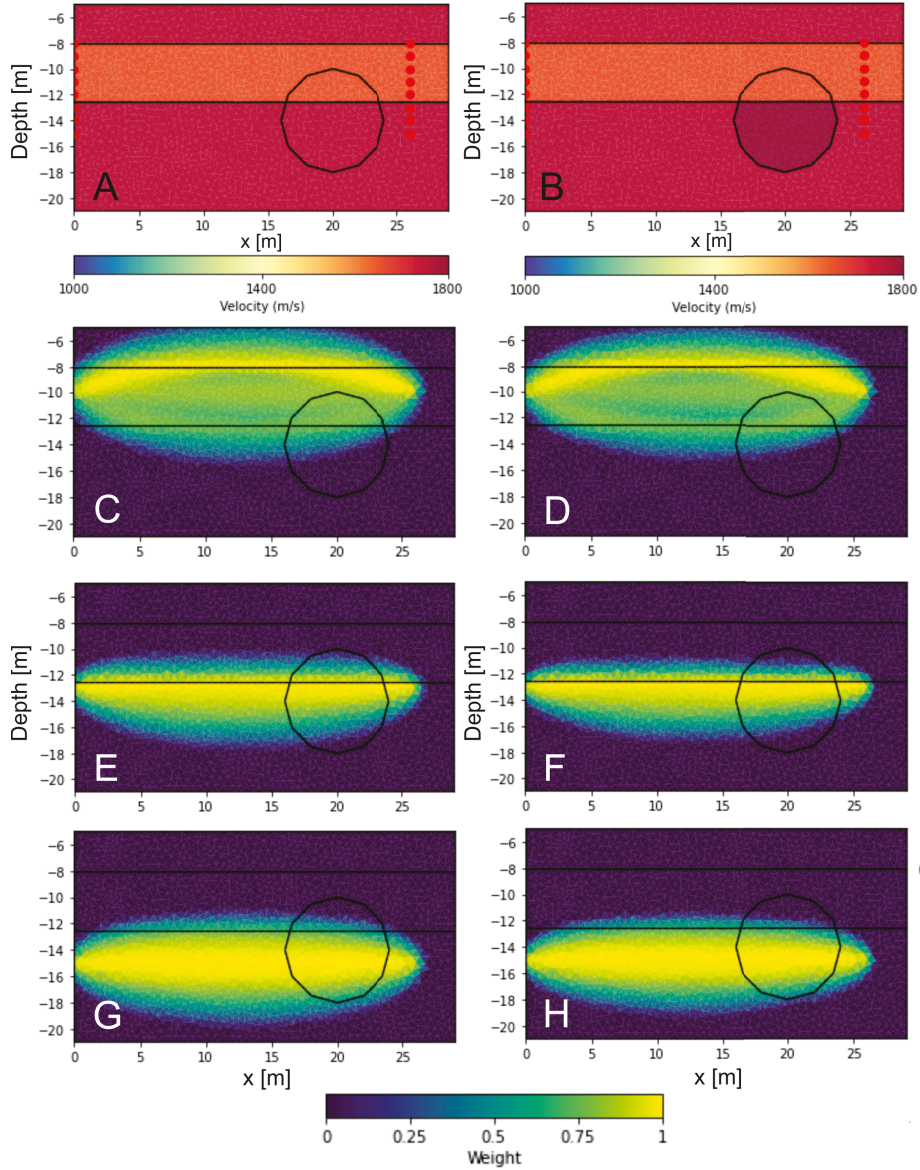
Figure 6.3: Extent of the Fresnel volume for the first heat injection at 10, 13 and 15 m depth with A) baseline monitoring f = 461 Hz and (B) during the first monitoring cycle 7 days after injection with f = 569 Hz.

6.3   Heat injection II

A follow-up project used a rather extensive seismic outlay for different heating scenarios by shooting back and forth as well as perpendicular to the groundwater flow direction. Longer heating duration, closer monitoring during heating, standby and cooling periods and highly frequent heating-cooling cycles have been achieved. Only a brief data analysis will be part of this thesis. The injection experiment has been parted in two phases. When the first phase comprises standby periods after heat injection and extraction, they will be missed out in the second phase . The repetitive signal (Figure 5.27) returned clear first breaks of the P-wave and clear channels on the record. The repeatability is ensured by the same procedure (Figure 5.28).

6.3.1   Borehole deviation, travel time and P-wave velocity

The analyses of the P-wave velocities for both receiver boreholes that face a lateral distance of $6.65\,\mathrm{m}$ shows again the same trend with depth. Similar P-wave velocities for both receiver boreholes construe a negligible effect of borehole deviation on our measurements. The times series of travel time differences, illustrated in Figure 5.29 B - D show different scenarios: a heat injection, a standby and a heat extraction period. All three scenarios show minor changes in the travel time differences occurring. Again, the focus will be laid on the analysis at the area between $RB1$ and $RB2$. Between $8\,\mathrm{m}$,-,$12\,\mathrm{m}$ depth, the velocity increase during the injection and its decrease during the extraction with slight variations during the standby period is visible in Figure 5.30 and 5.31. During the experiment's first phase, the layer beneath the aquifer shows no continuous decreasing or increasing in P-wave velocity. As for the second part of the experiment, where the cyclicity of the injection and extraction phases increases in frequency, the aquiclude reacts on the injection with increasing P-wave velocities. As we were shooting perpendicular to the groundwater flow direction (NE - SW), a time delay between injection and detectable reaction in the shooting axis is very likely.

6.3.2   Temperature dependent seismic velocities

As already stated by [Wang and Nur, 1990], the influence of temperature on seismic velocity strongly relates to thermo-physical characteristics of the corresponding pore fluid. Figure 6.4 shows that with increasing temperature, the P-wave velocity trends to increase as well. This proofs the statement of [Wang and Nur, 1990] considering the findings of [Grosso and Mader, 1972] that the P-wave velocity of pure water increases between 0 - $74.4\,°\mathrm{C}$. P-wave velocity shifts due to the influence of the surrounding sediment evoking higher P-wave velocities than pure water.

In the work of [Heldt et al., 2021a], it is visible that the temperature sensors detect higher temperatures in shallow areas (6 - $7\,\mathrm{m}$ depth) compared to deeper areas ($13.5\,\mathrm{m}$ depth), although the injection takes place between 7 - $14\,\mathrm{m}$ depth.
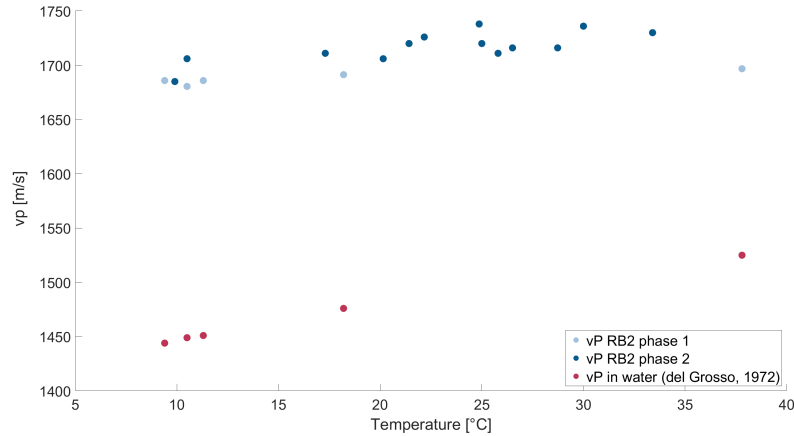
Figure 6.4: Similar trend of P-wave velocities during heat injection phase 1 (light blue), phase 2 (dark blue) and the lab inferred from
[Grosso and Mader, 1972] undertaking P-wave velocity measurements with pure water (red). A velocity shift is visible when comparing pure water measurements with actual soil

The measured temperatures are about 30 °C higher at the top of the aquifer than those near the aquifer bottom. The authors propose thermally induced convection processes that are also responsible for a faster cooling process in the shallow parts of the aquifer compared to the cooling process in the deeper areas.

6.3.3   Amplitude, energy and quality factor

The amplitude, shown for $10\,\text{m}$ depth in Figure 5.33 indicate different effects when observing $RB2$ in phase 1 and phase 2. During the long-duration injection periods in phase 1 the injection entails a slight drop in amplitude, but attenuation becomes more obvious during the standby phase. Extraction of the heat results in an increase in the amplitude level. The following decrease can be explained by a calming and levelling of the hydraulic regime. In phase 2 the alterations of injection and extraction happened faster without a standby- and recover time for the hydraulic regime. The fifth injection even shows a higher amplitude level. The attenuation is visible during the extraction process. Only the standby scenarios show comparable results. The heterogeneous distribution of the hydraulic conductivity in the subsurface can cause spatio-temporal differences in the reaction delay. This behavior is reflected by the energy level in Figured 5.34. $RB2$ shows a lower level than $RB1$ due to absorption and attenuation effects. In Phase 1 the Standby after the first injection shows no significant change in the receiver boreholes. The level decreases by a decimal power during the first extraction phase and stays low until the third extraction takes place in $RB2$. Time shifts are very likely to happen since the whole system is ma-

nipulated by heat injections and extractions. When looking at the Figure 5.32, we see that the extraction occurs when the temperature is at its peak in $RB2$ after the first injection. This correlates with a low amplitude level during this monitoring period. The second injection takes place when the temperature is at the same level as during the first extraction. The second extraction and third injection take place at almost the same temperature level in $RB2$. After the third extraction the temperature was at its highest during the first phase. We must consider that the seismic signal integrates over changes along the path. A direct comparison between temperature and amplitude at a specific borehole and depth is impossible. Phase 2 is characterized by even faster heating- and cooling circles. The sixth extraction marks the global temperature maximum in $RB2$ and both receiver wells' global minimum of amplitude. The initial heating from 9 to 20°C results in a decrease of amplitude by the power of ten. An amplitude decrease with temperature is visible in the data, although not distinctively specific in place and time. The quality factor can give a more orderly overview. Phase 1 shows the decrease during the heating and standby period, and the retreat during the extraction phases. The third injection is quite significant by a minimum Q over all depths (Figure 5.35 a). The overview of the quality factors in Phase 2 is already more promiscuous. And alike the curve of the third extraction in phase 1, the fifth- and sixth injection show higher quality factory in 13 - 15 m depth compared to the baseline. The smaller the energy level difference between $RB1$ and $RB2$, the higher the quality factor. Due to the high cyclicity of injection and extraction the hydraulic regime receives more stress compared to slow process changes. The decrease of the amplitude could be due to a decrease in the water's viscosity.

7

Conclusion

With our various injection scenarios, we evidently modified the hydrogeological parameters at the near-surface. The Quaternary-shaped land was widely explored and the application of cross-hole seismic survey enabled us to detect gas and heat-induced changes on the rock matrix in the field scale. Our seismic monitoring before and after the alteration of the pore fluid provided a unique data set. Its comparable time series of P-wave travel time, velocity and seismic amplitude data contribute to the diversification of exploration methods in the near surface. With this new approach, we have been able to generate highly repeatable time-lapse data when monitoring the impact of gas and heat injection over a period of at least 12 months. The boreholes were drilled to a depth up to 20 m. Three of them are positioned inline. The source borehole was equipped with a sparker and the receiver borehole with one hydrophone chain each. This method enabled us to identify gas and heat-induced changes in the subsurface and thus paved the way for a ready-to-apply field approach to monitor gas and heat storage facilities

Gas

The experimental design is suitable for monitoring gas-induced changes reflected by seismic velocity and amplitude-related values at the field scale making it qualitatively important. Based on this we undertook quantitative statements and compared P-wave velocities with absolute water content measurements. Gas content values derived from water content measurements were compared to calculated gas content values. We discussed different approaches for quantifying gas content changes by comparing Gassmann's equations and the time-average relation. With the concept of a "patchy saturation", we discovered a suitable method for our methane injection experiment with a measurement accuracy of 0.2 Vol.% in the subsurface by analyzing seismic P-wave velocities. Gassmann's equations for the hydrogen injection experiment were very promising in reflecting the gas content results. It shows again the relevance of a suitable model selection and the importance of parameter determinability throughout the monitoring. The challenge here will be the realistic mapping of the subsurface density

and its alteration during the injection process. For higher accuracy, it is furthermore essential to increase the monitoring interval. Discussing the seismic amplitude and the associated quality factor finalized the data evaluation. Even though its behavior is not fully resolved, several factors can be responsible for that. Whether a sustainable change in the subsurface pressure regime or the increasing sphere of influence, as the analyses using the Fresnel volume would suggest. The more extended durability of the gas in the upper level or a trapped gas underneath the low permeable layer supports the assumption that the gas may not be fully dissolved yet and that a residual gas phase is present. As already discussed, does the amplitude underlie a complex behavior, and even suction effects can be considered in future studies.

Temperature

The experimental design is as well suitable for monitoring heat-induced changes reflected by seismic velocity and amplitude-related values at the field scale. The temperature range is of great significance as the response of the geophysical proxy reacts to the thermo-physical behavior of the pore fluid. This, however, underlies physical concepts itself. We found that water behaved differently below and above 74 °C. The P-wave velocity indicated the increasing temperature at the subsurface by increasing. The amplitudes decrease after heating was also a plausible effect assuming an increase in attenuation due to a higher derangement. We have to consider the time shift when comparing conditions in time and space. Thus, a qualitative statement is not yet possible since the bulk modulus and the temperature-dependent velocity directly relate to the density. It remains delicate to compare distinct values, measured at the boreholes, with data that integrates over travel path line or volume. The duration and cyclicity considerably impacted the geophysical proxies indicating that frequent injection alterations affect the hydraulic regime of the aquifer.

The amplitude behavior for both experiments could not be fully resolved. The alteration is not behaving as distinct as expected. It indicates a sustainable change in the subsurface evoked by the injections. Whether this arises from density changes, variations in grain-to-grain contacts, or severe alterations in the hydrogeological setting of the subsurface remains open. Those challenges give much room to focus on complementing processing approaches such as frequency and dispersion analysis and provide real data for full waveform analysis. That would enhance the information width. Especially the acquisition of shear waves (SH, SV) will be essential to derive relevant geotechnical parameters such as anisotropy or consolidation ratio and to support and confirm other theoretical concepts. All three experiments show that gaining essential knowledge about parameter relation and dependencies in the near-surface opens up a vast knowledge potential in the future, considering the small number of field scale experiments.

107

Bibliography

[al Hagrey, 2011] al Hagrey, S. A. (2011). 2d optimized electrode arrays for borehole resistivity tomography and CO2 sequestration modelling. *Pure and Applied Geophysics*, 169(7):1283–1292.

[Allen et al., 1980] Allen, N. F., Richart Jr, F. E., and Woods, R. D. (1980). Fluid wave propagation in saturated and nearly saturated sands. *Journal of Geotechnical and Geoenvironmental Engineering*, 106.

[Asnaashari et al., 2014] Asnaashari, A., Brossier, R., Garambois, S., Audebert, F., Thore, P., and Virieux, J. (2014). Time-lapse seismic imaging using regularized full-waveform inversion with a prior model: which strategy? *Geophysical Prospecting*, 63(1):78–98.

[Bachrach and Nur, 1998] Bachrach, R. and Nur, A. (1998). High-resolution shallow-seismic experiments in sand, part i: Water table, fluid flow, and saturation. *GEOPHYSICS*, 63(4):1225–1233.

[Ballard et al., 1991] Ballard, R. F., Rechtien, R. D., and Hambacker, K. L. (1991). Performance evaluation of a high-freqency borehole seismic source. In *SEG Technical Program Expanded Abstracts 1991*. Society of Exploration Geophysicists.

[Becht et al., 2004] Becht, A., Tronicke, J., Appel, E., and Dietrich, P. (2004). Inversion strategy in crosshole radar tomography using information of data subsets. *GEOPHYSICS*, 69(1):222–230.

[Benson and Wu, 1999] Benson, A. K. and Wu, J. (1999). A modeling solution for predicting (a) dry rock bulk modulus, rigidity modulus and (b) seismic velocities and reflection coefficients in porous, fluid-filled rocks with applications to laboratory rock samples and well logs. *Journal of Applied Geophysics*, 41(1):49–73.

[Binley et al., 2015] Binley, A., Hubbard, S. S., Huisman, J. A., Revil, A., Robinson, D. A., Singha, K., and Slater, L. D. (2015). The emergence of hydrogeophysics for improved understanding of subsurface processes over multiple scales. *Water Resources Research*, 51(6):3837–3866.

BIBLIOGRAPHY

[Biot, 1956] Biot, M. A. (1956). Theory of propagation of elastic waves in a fluid-saturated porous solid. i. low-frequency range. *The Journal of the Acoustical Society of America*, 28(2):168–178.

[Biot and Willis, 1957] Biot, M. A. and Willis, D. G. (1957). The elastic coefficients of the theory of consolidation. *Journal of Applied Mechanics*, 24(4):594–601.

[Birnstengel et al., 2024] Birnstengel, S., Dietrich, J. P., Peisker, K., Pohle, M., Hornbruch, G., Bauer, S., Hu, L., Günther, T., Dahmke, A., and Werban, U. (2024). Experimental seismic crosshole setup to investigate the application of rock physical models at the field scale. *GEOPHYSICS*.

[Blazevic et al., 2020] Blazevic, L., Bodet, L., Pasquet, S., Linde, N., Jougnot, D., and Longuevergne, L. (2020). Time-lapse seismic and electrical monitoring of the vadose zone during a controlled infiltration experiment at the ploemeur hydrological observatory, france. *Water*, 12(5):1230.

[Boitnott and Bonner, 1994] Boitnott, G. N. and Bonner, B. P. (1994). Characterization of rock for constraining reservoir scale tomography at the geysers geothermal field. In *United States*.

[Bourbie et al., 1987] Bourbie, T., Coussy, O., and Zinszner, B. (1987). *Acoustics of porous media*. Gulf Publishing Co.

[Butler, 1997] Butler, J. J. J. (1997). *The Design, Performance, and Analysis of Slug Tests*. CRC Press.

[Cahill et al., 2017] Cahill, A. G., Steelman, C. M., Forde, O., Kuloyo, O., Ruff, S. E., Mayer, B., Mayer, K. U., Strous, M., Ryan, M. C., Cherry, J. A., and Parker, B. L. (2017). Mobility and persistence of methane in groundwater in a controlled-release field experiment. *Nature Geoscience*, 10(4):289–294.

[Chadwick et al., 2009] Chadwick, R., Noy, D., Arts, R., and Eiken, O. (2009). Latest time-lapse seismic data from sleipner yield new insights into CO2 plume development. *Energy Procedia*, 1(1):2103–2110.

[Chelidze et al., 2018] Chelidze, T., Vallianatos, F., and Telesca, L., editors (2018). *Complexity of seismic time series: Measurement and application.* Elsevier.

[Dahmke et al., 2021] Dahmke, A., Hornbruch, G., Lüders, K., Dietrich, P., Werban, U., Birnstengel, S., Richnow, H.-H., Vogt, C., Keller, N.-S., Geistlinger, H., and Zulfiqar, B. (2021). Verbundprojekt ug: Testum-aquifer – testfeld zur untersuchung und zum monitoring durch die nutzung des untergrundes induzierter reaktiver mehrphasentransportprozesse in oberflächennahen aquiferen. Technical report, Christian-Albrechts-Universität zu Kiel, Institut für Geowissenschaften, Kiel; Helmholtzzentrum für Umweltforschung GmbH Leipzig - UFZ.

[Dangeard et al., 2021] Dangeard, M., Rivière, A., Bodet, L., Schneider, S., Guérin, R., Jougnot, D., and Maineult, A. (2021). River corridor model constrained by time-lapse seismic acquisition. *Water Resources Research*, 57(10).

[Deutsches Zentrum für Luft und-Raumfahrt, 2022] Deutsches Zentrum für Luft und-Raumfahrt (2022). Pipeline leaks in the focus of dlr research. In *Measuring methane from the air and monitoring infrastructure from space.*

[Di Martino et al., 2021] Di Martino, M. D. P., De Siena, L., Healy, D., and Vialle, S. (2021). Petro-mineralogical controls on coda attenuation in volcanic rock samples. *Geophysical Journal International*, 226(3):1858–1872.

[Diallo, 2000] Diallo, M. S. (2000). *Acoustic waves attenuation and velocity dispersion in fluid-filled porous media: theoretical and experimental investigations.* PhD thesis, University of Tübingen.

[Dietrich et al., 2008] Dietrich, P., Butler Jr, J. J., and Faiß, K. (2008). A rapid method for hydraulic profiling in unconsolidated formations. *Groundwater*, 46(2).

[Dietrich and Leven, 2006] Dietrich, P. and Leven, C. (2006). *Direct Push-Technologies*, chapter 11, pages 321–340. Springer Berlin Heidelberg.

[Dietrich and Tronicke, 2009] Dietrich, P. and Tronicke, J. (2009). Integrated analysis and interpretation of cross-hole p- and s-wave tomograms: a case study. *Near Surface Geophysics*, 7:101.

[Dlugosch, 2014] Dlugosch, R. (2014). *Aquifer characterisation using nuclear magnetic resonance.* PhD thesis, Technische Universität Berlin.

[Dvorkin and Nur, 1993] Dvorkin, J. and Nur, A. (1993). Dynamic poroelasticity: A unified model with the squirt and the biot mechanisms. *GEOPHYSICS*, 58(4):524–533.

[Fehler and Pearson, 1984] Fehler, M. and Pearson, C. (1984). Cross-hole seismic surveys: Applications for studying subsurface fracture systems at a hot dry rock geothermal site. *GEOPHYSICS*, 49(1):37–45.

[Gassmann, 1951] Gassmann, F. (1951). über die elastizität poröser medien. *Vierteljahrsschrift der Naturforschenden Gesellschaft in Zürich*, 96:1–23.

[Geistlinger and Zulfiqar, 2020] Geistlinger, H. and Zulfiqar, B. (2020). The impact of wettability and surface roughness on fluid displacement and capillary trapping in 2-d and 3-d porous media: 1. wettability-controlled phase transition of trapping efficiency in glass beads packs. *Water Resources Research*, 56(10).

[Gist, 1994] Gist, G. A. (1994). Interpreting laboratory velocity measurements in partially gas-saturated rocks. *GEOPHYSICS*, 59(7):1100–1109.

[Götz, 2014] Götz, J. (2014). *Borehole seismic monitoring of CO2 storage within a saline aquifer at Ketzin, Germany.* PhD thesis, Technische Universität Berlin.

[Gregory, 1976] Gregory, A. R. (1976). Fluid saturation effects on dynamic elastic properties of sedimentary rocks. *GEOPHYSICS*, 41(5):895–921.

[Grosso and Mader, 1972] Grosso, V. D. and Mader, C. W. (1972). Speed of sound in pure water. *Journal of the Acoustical Society of America*, 52(5B):1442–1446.

[Hardee et al., 1987] Hardee, H. C., Elbring, G. J., and Paulsson, B. N. P. (1987). Downhole seismic source. *GEOPHYSICS*, 52(6):729–739.

[Harris et al., 1995] Harris, J. M., Nolen-Hoeksema, R. C., Langan, R. T., Schaack, M. V., Lazaratos, S. K., and James W. Rector, I. (1995). High-resolution crosswell imaging of a west texas carbonate reservoir: Part 1—project summary and interpretation. *GEOPHYSICS*, 60(3).

[Hausmann, 2013] Hausmann, J. (2013). Two-dimensional geomorphological characterization of a filled abandoned meander using geophysical methods and soil sampling. *Geopmorphology*, 2.

[Heldt et al., 2021a] Heldt, S., Wang, B., Hu, L., Hornbruch, G., Lüders, K., Werban, U., and Bauer, S. (2021a). Data of a high temperature heat injection test. *Data in Brief*, 36:107035.

[Heldt et al., 2021b] Heldt, S., Wang, B., Hu, L., Hornbruch, G., Lüders, K., Werban, U., and Bauer, S. (2021b). Numerical investigation of a high temperature heat injection test. *Journal of Hydrology*, 597:126229.

[Hellwig, 2017] Hellwig, O. (2017). *A Seismic exploration ahead of boreholes using borehole-guided waves: A feasibility study.* PhD thesis, Technische Universität Freiberg, Fakultät für Geowissenschaften, Geotechnik und Bergbau.

[Hermans et al., 2013] Hermans, T., Wildemeersch, S., Jamin, P., Orban, P., Brouyère, S., Dassargues, A., and Nguyen, F. (2013). A heat injection and pumping experiment in a gravel aquifer monitored with crosshole electrical resistivity tomography. In *Proceedings*. EAGE Publications BV.

[Hideki et al., 2008] Hideki, S., Dai, N., Hiroyuki, A., Daiji, T., and Ziqiu, X. (2008). Time-lapse cross-well seismic tomography for monitoring co 2 geological sequestration at the nagaoka pilot project site. *Journal of MMIJ*, 124(1):78–86.

[Hu et al., 2017] Hu, L., Doetsch, J., Brauchler, R., and Bayer, P. (2017). Characterizing co2 plumes in deep saline formations: Comparison and joint evaluation of time-lapse pressure and seismic tomography. *GEOPHYSICS*, 82(4):ID1–ID18.

[Hu et al., 2023] Hu, L., Schnackenberg, M., Hornbruch, G., Lüders, K., Pfeif-
    fer, W. T., Werban, U., and Bauer, S. (2023). Cross-well multilevel pumping
    tests – a novel approach for characterizing the changes of hydraulic properties
    during gas storage in shallow aquifers. *Journal of Hydrology*, 620:129520.

[Jaya and Milsch, 2013] Jaya, M. and Milsch, H. (2013). Dependency of seismic
    compressional wave velocity and attenuation on temperature and liquid-steam
    phase transition. In *75th EAGE Conference and Exhibition incorporating SPE
    EUROPEC 2013*. European Association of Geoscientists and Engineers.

[Jaya et al., 2010] Jaya, M. S., Shapiro, S. A., Kristinsdóttir, L. H., Bruhn,
    D., Milsch, H., and Spangenberg, E. (2010). Temperature dependence of
    seismic properties in geothermal rocks at reservoir conditions. *Geothermics*,
    39(1):115–123.

[Jefferson et al., 1998] Jefferson, R. D., Steeples, D. W., Black, R. A., and Carr,
    T. (1998). Effects of soil-moisture content on shallow-seismic data. *GEO-
    PHYSICS*, 63(4):1357–1362.

[Jones et al., 1980] Jones, T., Murphy, W., and Nur, A. (1980). Effects of tem-
    perature and saturation on the velocity and attenuation of seismic waves in
    rocks: Applications to geothermal reservoir evaluation. In *Sixth Workshop
    Geothermal Reservoir Engineering, Stanford University, Stanford, California,
    December 16-18, 1980*.

[Jordi et al., 2016] Jordi, C., Schmelzbach, C., and Greenhalgh, S. (2016).
    Frequency-dependent traveltime tomography using fat rays: application to
    near-surface seismic imaging. *Journal of Applied Geophysics*, 131:202–213.

[Jorgensen, 1989] Jorgensen, D. G. (1989). Using geophysical logs to estimate
    porosity, water resistivity, and intrinsic permeability. *US Geological Survey*.

[Keller et al., 2021] Keller, N.-S., Hornbruch, G., Lüders, K., Werban, U., Vogt,
    C., Kallies, R., Dahmke, A., and Richnow, H. H. (2021). Monitoring of the
    effects of a temporally limited heat stress on microbial communities in a
    shallow aquifer. *Science of The Total Environment*, 781:146377.

[Kern et al., 2001] Kern, H., Popp, T., Gorbatsevich, F., Zharikov, A.,
    Lobanov, K., and Smirnov, Y. (2001). Pressure and temperature dependence
    of vp and vs in rocks from the superdeep well and from surface analogues at
    kola and the nature of velocity anisotropy. *Tectonophysics*, 338(2):113–134.

[Köber et al., 2009] Köber, R., Hornbruch, G., Leven, C., Tischer, L., Groß-
    mann, J., Dietrich, P., Weiß, H., and Dahmke, A. (2009). Evaluation of
    combined direct-push methods used for aquifer model generation. *Ground
    Water*, 47(4):536–546.

[Köhn et al., 2017] Köhn, D., De Nil, D., Thorwart, M., Rabbel, W., Hübscher,
    C., and Pfeiffer, W. (2017). überwachung unterirdischer energiespeicher und

kartierung potentieller leckagepfade mit seismischer full waveform inversion. In *ANGUS Symposium 2017: Energiespeicher im geologischen Untergrund. ANGUS, Kiel.*

[Köhn et al., 2013] Köhn, D., Hagrey, S. A., and Rabbel, W. (2013). Monitoring of underground gas storage sites by elastic 2d time-lapse waveform inversion.

[Lamert et al., 2012] Lamert, H., Geistlinger, H., Werban, U., Schütze, C., Peter, A., Hornbruch, G., Schulz, A., Pohlert, M., Kalia, S., Beyer, M., Großmann, J., Dahmke, A., and Dietrich, P. (2012). Feasibility of geo-electrical monitoring and multiphase modeling for process understanding of gaseous CO_2 injection into a shallow aquifer. *Environmental Earth Sciences*, 67(2):447–462.

[Li and Schanz, 2011] Li, P. and Schanz, M. (2011). Wave propagation in a 1-d partially saturated poroelastic column. *Geophysical Journal International*, 184(3):1341–1353.

[Li et al., 2019] Li, S., Wang, D., and Zhang, M. (2019). Influence of upscaling on identification of reservoir fluid properties using seismic-scale elastic constants. *Scientific reports*, 9(1).

[Löffler et al., 2022] Löffler, M., Schrader, M., Lüders, K., Werban, U., Hornbruch, G., Dahmke, A., Vogt, C., , and Richnow, H. H. (2022). Stable hydrogen isotope fractionation of hydrogen in a field injection experiment: Simulation of a gaseous h2 leakage. *ACS Earth Space Chem.*, 6(3):631–641.

[Lüders et al., 2021] Lüders, K., Hornbruch, G., Zarrabi, N., Heldt, S., Dahmke, A., and Köber, R. (2021). Predictability of initial hydrogeochemical effects induced by short-term infiltration of ∼75 °c hot water into a shallow glaciogenic aquifer. *Water Research X*, 13:100121.

[Lumley, 2010] Lumley, D. (2010). 4d seismic monitoring of CO_2 sequestration. *The Leading Edge*, 29(2):150–155.

[Lumley et al., 2008] Lumley, D., Adams, D., Wright, R., Markus, D., and Cole, S. (2008). *Seismic monitoring of CO2 geo-sequestration: realistic capabilities and limitations*, chapter 27, pages 2841–2845. Society of Exploration Geophysicists.

[Lumley, 2001] Lumley, D. E. (2001). Time-lapse seismic reservoir monitoring. *GEOPHYSICS*, 66(1):50–53.

[Marelli et al., 2012] Marelli, S., Maurer, H., and Manukyan, E. (2012). Validity of the acoustic approximation in full-waveform seismic crosshole tomography. *GEOPHYSICS*, 77(3):R129–R139.

[Mavko et al., 1995] Mavko, G., Chan, C. Y., and Mukerji, T. (1995). Fluid substitution: Estimating changes in vp without knowing vs. *GEOPHYSICS*, 60:1750–1755.

[Mavko et al., 2020] Mavko, G., Mukerji, T., and Dvorkin, J. (2020). *The Rock Physics Handbook*. Cambridge University Press.

[Milsch et al., 2008] Milsch, H. H., Spangenberg, E., Kulenkampff, J., and Meyhöfer, S. (2008). A new apparatus for long-term petrophysical investigations on geothermal reservoir rocks at simulated in-situ conditions. *Transport in Porous Media*, 74(1):73–85.

[Müller et al., 2010] Müller, T. M., Gurevich, B., and Lebedev, M. (2010). Seismic wave attenuation and dispersion resulting from wave-induced flow in porous rocks - a review. *GEOPHYSICS*, 75(5):75A147–75A164.

[Nanda, 2016] Nanda, N. C. (2016). *Seismic Data Interpretation and Evaluation for Hydrocarbon Exploration and Production*. Springer International.

[Ng et al., 2019] Ng, Y. C. H., Danovan, W., and Ku, T. (2019). The potential of seismic cross-hole tomography for geotechnical site investigation. *E3S Web of Conferences*, 92:18006.

[Onishi et al., 2009] Onishi, K., Ueyama, T., Matsuoka, T., Nobuoka, D., Saito, H., Azuma, H., and Xue, Z. (2009). Application of crosswell seismic tomography using difference analysis with data normalization to monitor CO2 flooding in an aquifer. *International Journal of Greenhouse Gas Control*, 3(3):311–321.

[Paasche et al., 2009] Paasche, H., Werban, U., and Dietrich, P. (2009). Near-surface seismic traveltime tomography using a direct-push source and surface-planted geophones. *GEOPHYSICS*, 74(4):G17–G25.

[Partyka et al., 2000] Partyka, G. A., Thomas, J. B., Turco, K. P., and Hartmann, D. J. (2000). Upscaling petrophysical properties to the seismic scale. In *2000 SEG Annual Meeting*.

[Peter et al., 2012] Peter, A., Lamert, H., Beyer, M., Hornbruch, G., Heinrich, B., Schulz, A., Geistlinger, H., Schreiber, B., Dietrich, P., Werban, U., Vogt, C., Richnow, H.-H., Großmann, J., and ke, A. (2012). Investigation of the geochemical impact of co2 on shallow groundwater: design and implementation of a co2 injection test in northeast germany. *Environmental Earth Sciences*, 67(2).

[Pevzner et al., 2020] Pevzner, R., Urosevic, M., Tertyshnikov, K., AlNasser, H., Caspari, E., Correa, J., Daley, T., Dance, T., Freifeld, B., Glubokovskikh, S., Greenwood, A., Kepic, A., Popik, D., Popik, S., Raab, M., Robertson, M., Shulakova, V., Singh, R., Watson, M., Yavuz, S., Ziramov, S., and Gurevich, B. (2020). *Active surface and borehole seismic monitoring of a small supercritical CO2 injection into the subsurface: experience from the CO2CRC Otway Project*, pages 497–522. Elsevier.

[Pohle et al., 2022] Pohle, M., Birnstengel, S., Kotas, H., Peisker, K., Schoßland, A., Schultz, J., and Werban, U. (2022). Seismic crosshole data at the

testum site in wittstock/dosse (germany). PANGAEA - Data Publisher for Earth & Environmental Science.

[Randall et al., 1991] Randall, C. J., Scheibner, D. J., and Wu, P. T. (1991). Multipole borehole acoustic waveforms: Synthetic logs with beds and borehole washouts. *GEOPHYSICS*, 56(11):1757–1769.

[Rechtien et al., 1993] Rechtien, R. D., Hambacker, K. L., and Ballard, R. F. (1993). A high-frequency sparker source for the borehole environment. *GEOPHYSICS*, 58(5):660–669.

[Reuss, 1929] Reuss, A. (1929). Berechnung der fließgrenze von mischkristallen auf grund der plastizitätsbedingung für einkristalle . *ZAMM - Zeitschrift für Angewandte Mathematik und Mechanik*, 9(1):49–58.

[Robinson et al., 2008] Robinson, D. A., Binley, A., Crook, N., Day-Lewis, F. D., Ferré, T. P. A., Grauch, V. J. S., Knight, R., Knoll, M., Lakshmi, V., Miller, R., Nyquist, J., Pellerin, L., Singha, K., and Slater, L. (2008). Advancing process-based watershed hydrological research using near-surface geophysics: a vision for, and review of, electrical and magnetic geophysical methods. *Hydrological Processes*, 22(18):3604–3635.

[Romero-Ruiz et al., 2021] Romero-Ruiz, A., Linde, N., Baron, L., Solazzi, S. G., Keller, T., and Or, D. (2021). Seismic signatures reveal persistence of soil compaction. *Vadose Zone Journal*.

[Schön, 2004] Schön, J. H. (2004). *Physical Properties of Rocks: Fundamentals and Principles of Petrophysics*, volume 18. Elsevier.

[Schön, 2015] Schön, J. H. (2015). *Physical Properties of Rocks: Fundamentals and Principles of Petrophysics*, volume 218. Elsevier.

[Schulze-Makuch et al., 1999] Schulze-Makuch, D., Carlson, D. A., Cherkauer, D. S., and Malik, P. (1999). Scale dependency of hydraulic conductivity in heterogeneous media. *Ground Water*, 37(6):904–919.

[Sheriff, 1975] Sheriff, R. E. (1975). Factors affecting seismic amplitudes. *Geophysical Prospecting*, 23(1):125–138.

[Solazzi et al., 2021] Solazzi, S. G., Bodet, L., Holliger, K., and Jougnot, D. (2021). Rayleigh waves, dispersion, partial saturation, capillary forces, modeling, porous media. *Journal of Geophysical Research: Solid Earth*, 126(12).

[Tiwary et al., 2009] Tiwary, D. K., Bayuk, I. O., Vikhorev, A. A., and Chesnokov, E. M. (2009). Comparison of seismic upscaling methods: From sonic to seismic. *GEOPHYSICS*, 74(2).

[Trautz et al., 2020] Trautz, R., Daley, T., Miller, D., Robertson, M., Koperna, G., and Riestenberg, D. (2020). Geophysical monitoring using active seismic techniques at the citronelle alabama CO2 storage demonstration site. *International Journal of Greenhouse Gas Control*, 99:103084.

[Truebner, 2017] Truebner (2017). *Datenblatt SMT100*. Truebner.

[Vasheghani et al., 2009] Vasheghani, F., Lines, L. R., and Embleton, J. (2009). The effects of fluid viscosity on seismic response: A model study. In *Frontiers + Innovation – 2009 CSPG CSEG CWLS Convention*.

[Voigt, 1910] Voigt, W. (1910). *Lehrbuch der Kristallphysik (mit Ausschluss der Kristalloptik)*. BG Teubner.

[von Ketelhodt et al., 2019] von Ketelhodt, J. K., Manzi, M. S. D., Durrheim, R. J., and Fechner, T. (2019). Seismic vertical transversely isotropic parameter inversion from p- and s-wave cross-borehole measurements in an aquifer environment. *GEOPHYSICS*, 84(3):D101–D116.

[Wang and Nur, 1990] Wang, Z. and Nur, A. (1990). Wave velocities in hydrocarbon-saturated rocks: Experimental results. *GEOPHYSICS*, 55(6):723–733.

[Watanabe et al., 1999] Watanabe, T., Matsuoka, T., and Ashida, Y. (1999). Seismic traveltime tomography using fresnel volume approach.

[Wen, 2018] Wen, R. (2018). Multi-scale permeability modeling and upscaling workflow integrating core, well log, seismicattributes and geologic models. In *Geomodeling Technology Corp.*

[Whiteley et al., 2020] Whiteley, J., Chambers, J., Uhlemann, S., Boyd, J., Cimpoiasu, M., Holmes, J., Inauen, C., Watlet, A., Hawley-Sibbett, L., Sujitapan, C., Swift, R., and Kendall, J. (2020). Landslide monitoring using seismic refraction tomography – the importance of incorporating topographic variations. *Engineering Geology*, 268:105525.

[Wightman et al., 2004] Wightman, W. E., Jalinoos, F., Sirles, P., and Hanna, K. (2004). Application of geophysical methods to highway related problems. Technical Report 200512, United States. Federal Highway Administration. Central Federal Lands Highway Division.

[Winbow, 1991] Winbow, G. A. (1991). Seismic sources in open and cased boreholes. *GEOPHYSICS*, 56(7):1040–1050.

[Wyllie et al., 1956] Wyllie, M. R. J., Gregory, A. R., and Gardner, L. W. (1956). ELASTIC WAVE VELOCITIES IN HETEROGENEOUS AND POROUS MEDIA. *GEOPHYSICS*, 21(1):41–70.

[Zhang et al., 2012] Zhang, F., Juhlin, C., Cosma, C., Tryggvason, A., and Pratt, R. G. (2012). Cross-well seismic waveform tomography for monitoring CO2 injection: a case study from the ketzin site, germany. *Geophysical Journal International*, 189(1):629–646.

[Zhang et al., 2021] Zhang, J., Shen, Y., Yang, G., Zhang, H., Wang, Y., Hou, X., Sun, Q., and Li, G. (2021). Inconsistency of changes in uniaxial compressive strength and p-wave velocity of sandstone after temperature treatments. *Journal of Rock Mechanics and Geotechnical Engineering*, 13(1):143–153.

[Zhijing Wan, 1990] Zhijing Wan, Michael L Batzle, A. M. N. (1990). Effect of different pore fluids on seismic velocities in rocks. *Canadian Journal of Exploration Geophysics*, 26(1):104–112.

[Zulfiqar et al., 2020] Zulfiqar, B., Vogel, H., Ding, Y., Golmohammadi, S., Küchler, M., Reuter, D., and Geistlinger, H. (2020). The impact of wettability and surface roughness on fluid displacement and capillary trapping in 2-d and 3-d porous media: 2. combined effect of wettability, surface roughness, and pore space structure on trapping efficiency in sand packs and micromodels. *Water Resources Research*, 56(10).